Resonant MEMS structures for displacement sensing

(a sensor in a nutshell)

Dissertation

zur

Erlangung der Doktorwürde

der

Fakultät für Elektrotechnik und Informationstechnik

vorgelegt von

Alexander Dabsch
aus Wien

Wien 2021
Technische Universität Wien

Preface

While writing this thesis, it is time to take a look back on the past four years and rethink numerous ideas that came up during the experiments and, at times, rather in between the scientific work. Failures like inoperative prototypes were taking place next to more pleasant adventures, such as no fewer than seven patents registered since 2014[1]. Some of these have been developed for one of the companies that I frequently deal with; others for the Technical University of Vienna, which means something special to me. While industrial patents are a fixed part of a company strategy to protect knowledge created in-house and demonstrate innovative strength to the sector, applied technological development is often viewed with some reservation at scientific institutions, even in technical areas. “Too far away from basic research,” or, “with too low an academic level for university research” are standard phrases put against application-oriented research. Meanwhile, many projects without direct use for industrial application often do not meet customer needs.

I must confess that there are some who have made ritzier calculations of complex problems or have set up their experiments closer to the latest methods of authors in top journals. However, my basic idea behind every single project is to improve an existing solution, solve a given problem, or give food for thought by creating products – not only concepts – that are standalone solutions which find their place even amongst the numerous existing devices in the sector of sensor technology. These solutions mostly evolve from similar concepts developed in the past, by me or my predecessors, but with a subtle difference, thereby creating something completely new, as we will see in the present thesis.

With this attitude, me and my team do not always run into open doors. Naturally, everyone who does not run a system according to existing rules is met with resistance; currently however, a new designation, especially in the startup community, is evolving for such people. We call these people “Game Changers” and appreciate their novel concepts that have been created outside of the boundaries posed by large companies, or even what would seem reasonable under huge economic pressure at large. These “Game Changers” devise products and services that are out of the box, driven by their own creativity and personal enthusiasm for a vision of something new and sometimes, at first sight, unusable. Indeed, some ideas

[1] Two patents registered within the scientific work (AT517945 (A4) - SENSOR ZUR BESTIMMUNG EINES DREHWINKELS – 15.06.2017 – issued and PCT/AT2017/060082 – Force Sensor – 04.10.2018 – issued and internationalized (PCT)) and five patents within the industrial development (two issued – three registered)

reveal their best usage only long after having been invented, as it has been the case with the PikoSens prototype which was originally designed as a force-sensor and now works as a high precision displacement-sensor in many prototype applications. Being a Game Changer means swimming against the tide and going the path of greatest resistance. But it is the best part of the game to work on something new by changing everything old; which, however, does not mean that everything old has to be changed (like the title page of the University of Göttingen from 1908).

This thesis, which mainly talks about the PikoSens project, is the outcome of the past four years of autonomous research enabled mostly by Professor Franz Keplinger. He allowed free reign to me and my ideas and undertakings, which were not always easy to handle whilst my team and I were spending a lot of time fixing problems outside of my research work. In the end, we are able to show a well-defined sensor prototype beyond entrepreneurial applications, which already allows us to cooperate with two leading companies from the measurement technology sector in third-party funded research projects, and we look ahead to continuing the scientific work in the next years to create stand-alone sensor technology for highly complex applications. The university background opens many doors for us to deal with the best companies in our sector, and we are hopeful for this cooperation to continue.

Kurzfassung

Diese Arbeit beschäftigt sich mit den Möglichkeiten, einfache MEMS Sensor-Strukturen möglichst umfangreich zu nutzen und deren Einsatzmöglichkeiten zu erweitern. Der Ausgangspunkt der Entwicklung sind die Arbeiten von Univ.-Prof. Dr. Franz Keplinger und Dr. Michael Stifter, welche sich zunächst mit der Herstellung und Vermessung von einfachen Silizium Kragbalken für den Einsatz als eindimensionales Magnetometer beschäftigen und im Weiteren, durch die Weiterentwicklung zu U-förmigen Balken, auch zwei Feldkomponenten des Magnetfeldes vermessen können. Eingesetzt werden für diese Sensor-Strukturen Standard MEMS Prozesse sowie Referenzmessungen unter dem Einsatz eines Laser-Doppler-Vibrometers, welches als Referenz für alle weitern Strukturen herangezogen wird, wodurch eine hohe Vergleichbarkeit der Strukturen gegeben ist. Diese vom Prinzip nicht neue Technologie wurde jedoch durch deren Arbeit so fein abgestimmt, dass die erzielbare Sensitivität im Bereich jener der Hall-Sensoren liegt und mit Messbedingungen im Vakuum noch verbessert werden kann.

Alle erwähnten Sensoren sind Lorentz Kraft angeregt und haben zu diesem Zweck Leiterbahnen, meist aus Gold, auf ihrer Oberfläche mittels welcher bei den Sensoren durch geeignete Positionierung gezielt zwischen mehreren Feldkomponenten unterschieden werden kann. Dieses Prinzip wird übernommen und findet auch bei der weiteren Entwicklung der Sensorstrukturen in dieser Arbeit Anwendung. Die Entwicklung geht dabei mit dem Vorbild der U-Struktur, mit welcher ein bis zwei Magnetfeldkomponenten vermessen werden können, hin zu einer Magnetfeldgradientenstruktur, welche eine örtliche Auflösung des Feldgradienten abbilden soll. Dies wird durch zwei gegenübergestellte und mechanisch gekoppelte Strukturen realisiert. Von dieser Sensor-Struktur wurden im Zuge der Entwicklung zwei unterschiedliche Strukturen realisiert welche durch geschickte Geometrieauswahl unterschiedliche Temperaturabhängigkeiten der Resonanzfrequenz aufweisen. Bei ansonsten gleichbleibenden Werkstoff- und Geometrieparametern konnte auf diese Weise die Abhängigkeit von der Umgebungstemperatur um 75% verringert werden[2].

Im letzten Abschnitt wird auf die Entwicklung des PikoSens „Displacement Sensors“ eingegangen, welcher als Weiterentwicklung der Magnetfeldgradientenstruktur gesehen werden kann. Eine kreuzförmige Basis-Struktur dient als vorgespannte Saite und wird durch die Verschiebung des Sensorrahmens, welcher in vier Bereiche unterteilt ist, „verspannt“.

[2] A. Dabsch et al.; „Temperature dependency of silicon structure for magnetic field gradient sensing“; Journal of Micromechanics and Microengineering; Dec. 2017

Diese Verspannung bewirkt eine unterschiedliche Änderung aller Resonanzmoden, je nach Belastungsrichtung und –stärke. Durch dieses Modell können mehrere Kraftkomponenten gleichzeitig bestimmt werden, was sowohl durch Simulation als auch durch Messungen gezeigt wird. Die Vorteile der Temperatureffekt-Kompensation aus den Gradienten-Strukturen wurden für diese Entwicklung übernommen, wobei der Effekt auch hier deutlich nachweisbar ist.

Contents

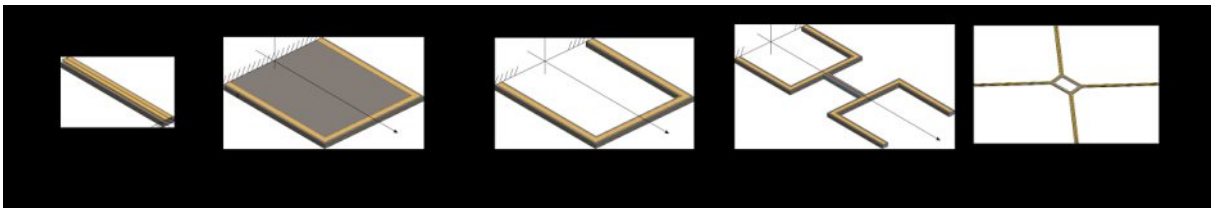

I. Motivation and Concepts

1.1 Introduction

Let's start.

Sensors are the most powerful tools in an automation process and in the aspiring field of robotics. As Goethe said, "The senses are not deceiving, but the verdict is deceptive"[3]. Modern sensors are the senses of robots and machines, which interact with humans in many applications: From uses in the automotive sector to modern electronic devices, up to fully automated fabrication and delivery systems.

In recent years, the level auf automation in industry and production has increased dramatically. This has been accompanied by a large and growing number of sensor manufacturers from a wide variety of specialties and various economic sectors. The global sensor market for automation processes is expected to grow at an annual rate of 11.3% during the five-year period starting 2017 and to reach a market volume of 241 billion dollars[4]. According to the same study, medical technologies will grow above average at 12.6% per year and will outpace the electronics industry with respect to the number of sensor elements used. In the same period, the number of requested industry robots will double, up to over 500,000 units per year[5].

Increased interest in sensors in almost all industries favours the development of novel, highly specialised sensors and thus fuels the interest of researchers and research institutes. Combined

[3] Johann Wolfang von Goethe;„Maximen und Reflexionen, Nachlaß, Über Natur und Naturwissenschaft"
[4] CAGR – Allied Market Research – German Ministry for Economy and Energy "Industrie 4.0 Zielmarktanalyse USA 2017"
[5] IFR – International Federation of Robotics; „How robots conquer industry worldwide"; https://ifr.org/downloads/press/Presentation_PC_27_Sept_2017.pdf; 27.9.2018 12:34 Uhr.

with new driveline technologies, sensor and measurement systems are strong tools for automation tasks and justify high development costs of smart automation systems.
Developing new sensor technologies does not always mean starting from scratch, but rather also finding new ways to use existing tools with a minimum effort of adaption. It can either mean creating sensors with a wide range of applications and finding new ways to implement them, or finding new possibilities to use the existing hardware of sensors to measure other physical quantities. For example, we've developed the PikoSens sensing element to measure small displacements based on a classic magnetic-field-sensor, using the main features of the microstructure.

Mechanical micro sensors, generally grouped under the collective term MEMS (micro-electro-mechanical-system), along with widely spread silicon etching and CMOS technology, open a wide area of possibilities and provide a maximum of freedom for layout options. These standard tools enable the use of mechanical sensors for many applications, e.g. electro-magnetic field sensors and micro fluidic elements, as well as force- or displacement sensing.

The first chapter of this work explains the theoretical background of the sensor development and the models for the simulation processes. The attached chapters are the presented publications in chronological order, followed by the patent document (PCT) of the developed sensor which is the basis of this work.

1.2 Existing MEMS devices

The starting point of the development of the PikoSens displacement sensors is the resonant single cantilever magnetic field sensor, invented by Donzier et. al. in 1991[i]. The sensor device is a cantilever manufactured out of a monocrystalline silicon, using standard etching technology. The excitation is achieved through the Lorentz force, triggered by an alternating current with a frequency near the resonance frequency of the cantilever, and the external static *B*-field.

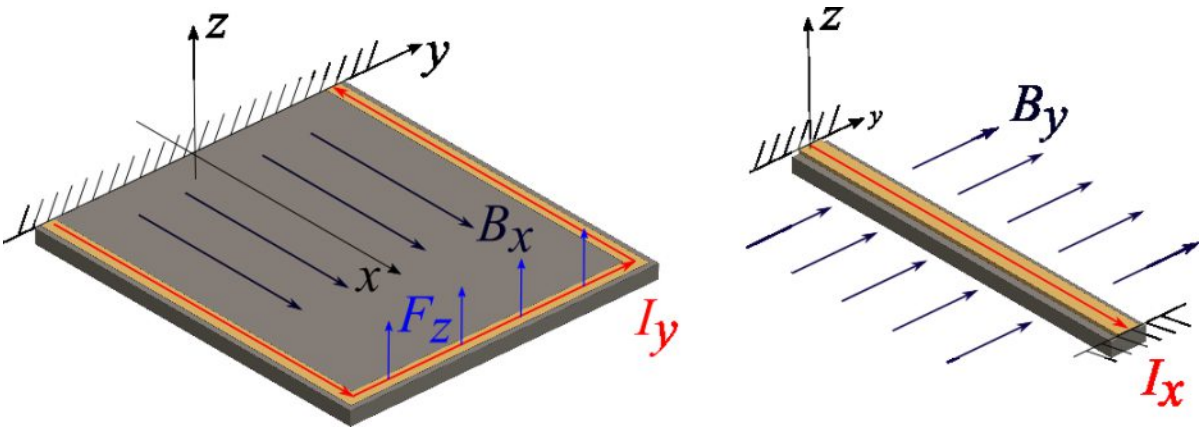

Figure 1: left: single clamped "cantilever" plate, right: double clamped cantilever. Depicted are the main parameters for an excitation of the cantilever by the Lorentz force under the influence of a magnetic field.

Using this simple structure design, the authors found that the sensitivity of the device is independent of the plate size and inversely proportional to the third power of the thickness. The resolution reached with this technology is 10 nT/Hz (resonance frequency 10 kHz and current 20 mA). Due to the high plate surface-to-mass ratio of the sensing structure, air damping is the largest limitation to a high Q factor and resolution. The design is applied in ATM (atomic force microscope) too, extended by an ultrafine measuring tip at the free end of the cantilever, as presented by Koblischka et. al.[ii], amongst others. An enhanced version of this sensor device was presented by Stifter in 2012 [iii] by using the same structure type extended by a counter electrode based capacitive readout and tested at the CERN accelerator dipole in 2015[iv], as described in Publication I.

Using the same single clamped cantilever type, Lang et. al.[v] presented a chemical sensor, based on a cantilever array of eight parallel cantilevers, fixed on the same side, to detect gases and vapors. The sensor uses additional coatings on the top surface, which interact with the gas to be detected. The linked particles on the surface increase the effective mass of the cantilever Δm. Based on this, there are two operation modes for the sensor device. One

detects the static bending of the cantilever, which is related to the surface stress. The second, dynamic mode detects the mass change by the following formula[vi],

$$\Delta m = \frac{k}{0.72\pi^2}\left(\frac{1}{f_f^2} - \frac{1}{f_i^2}\right) \quad (1)$$

where k is the spring constant of the cantilever, f_i the resonance frequency without additional load and f_f the resonance frequency during the measurement. This fundamental equation is derived from the simple, single cantilever structure. It shows that the indirect connection between resonance frequencies is associated with the function of the PikoSens device, as will be shown below.

The fundamental approach to using an existing development for alternative applications is the principal contribution of this work. The range of applications is further extended by Baselt et. al. in 2002, who present another possibility for the usage of a single clamped cantilever, introducing a micro cantilever-based hydrogen sensor which is able to detect hydrogen concentrations between 0.1 and 100% (linear output in a range of 10 to 90% hydrogen)[vii]. The best example for an application of such sensors can be found in fuel cells to detect hazardous leaks in hydrogen tanks, which operate in the same way as the chemical sensor by Lang (v). The Sensor uses a thin-film coated polymer layer, interacting with the surrounding hydrogen (this process is fully reversible) and increases the bending of the cantilever depending on the hydrogen concentration on the surface-layer. Using a capacitive readout, the counter electrode detects the bending of the cantilever tip.

In 2005, Keplinger[viii] introduced a magnetic field sensor based on the works of Deladi[ix] and Latorre[x], using a U-shaped cantilever, excited also by Lorentz Force. This structure type has a larger width/stiffness ratio which enables higher sensitivity compared to the single clamped cantilever “plates”. Using these fewer stiff structures, three components of the magnetic flux density are theoretically detectable, utilizing symmetric-/antisymmetric and in-plane excitation respectively. Simulations show that such in-plane modes have resonance frequencies in a range that is not accessible by currently available measuring instruments.

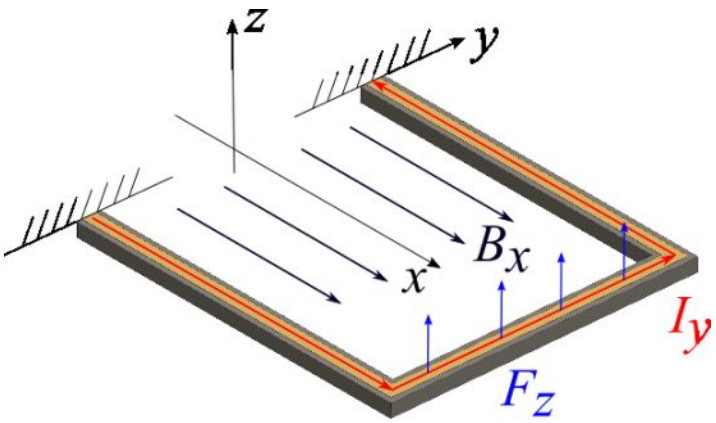

Figure 2: U-shaped cantilever with the main parameters (I, B and F) acting as a magnetometer. Only the beam in y-direction has a contribution to the excitation.

These devices have higher sensitivity with regard to the single clamped cantilever and reach higher Q factors which does not seem extraordinary considering the much higher stiffness/mass ratio (approximately height/cross-section-area of the cantilever). Splitting the readout of the vibration amplitude into a symmetric and an antisymmetric component, the device, when restricted to one component of the flux density, allows the determination of the flux density gradient. The most important limitation, also with this device, is the Q factor (~10^3 with this sensor) which can be increased by bringing the sensor device into a tight sealed vacuum encapsulation. Then, Q factors in a range of 10^5 are achievable.

1.2.1 Further development

The existing devices mentioned above deliver the tools to design a stand-alone magnetic field gradient sensor using a mirrored double U-shaped structure as described in Publication II [xi]. Both U-shaped-substructures are interconnected by an additional coupling bar to align minimal variations of the geometry of both U-structures caused by variations in the manufacturing process and, therefore, variations in the resonance frequencies of the two structures. The resonant operation mode needs an exact synchronisation of the two opposite structures as the high Q factor produces differences in the deflection without the coupling bar.

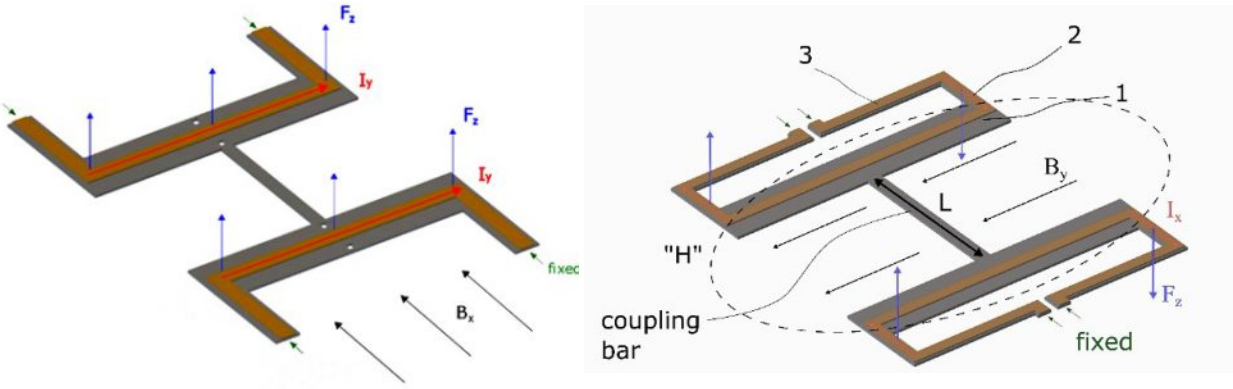

Figure 3: Magnetic field gradient structures. Left: double U-shaped structure. Right: Omega-shaped strucure, Temperature effect compensation sub-structure (3)

To analyse the temperature dependency of the double clamped structures (attachment points are marked with green arrows), two different structure types are introduced. Fig. 3 & 4, one double U-shaped structure (left picture) as already described and a double omega-shaped structure (right picture), which has a much lower temperature dependency of the resonance frequency than the double U-shaped one.[6]

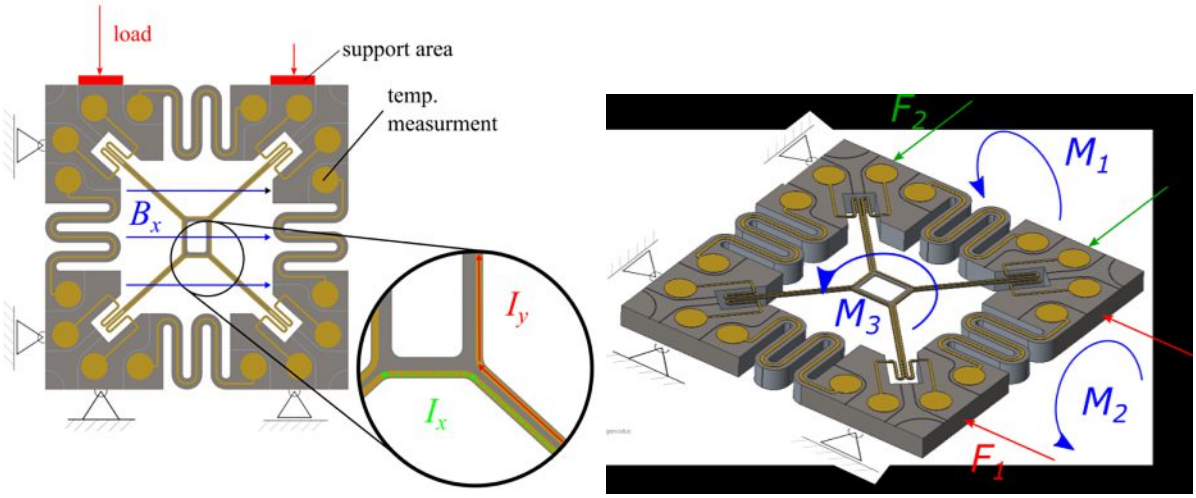

Figure 4: Cross shaped displacement sensing structure "PikoSens" with the theoretical possible parameters to be measured (F_1, F_2, M_1, M_2 and M_3).

Coming from the structures for the magnetic field gradient, we already have wide-range knowledge about the effects of external loads on the resonance frequency of the respective modes of the structure. Taking a step further, we introduce a cross shaped structure that is related to the double U-shaped structure, to measure the displacement in the *x*- and *y*-direction by tracing the resonance frequency of different vibration modes. Therefore, the cross-shaped structure is attached at its four ends to a sensor frame that has meander sub-structures between

[6] As shown in "A. Dabsch, "Temperature dependency of silicon structures for magnetic field gradient sensing" Journal of Micromechanics and Microengineering, July 2017" [23]

the attachment points to enable the deformation of the sensing element. With this structure type, we are theoretically able to measure five degrees of freedom (DOF). The possible parameters to measure are two linear displacements in the plane of the sensing structure (F_1 and F_2) and three moments (M_1, M_2 and M_3) around the three main axes. The displacement measurement structure, named "PikoSens", is the main contribution of the present work and is part of the further development to implement the wide field of application of this structure type.

II. Background and Theory

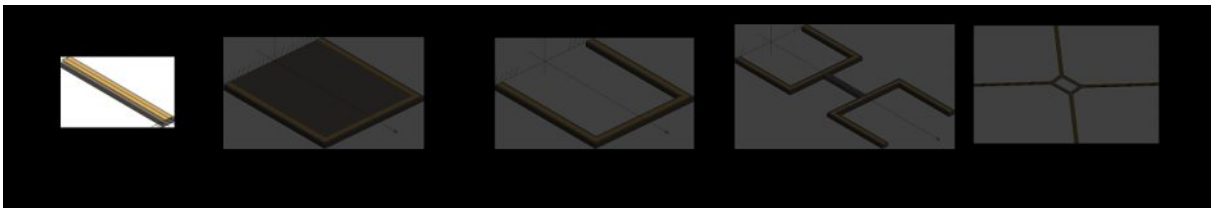

2.1 Euler-Bernoulli and Timoshenko beam

Like many calculations in this field, the theoretical background within this work starts with the Euler-Bernoulli and, subsequently, the Timoshenko beam theory. These two fundamental theories qualify the standard model of a cantilever, independent of its mounting (e.g. single- or double clamped) by choosing the appropriate boundary conditions.[xii] The following equation, the Euler-Bernoulli equation, is the most general way to describe a single cantilever:

$$\frac{\partial^2}{\partial x^2}\left(EJ_{yz}(x)\frac{\partial^2\psi}{\partial x^2}\right)+\rho A(x)\frac{\partial^2\psi}{\partial t^2}=q(x,t) \tag{2}$$

This partial differential equation of 4th order is described by the young's modulus E[xiii] which will be described later, J_{yz} the geometrical moment of inertia of the present cross section $A(x)$ and the mass density ρ. The transvers loading is represented by $q(x,t)$. The anisotropic SOI wafer used for this special case will be described in a later chapter.

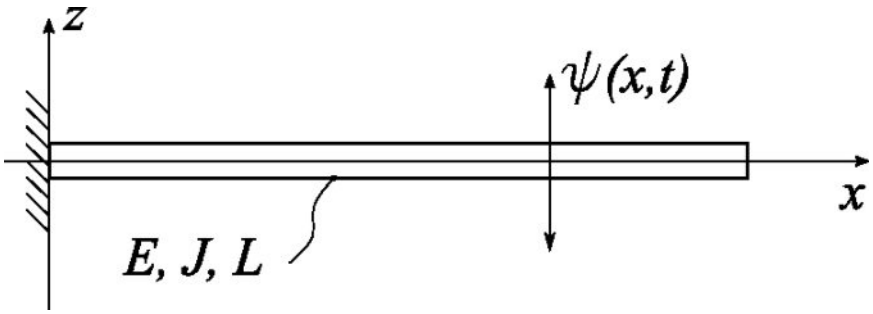

Figure 5: single clamped cantilever with constant geometrical moment of inertia and material characteristica over the entire length.

The term $EJ_{yz}(x)$ represents the bending stiffness of the cantilever and is the most important factor to determine the eigenfrequencies of the cantilever. ψ is the displacement of the beam in the z-direction[7].

The following equations simplify the Timoshenko theory:

$$M = -EJ_{yz}(x)\frac{\partial^2\psi}{\partial x^2} \quad \text{and} \quad \frac{\partial M}{\partial x} = F = -EJ_{yz}(x)\frac{\partial^3\psi}{\partial x^3} \tag{3}$$

Here, *M* is the bending moment of the beam and *F* is the shearing force. With a constant cross section over the complete length, $J_{yz}(x)$ is independent of the longitudinal coordinate *x* ($J_{yz}(x) \longrightarrow J_{yz}$). By separating *X* and *T,* the equilibrium conditions can be described as follows:

$$\frac{\partial F}{\partial x} = -q \tag{4}$$

$$EJ_{yz}\frac{\partial^4\psi}{\partial x^4} = -\frac{\partial^2 M}{\partial x^2} = q \tag{5}$$

The equations are used for a single clamped cantilever by solving the eigenvalue problem with a separation ansatz. It should be noted that these equations are limited to the length of the cantilever if the Poisson's ratio ν[xiv] is negligible.

$$\psi(x,t) = X(x)T(t) \quad \text{and} \quad T(t) \propto e^{-i\omega t} \tag{6}$$

In this case, using $\beta = \frac{\rho A}{EJ_{yz}}$, the Euler-Bernoulli equation becomes

$$\frac{\partial^4\psi}{\partial x^4} + \beta\frac{\partial^2\psi}{\partial t^2} = 0 \tag{7}$$

A harmonic ansatz for *X(x) is*

[7] The (static) deflection of the single cantilever as well as in good condition the U-shaped cantilever excited by the Lorentz force is given by the following: $F_L = I \cdot B \cdot L$ (with *I* as the current; *B* is the magnetic flux density and *L* the length of the current carrying conductor); deflection $W(l) = \frac{F_L \cdot l^3}{3EJ}$.

$$X(x) = C_1 \cos(\beta\omega^2 x) + C_2 \sin(\beta\omega^2 x) + C_3 \cosh(\beta\omega^2 x) + C_4 \sinh(\beta\omega^2 x) \quad (8)$$

The boundary conditions for a single clamped cantilever, in fact of zero bending moment and zero shearing force at the tip of the beam, are:

$$\psi(0) = \psi'(0) = \psi''(L) = \psi'''(L) = 0 \quad (9)$$

Solving the eigenvalue problem with these boundary conditions, the characteristic polynomial and the geometric Eigenfrequencies[xv] become $1 + \cos(\kappa_i L)\cosh(\kappa_i L) = 0$

$$\kappa_i = \sqrt[4]{\omega^2 \frac{\rho A}{EJ_{yz}}} \quad (10)$$

Solving the equation of the characteristic polynomial for the first three modes, we get $\kappa_1 L = 1.875$; $\kappa_2 L = 4.694$ and $\kappa_2 L = 7.855$. The eigenfrequencies become:

$$\omega_i = {\kappa_i}^2 \sqrt{\frac{EJ_{yz}}{\rho A}} \quad (11)$$

The Timoshenko beam equation includes the shear deformation in the cantilever. These deformations have an effect if the following condition cannot be met, where G is the shear modulus:

$$\frac{EJ_{yz}}{\nu\, A\, G\, L^2} \ll 1 \quad (12)$$

Equation 12 is the relation between bending stiffness and shear stiffness times length square and means that the Euler Bernoulli beam has a higher stiffness overall than the Timoshenko beam which is given by the following equation:

$$\frac{\partial^2}{\partial x^2}\left(EJ_{yz}(x)\frac{\partial^2 \psi}{\partial x^2}\right) + \rho\, J_{yz}\frac{\partial^2 \psi}{\partial t^2} + \nu\, A\, G\, \frac{\partial\ \psi}{\partial x} = q(x,t) \quad (13)$$

2.2 The U-shaped cantilever

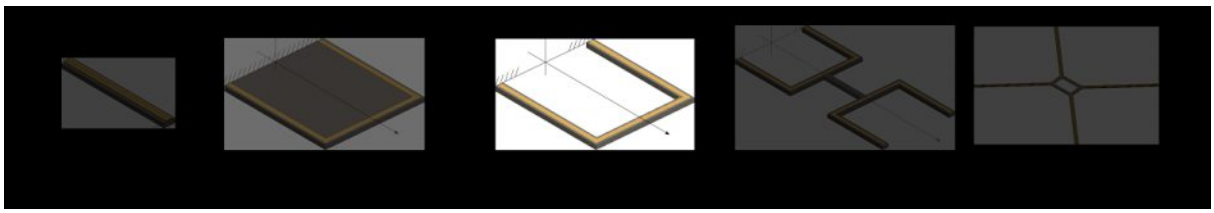

In case of the U-shaped cantilever, we add an additional tip mass to simulate the crossbeam and assume that the geometrical moment of inertia J_{yz} is equal for the single cantilever as well as the U-shaped one. The additional boundary condition, which constitutes the shear force at the tip of the cantilever, in respect of the tip mass is:

$$\psi'''(L) + {\kappa_i}^4 \, \mu \, L \, \psi(L) = 0 \tag{14}$$

with the mass ratio μ.

$$\mu = \frac{m}{\rho A L} \tag{15}$$

In this case, the mass m represents the cross beam of the U-shaped cantilever and A is the cross section of both cantilevers in x-direction. The characteristic polynomial with this new boundary condition extends to

$$1 + \cos(\kappa L)\cosh(\kappa L) + \mu \, \kappa \, L[\cos(\kappa L)\sinh(\kappa L) - \sin(\kappa L)\cosh(\kappa \mathrm{L})] = 0 \text{ [xvi]} \tag{16}$$

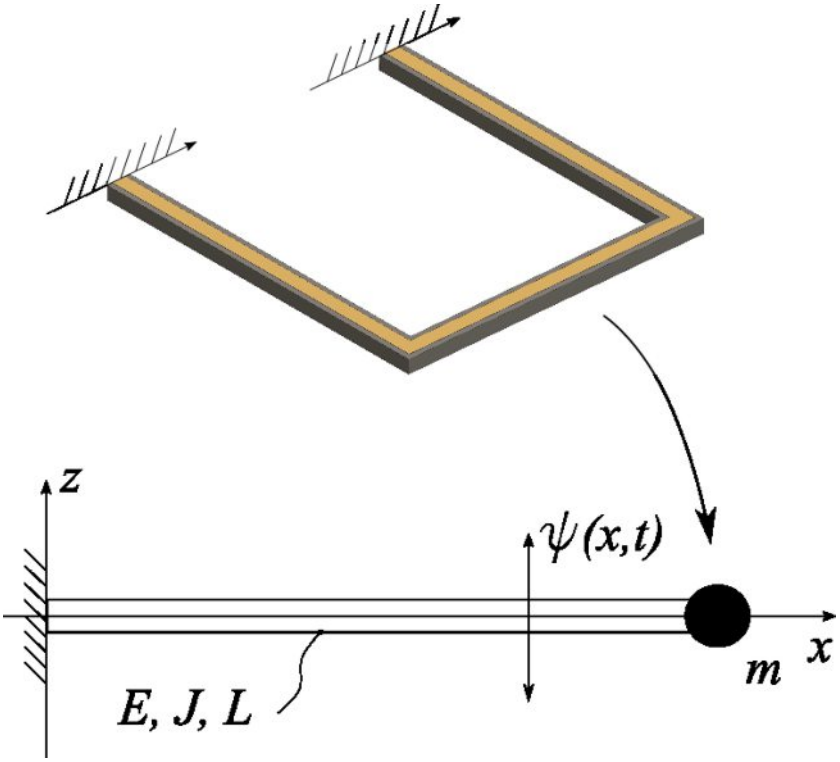

Figure 6: Analytical model for the U-Shaped Cantilever with an additional mass on the tip of a single clamped cantilever instead of the cross beam.

This approximation of the U-shaped cantilever loses its validity at higher vibration modes compared to FEM simulations as done by Stifter (iv), e.g. because the single cantilever's tip mass neglects the bending as well as the wide of the crossbeam.

2.3 Magnetic field gradient structures

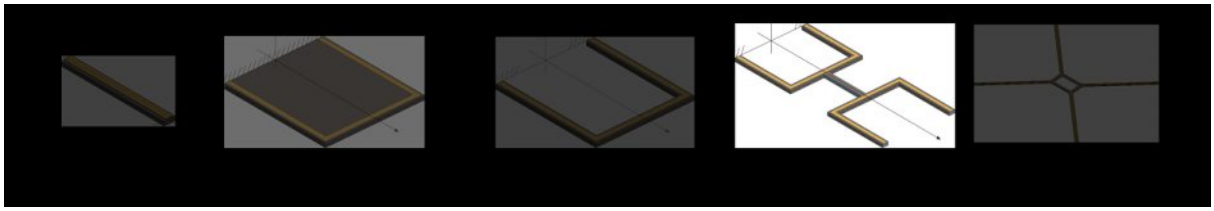

As described in the previous chapter, the investigated cantilever is a double U-shaped structure with an additional coupling bar between the two substructures to measure the magnetic flux density gradient. The coupling bar aligns the vibration of both structures, which have small differences in their resonance frequency due to manufacturing tolerances.

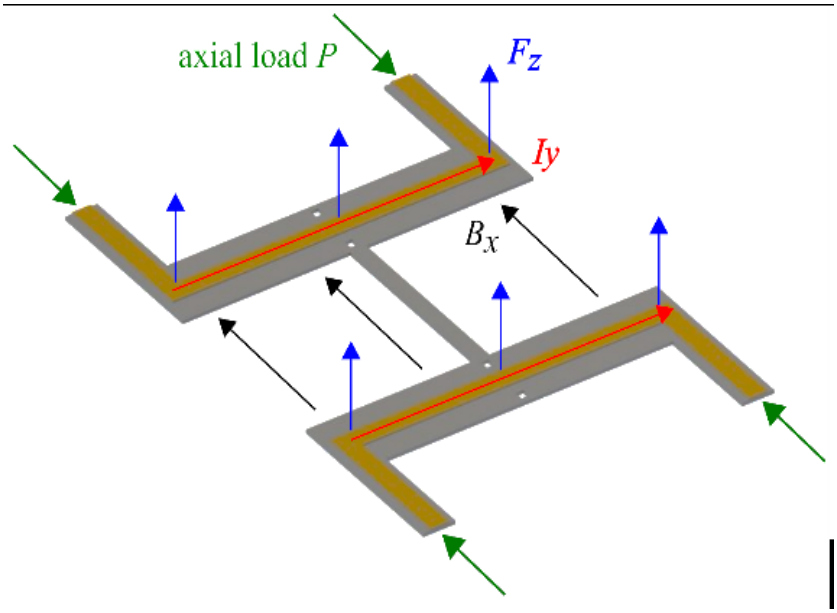

Figure 7: Double U-shaped structure, parallel excitation mode, magnetic flux density and gradient in x-direction

The structures are Lorentz force driven as depicts in figure 7. If the magnetic flux density (z-direction) is perpendicular to the crossbeams, the remaining leads (x-direction) are negligible due to the excitation of the vibration modes. The Lorenz force, based on Faradays induction law[xvii], acts on the structure in z-direction is described as

$$\overrightarrow{F_z} = L_{yy}\,\overrightarrow{I_y} \times \overrightarrow{B_x} \quad \overset{I \perp B}{\longrightarrow} \quad = L_{yy}\,\overrightarrow{I_y}\,\overrightarrow{B_x} \tag{17}$$

The measurement signal of a magnetic flux density gradient in x-direction is the difference of the deflection amplitude between the both crossbeams. To reduce the required current strength of the sensing element and thus an unwanted self-heating of the structure the sensor works in a frequency selective system near to the resonance frequencies of the mechanical

structures. Therefore, the quality factor Q is the most important index to describe a mechanical resonator. There are different ways do estimate the Q factor like the bandwidth method[xviii] or the logarithmic decrement method.

The Q factor can be described as

$$Q = \frac{\omega_0}{\Delta\omega} \tag{18}$$

Where ω_0 is the resonance frequency and $\Delta\omega$ the frequency gap at half high of the resonance peak. In a resonant vibration mode, the signal of the resonator amplifies with the Q factor around the resonance frequency. A complete calculation of the quality factor can only be approximated for complex structures as seen in [XVIII] and perfectly summarised and reprocessed by S. Schmid. A reduction of the Q factor is mostly induced by damping mechanisms[xix] like clamping, friction, surface-friction, thermo elastic damping (TED) and in case of double clamped beams – dilution damping.

The simplified model for an analytical calculation of the flux density gradient structure is a double clamped cantilever with an additional mass in the middle (see Figure 10). The calculations and the FEM simulations are in good agreement with the measurements for the first symmetric and the first anti-symmetric mode (see chapter 4.4.5 Table III). The same model is also applied for the cross shaped displacement sensor structure in the following chapter.

Special contributions will be made to the coupling bar, which interconnects the two U-shaped substructures. For small flux density gradients, a larger width between the two crossbeams enables a higher sensitivity of the sensor while keeping the spring constant of the crossbeam constant. The variable parameter of the coupling bar is the width *b,* which influences the coupling factor of the interconnection (XI).

Γ means the width of the resonance peak at half high, is represented by $\Delta\omega_s$ which is the difference between the resonance frequencies of the coupled resonators.

$$\Gamma = \Delta\omega_s = \omega_2 - \omega_1 = \frac{k_c}{k_R}\omega_1 \tag{19}$$

With k_c is the spring constant of the coupling bar and k_R of the resonator. Both are mostly determined by the Young's modulus, which is constant all over the structure. For $\Delta\omega_s \ll \Gamma$ we are in the strong coupling regime.

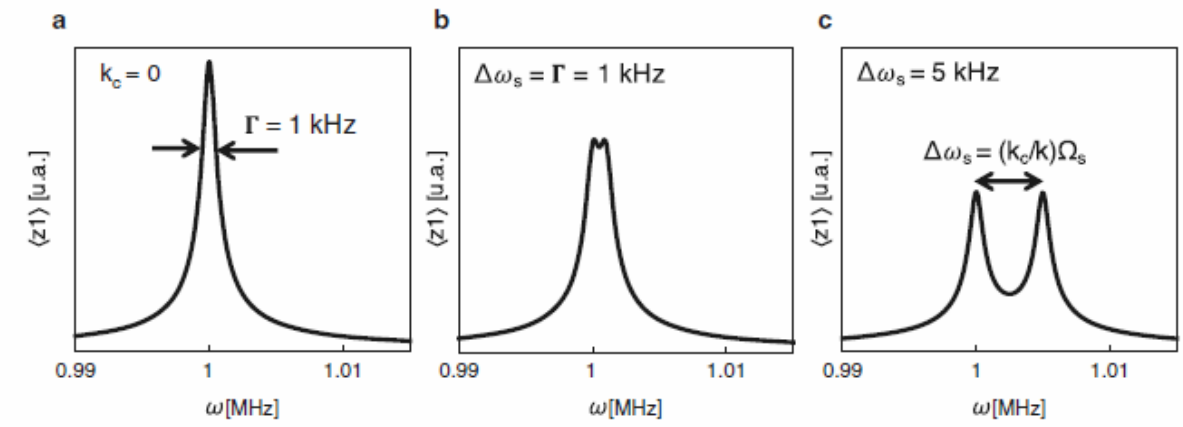

Figure 8: Resonant amplitude over frequency. a: two strongly coupled resonators; b: resonance gap with $\Delta\omega_s$ in the scale of Γ; c: weak coupling of two resonators. Figure adopted from [xix].

Too weak of a coupling creates a resonance frequency gap between the two sub structures which means an unequal amplification between these both sub-structures while exciting the sensor with an single frequency signal. This also means a variation in the deflection of the U-shaped cantilevers regarding to a change in the magnetic flux density.

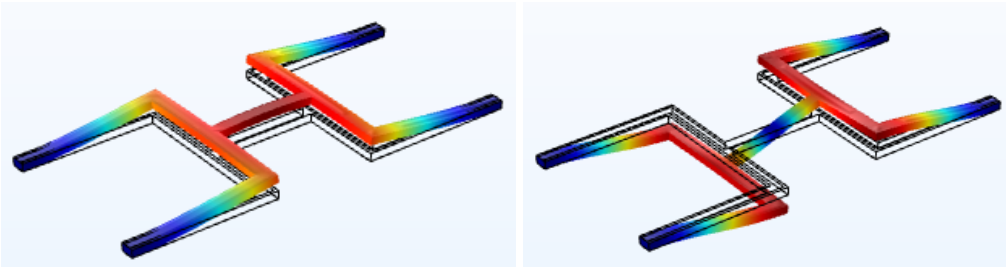

Figure 9: left: first symmetric mode of the double U-shaped structure; right: first anti-symmetric vibration mode

Creating an analytical model, the geometrical boundary conditions of the both sided clamped double U-shaped structure is given as:

$$\psi(0) = \psi'(0) = \psi(L) = \psi'(L) = 0 \tag{20}$$

In the following, a case discrimination between symmetric and anti-symmetric vibration modes creates different boundary conditions:

For symmetric modes

$$\psi'\left(\frac{L}{2}\right) = 0 \qquad \psi''(0) = \psi''(L) \tag{21}$$

and for anti-symmetric modes

$$\psi''\left(\frac{L}{2}\right) = 0 \qquad \psi''(0) = -\psi''(L) \tag{22}$$

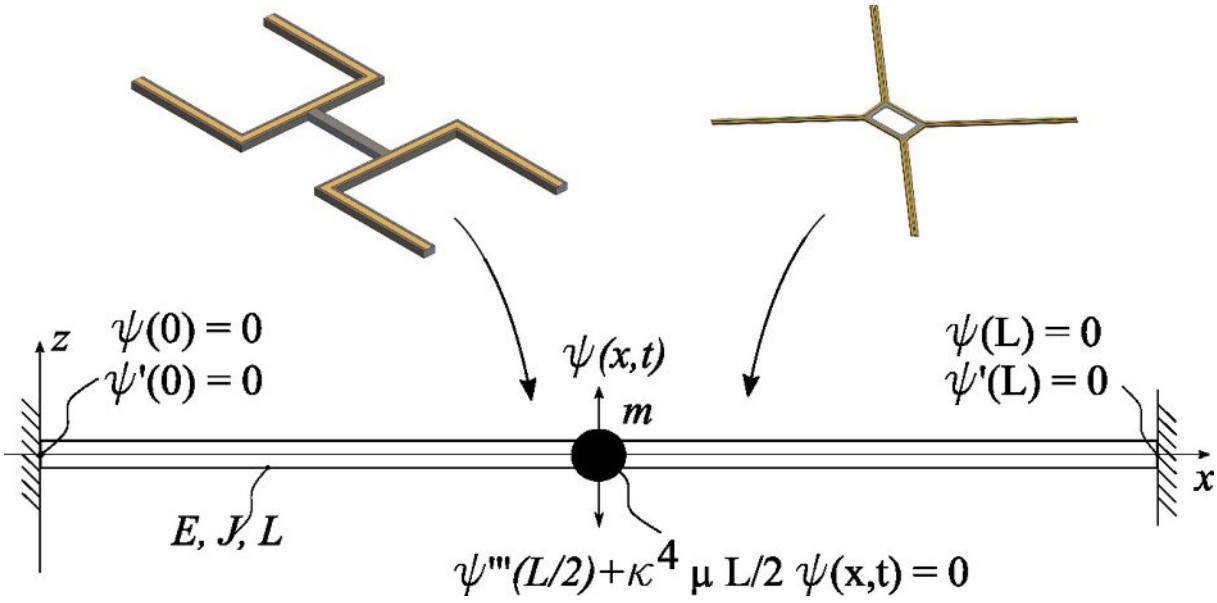

Figure 10: Double clamped cantilever as analogous model for the double U-shaped as well as the cross-shaped structure.

In Figure 10 *m'* is the reduced mass out of the two cross beams as well as the coupling bar which influences the mass ratio μ:

$$\mu = \frac{m'}{\rho A L} \tag{23}$$

With the given set of boundary conditions (equation 20 and 21), the eigenvalue problem can be summarised to the characteristic polynomial:

$$\cos(\kappa L)\sinh(\kappa L) + \cosh(\kappa L)\sin(\kappa L) + \kappa\mu L\cos(\kappa L)\cosh(\kappa L) - 1 = 0 \tag{24}$$

Depending on the mass ratio μ, we can distinguish three cases:

$$\mu = 0 \longrightarrow \kappa_1 L = 0{,}501;\ \ \kappa_2 L = 2{,}212;\ \ \kappa_2 L = 5{,}504 \tag{25}$$

$$\mu = 1 \longrightarrow \kappa_1 L = 0{,}334;\ \ \kappa_2 L = 1{,}810;\ \ \kappa_2 L = 4{,}883 \tag{26}$$

$$\mu \gg 1 \longrightarrow \kappa_1 L = 1{,}571;\ \ \kappa_2 L = 4{,}712;\ \ \kappa_2 L = 7{,}854 \tag{27}$$

$\mu = 0 \longrightarrow$ Represents a double clamped cantilever without an additional mass in the middle.

$\mu = 1 \longrightarrow$ Is the most representative case for the given cantilever.

$\mu \gg 1 \longrightarrow$ Theoretical model for a large additional mass on a string.

2.3.1 Nonlinearities occurring at double clamped cantilevers

The two main sources of nonlinearities are material effects and geometric nonlinearity. The nonlinearities of the material, described by the enlarged Hooke's law (equation 28). While in most cases small deflections result in linear behaviour between stress and strain, larger deflections are the reality. Even the Young's modulus has nonlinearities, which is described in the enlarged Hook's law[xx]:

$$\sigma = E_0\varepsilon + E_1\varepsilon^2 + \cdots \tag{28}$$

The second part is the geometric nonlinearity which is most influenced by the clamping and the cantilever type. An example is the structure type as seen in Figure 10, a double clamped cantilever. The main parameter is spring hardening by elongation of the deflected cantilever[xxi]. The spring constant of the resonator k_R enlarges to:

$$k_R = k_{R0}(1 + k_{R1}x + k_{R2}x^2 + \cdots) \tag{29}$$

The material nonlinearity is a restriction for sensors measuring the deflection, like the Lorentz force driven magnetic field sensors described above (chapter 2.2), where the measuring range is limited due to the nonlinear effects at higher deflections. The geometric nonlinearity effect affects sensors measuring the resonance frequency like the PikoSens micro displacement sensor (chapter VI) or the chemical sensor by H. Lang et. al.[v]. Figure 11 depicts the effect of a nonlinear spring constant on the transfer function.

Figure 11: left: linear response of an oscillator transmission curve; right: the resonance peak is driften to lower frequencies (xxi, p.716)

Geometrical nonlinearity is most seen by bending modes as used in almost every sensor structure described before and often occur parallel with temperature affected effects like buckling due to thermal expansion or otherwise high tensile stresses occurred by thermal contraction.

2.4 Temperature dependency model

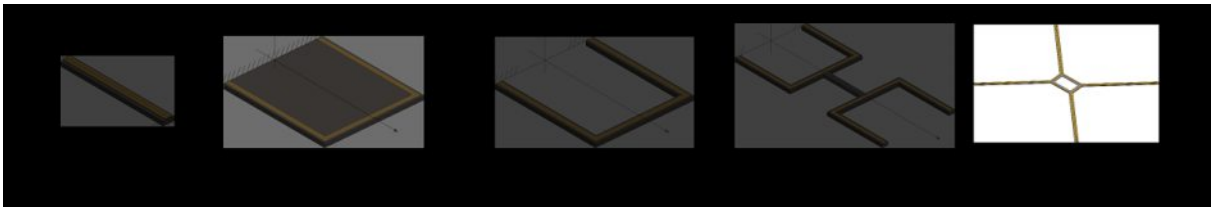

In this section we develop an analytical model for the temperature dependency of the double clamped structures. Main cause for the dependence is the different thermal expansion coefficient of the silicon cantilever and the bulk material. We assume that the thermal expansion reduces the pre-stress of the stretched string (which is the substitute model for the double U-shaped cantilever) without buckling of the cantilever. A useful theoretical model is the "monoaxial constrained thermal expansion prevention" given by the following equation:

$$\varepsilon_x = \varepsilon_{th} + \varepsilon_m = 0 \tag{30}$$

Where the strain ε_x is the relative extension of the double clamped cantilever which can be separated in the thermal expansion ($\varepsilon_{th} = \alpha \cdot \Delta T$) and the mechanical expansion (ε_m) acting against each other.

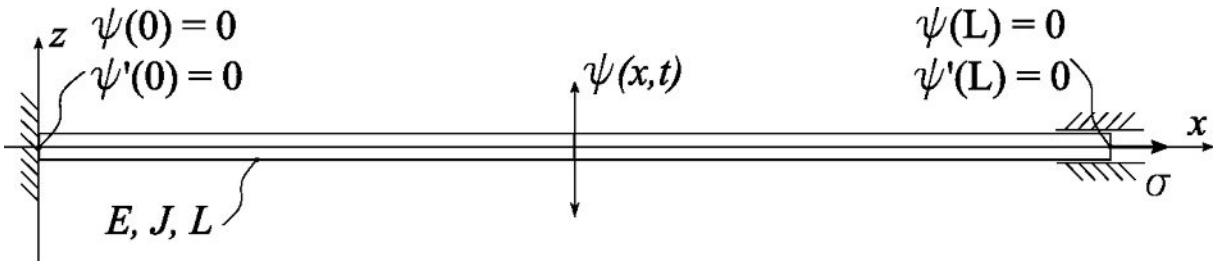

Figure 12: Analogous model for the temperature effected double clamped cantilever under tensile stress σ. Boundary conditions are equal to the simple double clamped cantilever (figure 10).

The occurring stress, which has a linear dependence of the temperature, acting on the cantilever is determined by:

$$\sigma = -E(T) \cdot \alpha \cdot \Delta T \tag{31}$$

$E(T)$ is the temperature dependent young's modulus of silicon which is 130GPa for axial load (e.g. [110] or $[\bar{1}00]$ direction) with an temperature coefficient of -60ppm/K [xxii]. α is the thermal expansion coefficient from silicon (=$1 \cdot 10^{-8}$ 1/K [xxiii]) and ΔT the temperature difference.

The Timoshenko beam theory differential for this model modifies to:

$$\frac{\partial^2}{\partial x^2}\left(EJ_{yz}(x)\frac{\partial^2\psi}{\partial x^2}\right) + \rho A(x)\frac{\partial^2\psi}{\partial t^2} - N\frac{\partial^2\psi}{\partial x^2} = 0 \tag{32}$$

With $N = \sigma A$ is the tensile force acting on the cantilever and $\psi = \psi(x,t)$. We use the same sinusoidal Ansatz as before to solve the eigenvalue problem with the wavenumber κ_i.

$$\omega_i = {\kappa_i}^2\sqrt{\frac{EJ_{yz}}{\rho A}}\sqrt{1+\frac{\sigma A}{EJ_{yz}{\kappa_i}^2}} \tag{33}$$

The eigenfrequencies increase with the tensile stress in the additional term multiplied to the already known term from the unstressed cantilever (equation 10).

The wavenumber κ_i for our cantilever now also depends on the tensile stress and comes from the

$$\kappa_i = \sqrt{\frac{\sigma A}{EJ_{yz}}} \tag{34}$$

2.5 Torsional plate sensing structure

Another interesting structure was created by a double clamped cantilever with a rectangular plate in the middle (Figure 13). It was originally intended for measurements of the magnetic field gradient. This torsional bending structure is excited by two gold conductor paths which carry antiparallel current (in contrast to the bending structures which need parallel currents or a single conductor path).

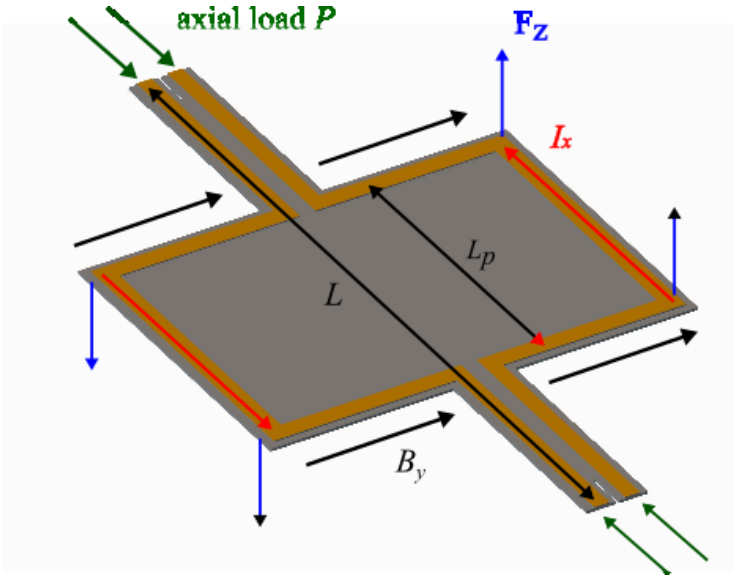

Figure 13: Torsional bending structure represented by a rectangular plate on a double clamped cantilever. The axil load P presents the stress by thermal expansion of the structure. Only the important current carrying parts ae depicted.

The torsional bending structure completes the set of double clamped sensing structures. The following calculations help understand the proportionate torsional twist, depending on the load state, combined with the simple bending oscillation used by the PikoSens structures. In our calculation model we made some concessions to simplify the boundary conditions. First, the length of the plate L_p is much smaller than the complete length of the cantilever L so that due to the smaller torsional stiffness of the cantilever the majority of the torsion occurs in the cantilever while the plate only rotates around the y-axis. Second, the cantilever is long enough that boundary effects of the connection area between plate and cantilever and cantilever and sensor frame can be neglected.

The Timoshenko equation for this model for only torsional modes is described by:

$$\left[GJ_{yz} - \frac{PI_\alpha}{m}\right]\frac{\partial^2\varphi}{\partial x^2} - I_\alpha\frac{\partial^2\varphi}{\partial t^2} = 0 \tag{35}$$

In this model, G is the shear modulus[8] ([xxiv]) and I_α/m the polar mass moment of inertia per unit length and mass[9]. P is the axial load depicted in Figure 13. J_{yz} as already known is the moment of inertia of the complete cantilever, but in good approximation represented by the moment of inertia of the cantilever itself. GJ_{yz} represents the shear stiffness of the cantilever. The boundary conditions for the torsional bending oscillation are given in the following:

$$\varphi(0,t) = \varphi(L,t) = 0 \tag{36}$$

And we get the eigenvalue:

$$\omega_0 = \frac{\pi}{L}\sqrt{\frac{GJ_{yz}}{I_\alpha} - \frac{P}{m}} \tag{37}$$

In contrast to the bending structures, we are only interested in the first vibration mode. The effect of the axial load (e.g. induced by thermal expansion) at the resonance frequency is shown by comparing equations 31 and 37 and is described in detail during chapter 5.4.

[8] Shear modulus $G = \frac{1}{2(1+\nu)}E$ is related to the shear stress by $\tau = G \cdot \tan(\gamma)$ with γ as the rotation angle.

[9] $\frac{I_\alpha}{m} = \frac{1}{12}(b^2 + h^2)$ with b is the wide of the cantilever and h is the high.

2.6 Contribution to publications

The second part of this work is represented by six publications, commencing with the µ-wire magnetic field sensor we tested at the CERN laboratories (publication I), the magnetic field gradient sensors (publications II and III) and the multiaxial force sensor (publications IV and V). At least the issued patent containing the micro newton force sensor (publication VI). In the following breakdown there are my contributions to the individual publications (expect publication six):

- M. Stifter; "MEMS µ-wire magnetic field detection method@CERN."; IEEE Sensors Journal, 15717295, 2015 vol2
  Co-author; in print
  Internet publication: https://ieeexplore.ieee.org/abstract/document/7370244
  25%

- A. Dabsch, "MEMS cantilever based magnetic field gradient sensor", Journal of micromechanics and microengineering, vol 27 no 5, april 2017
  Lead author; in print
  Internet publication: https://iopscience.iop.org/article/10.1088/1361-6439/aa654f/meta
  75%

- A. Dabsch; "Temperature dependency of solicon structures for magnetic field gradient sensing"; Journal of Micromechanics and Microengineering; July 2017
  Lead author; in print
  Internet publication: https://iopscience.iop.org/article/10.1088/1361-6439/aa7d28/meta
  75%

- A. Dabsch; "Multiaxial Resonant MEMS Force Sensor"; Journal of Micromechanics and Microengineering; vol 28 no 10; june 2018
  Lead author, in print
  Internet Publication: https://iopscience.iop.org/article/10.1088/1361-6439/aac13e/meta
  90%

- A. Dabsch; "Two dimensional displacement measurement with MEMS structure"; Journal of Micromechanics and Microengineering
  Lead author, under review
  90%

Publications one was the first work I was able to join at the institute and I was glad to find a motivated team that enables me to contribute to a degree that I also join the research stay at the CERN in Geneva. I created the pcb with the belonging readout circuit and was responsible for the complete measurement setup and the equipment.

Publications two to six where caused mainly under my responsibility. I made the design for the new magnetic field gradient sensors because I was not able to measure the measurement signals as accurate as I want to and finally I designed the multiaxial force sensor after I read a paper about the challenging measurement tasks in medical technology, particular for meniscus prosthesis. Therefore publication six is mainly instigated by me with the help of Prof. Franz Keplinger.

III. Publication One

MEMS μ-Wire Magnetic Field Detection Method@CERN

Authored by M. Stifter, H. Steiner, W. Horschitz, T. Sauter, T. Glatzl, A. Dabsch and F. Keplinger
Published in: 2015 IEEE SENSORS

Abstract

This work reports a novel construction of amicromachined MEMS magnetometer detecting static magnetic fields of CERN's reference dipole with a custom made capacitive read-out. The magnetic flux density is characterized via vibration modes of the MEMS structure which are sensed capacitively. The device consists of a single-crystal silicon clamped-free plate (cantilever) carrying a thin conductor. The cantilever and thin film metal electrodes are separated by a small gap, building a vibrating plate capacitor. Movements of the cantilever are read out conveniently by electronic circuits. A static magnetic field generates a force density acting on the conductor that alternates according to the frequency of the current. By knowing the electrical current, the deflection amplitude of the cantilever is a measure of the component of the magnetic flux density that points perpendicular to the current. The highest vibration amplitudes are expected, of course, in the vicinity of resonance frequencies of the micromachined structure. At ambient pressure the prototype sensor has a measured resonance frequency of 3.8 kHz for the fundamental mode and 20 kHz for the first antisymmetric mode. In experiments, the magnetic flux of the dipole has been characterized between 0.1 and 1 T, with a relative uncertainty of $3 \cdot 10^{-4}$.

3.1 Introduction

The experimental focus of this work was on developing a resonant MEMS magnetic field sensor with a capacitive readout. A Lorentz-force actuated MEMS cantilever was designed, fabricated and characterized as magnetometer for both static and alternating magnetic fields.

Emphasis was laid on both the optimization of the sensitivity of the mechanical resonator and the characterization of the sensor over many orders of magnitude. The sensor is based on a novel hybrid design, with two independent wafers (silicon and Pyrex), which are mounted on top of each other with a custom SU-8 bonding process. All process steps are carried out on wafer level, except the contacting one with the silver conductive paste. The applied frequency-selective measurement method of mechanical oscillations provides an alternative to the common broadband measurement techniques. The transducer depicted in Fig. 1 measures preferably at resonance, where it rejects broadband interfering signals efficiently because of the considerable resonant enhancement [1]. If the interfering frequency components do not match the resonance frequency, they are effectively suppressed by the transducer. With a careful design, resonators made of monocrystalline-silicon can reach remarkable high quality factors of the order 10_2 to 10_4 [2].

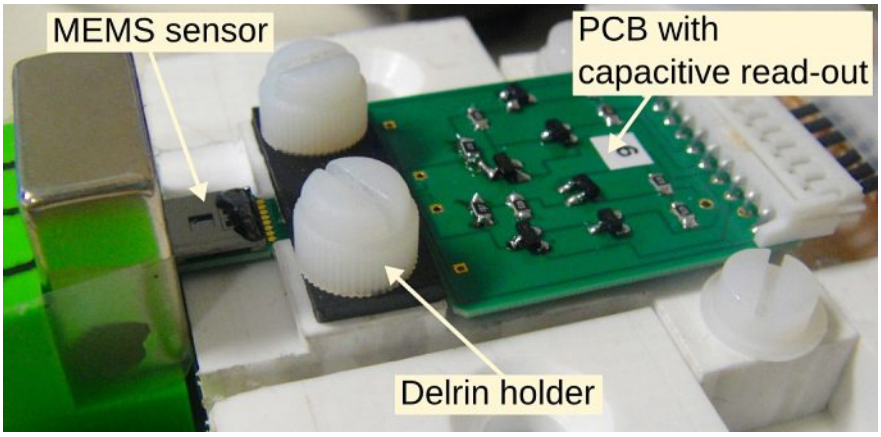

Fig. 1. Setup for the characterization of the MEMS sensor for magnetic flux densities in the range of 0.1 to 1 T.

The oscillatory movement is measured capacitively. An electrostatic force on the mass of the oscillating cantilever is imposed by the sensing electrodes and decreases the resonance frequency. The stability of such structures is possibly deteriorated by the occurrence of a strong electrostatic softening mechanism [3, 4, 5]. Besides fundamental properties, such as the resonance frequency or the band-width of the resonance peaks, nonlinearities were analyzed to develop guidelines for the improvement of the transducer's sensitivity [6]. Ideally, the resonance frequency is independent of the vibration's amplitude, but in nonlinear systems like the cantilever subjected to an amplitude- dependent electrostatic force, the resonant frequency depends on operating conditions and the amplitude response can exhibit hysteresis phenomena [7, 8]. Additionally to the excitation of the mechanical structure at its natural resonance, higher modes are also possible, that allow to suppress acoustic interferences.

For the development of the whole microelectromechanical system a comprehensive characterization of the structures is necessary. The analog signal acquisition is based on the evaluation of the readout capacitor with a high impedance source follower enabling for low system nonlinearity. The operating range regarding the magnetic flux density can be varied over several orders of magnitude by changing the excitation current.

3.2 Device Fabrication

The fabrication process for the device is based on the silicon-on-insulator (SOI) technology, where two monocrystalline silicon layers are separated by a thin layer of silicon dioxide (SiO2). Compared to the use of simple silicon wafers this technology offers a defined etch stop due to the large selectivity of the etchant between silicon (Si) and SiO2. The thicknesses of the device layer and the handle layer are 20 μ m and 350 μ m, respectively.

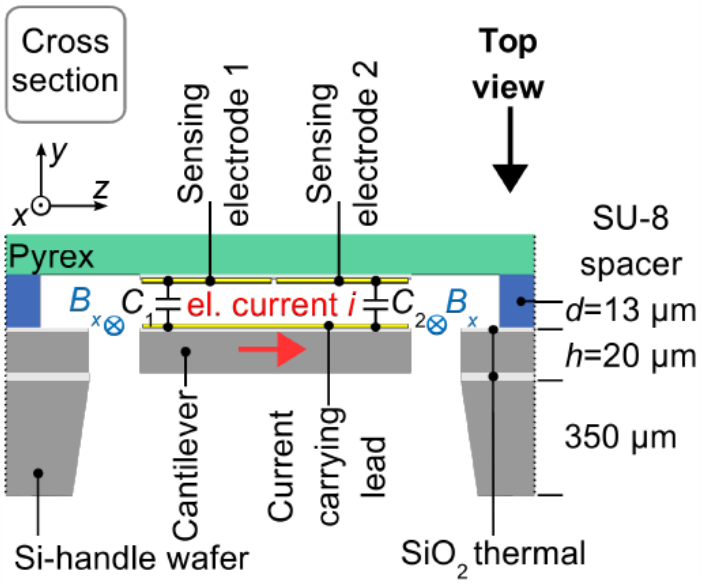

Fig. 2. Schematic cross section of the test device depicting the arrangement of the two sensing electrodes.

The counterpart of the free vibrating planar structure, i.e., the wafer with the sensing electrodes is fabricated on a Pyrex glass-wafer. In Fig. 2 an SU-8 layer is applied on the Pyrex glass-wafer, where a custom SU-8 bonding process on wafer level creates a 13 µm high spacer, which is equal to the equilibrium distance d between the sensing electrodes and the vibrating structure. The two wafers are mounted on top of each other. The geometrical parameters of the MEMS sensor are summarized in Table I.

TABLE I. PARAMETER OF THE CANTILEVER

Length l	2 mm
Width w	1.75 mm
Height h	20 µm
Lead width b_{Au}	70 µm
Electrode gap d	13 µm

3.3 Experimental Setup

The MEMS sensor is placed in the reference dipole of CERN depticted in Fig. 3, with an effective aperture of L = 2.5 m, H = 80 mm and W = 300 mm. The field range of 1 T (stab.: 10-5 T) is monitored continously with an NMR probe (MetroLAB PT 2025) and periodically mapped. Additionally, a Hall probe (FM 302, AS-NTM-2) is placed next to the NMR probe, enabling the measurement of different vector components of the magnetic field.

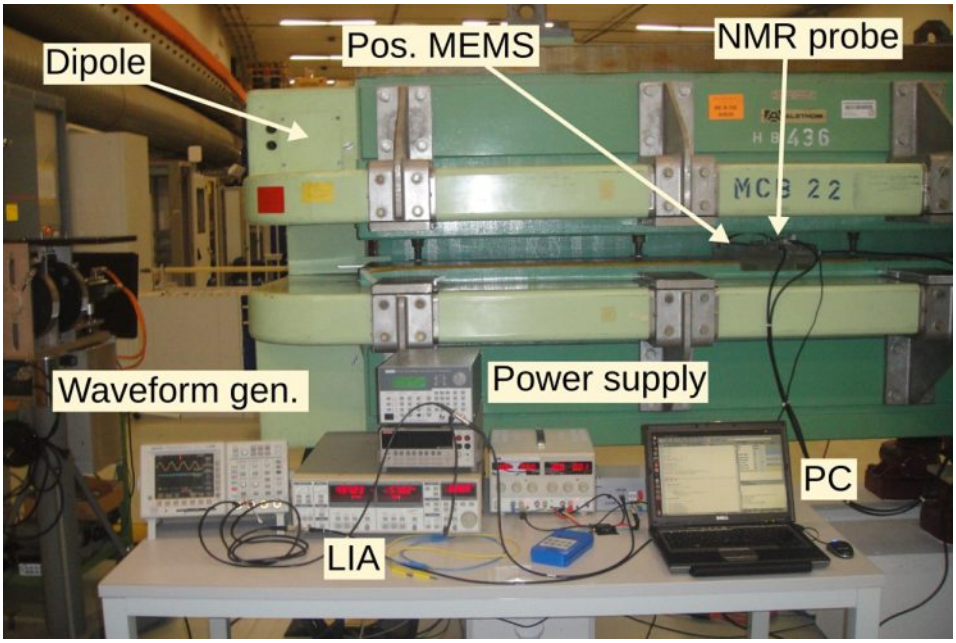

Fig. 3. Characterization of the MEMS sensor in the CERN reference dipole.

Regarding to the orientation of the device in Fig. 4, in respect to the external magnetic field of the dipole, two different families of vibration modes will be favored, namely the first symmetric (S1) and the first antisymmetric mode (AS1).

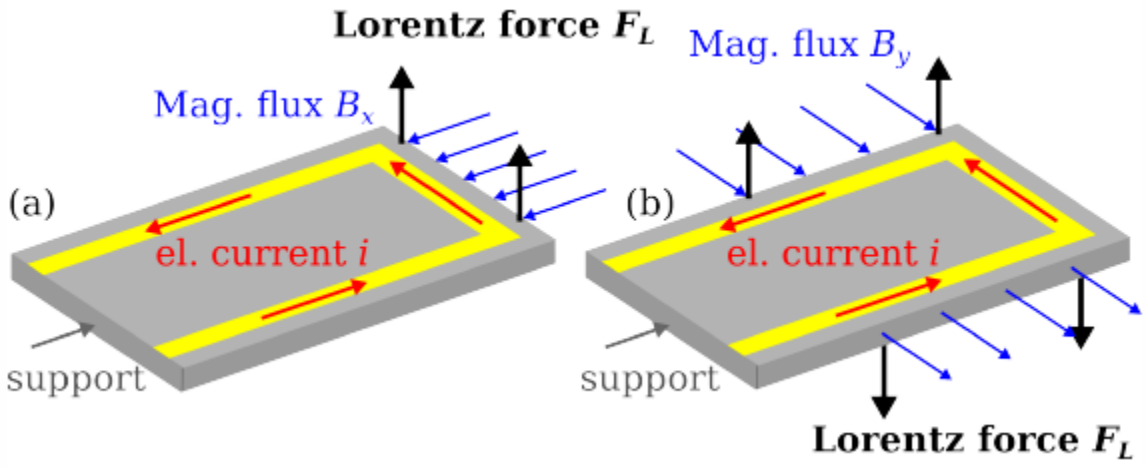

Fig. 4. Schematic views of different vibration mode shapes. (a) Depicts the symmetric excitation mode S1 and (b) the antisymmetric excitation mode AS1 in dependence of the acting Lorentz force.

3.3.1 Measurement Principle

A programmable waveform generator excites the sinusoidal current through the lead, which allows spectroscopy of the mechanical structure oscillations due to the Lorentz force. This technique is very similar to the stretched wire method, but offers the feasibility to measure the variations in the magnetic spatial field and as a result flux linkages with an array of micromachined sensors [9]. A Lock-in amplifier (LIA) is synchronized at the fundamental frequency to measure the output signal of the custom-built capacitive read-out system.

3.3.2 Capacitive Read-Out

In the case of electrostatic sensing, the cantilever is set to a polarization voltage Up to provide the bias for the capacitive detection. The sinusoidal current through the lead is driven by an AC voltage uAC , which combines with the DC voltage Up and forms finally the driving force of the cantilever readout [5].

The capacity C(t) varies according to the motion of the cantilever. Apart from the possibility to control the dynamic behavior of the cantilever through the polarization voltage Up, harmonics with doubled frequency will occur, as a result of the quadratic dependence of the electrostatic force.

A sophisticated kind of source follower, which is capable of measuring changes in the capacitance with a flat transfer function at frequencies from 20 Hz up to 1 MHz, is used as amplifier to sense the cantilever vibrations. In contrast to lowimpedance transimpedance stages that evaluate the current through C(t), the high input impedance of about 50 GΩ at 1 pF ensures low harmonic driving forces by the capacitive read-out. Hence, the amplitude of the cantilever vibration due to the Lorentz-forced excitation is always much smaller than its thickness h as well as its equilibrium distance d between the vibrating cantilever and the sensing electrodes.

3.4 Experimental Results

The measurements related to Fig. 5 were performed at CERN with a cantilever featuring a length of 2 mm, a width of 1.75 mm, and a thickness of 20 μ m.

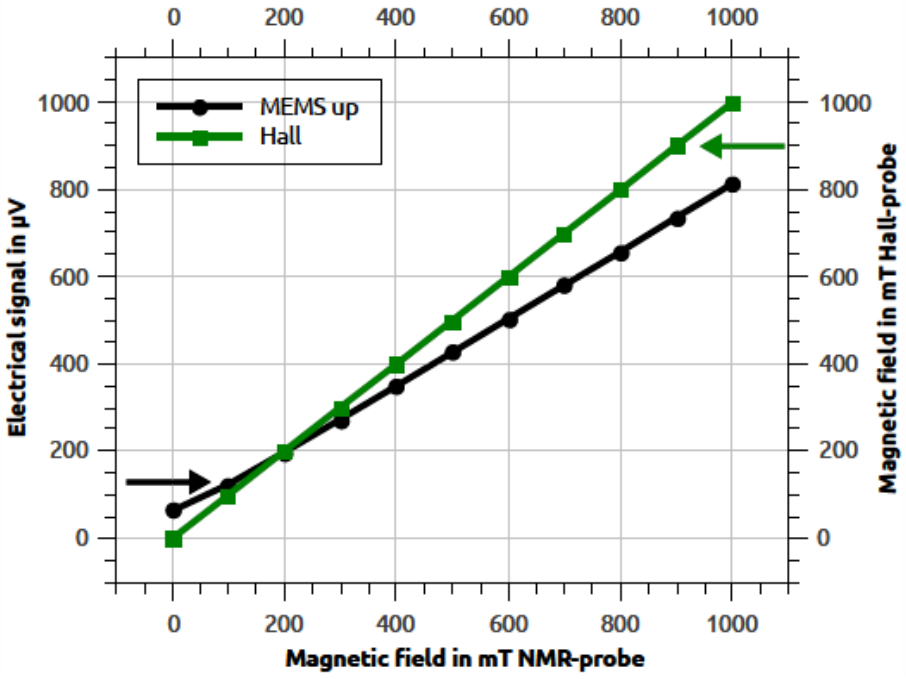

Fig. 5. A comparison of the MEMS sensor with the Hall probe (FM 302, AS-NTM-2), where the magnetic field is ramped up.

The MEMS sensor has been characterized with a Hall probe (FM 302, AS-NTM-2), where the sensitivity depicted in Fig. 5 of the MEMS magnetometer is 80 μ V/100 mT. Below 100 mT a slightly saturation of the signal occurs.

Airborne noise and structure-borne noise introduced by the power supply of the dipole mask the Lorentz force driven oscillations. The offset at the lower bound of the magnetic field is a result of rather different and non-vanishing electrical bias potentials of the independent sensing electronic assemblies connected to the two sensing electrodes. In Fig. 6 and 7, there is a slight hysteretic behavior between 0.1 to 1 T, when the dipole is ramped up and down.

The resonant sensor has been characterized (in the Lab and under vacuum conditions) over six orders of magnitude both capacitive and optical. The sensitivity remained constant with an uncertainty of less than one percent which is similar to the Hall sensor.

Beside the sensitivity the relative uncertainty measured at the fundamental mode (S1) is 3 · 10-3, whereas the relative repeatability uncertainty is 5 · 10-3. The performance of the Lorentz-forced sensor in comparison with the commercial Hall sensor is summarized in Table II.

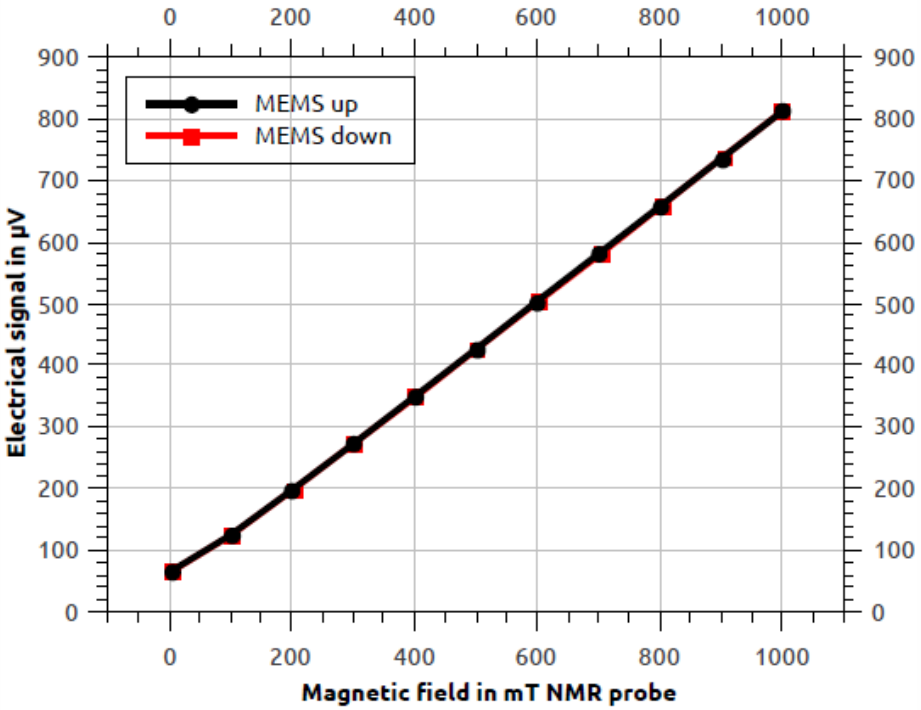

Fig. 6. Dependence of the capacitive electrical signal (vibration amplitude) of the first symmetric mode (S1) on the magnetic flux density for a resonance frequency of 3.8 kHz and the driving current is 1.8 mA.

The benefits of the custom made MEMS sensor are the temperature characteristics and the sensitivity, the handicap is the resolution, but the specifications of the commercial Hall sensor are due to the offset stability of no significance, if the ambient temperature is not monitored to compensate this effect. If, e.g., measurements with a 100 nT resolution are necessary, the temperature has to be kept constant at 33 mK, which is not that easy in non-air conditioned

environments. But the resonant MEMS sensor offers a negligible offset stability (regarding temperature changes). Possibilities to reduce the relative and the repeatability uncertainties are measuring the differential output signal of both sensing electrodes and measuring at higher resonance frequencies to get rid of the ambient noise.

TABLE II. CHARACTERIZATION OF THE MEMS SENSOR WITH A COMMERCIAL HALL PROBE.

	Hall probe FM302, AS NTM-2	*Lorentz-forced sensor with capacitive readout*
Linear range	2T	Custom
Size	5 mm x 70 mm	Custom
Linearity	< 0.1%	< 0.1% (linear regime)
Sensitivity TC	50 ppm/K (up to 500 ppm/K)	28 ppm/K
Offset @25°C	Not specified	Depends on the electrost. config
Noise (0.1-10 Hz)	12 μT_{pp}	250 pT/sprt(Hz)
Hysteresis	Not specified	None
Bandwidth BW	DC – 25 kHz	Several 100 Hz at res. &STP
Power consumption	9 V, 10 mA	20 µW – 20 mW
Offset stability	3 µT	Negligible

When the cantilever is oriented orthogonally with his length to the magnetic field of the dipole as depicted in Fig. 4(b), a first antisymmetric excitation mode is feasible due to the driving current direction. This leads in Fig. 7 to an increase of the system nonlinearity, but also in a decrease of the measurement uncertainty.

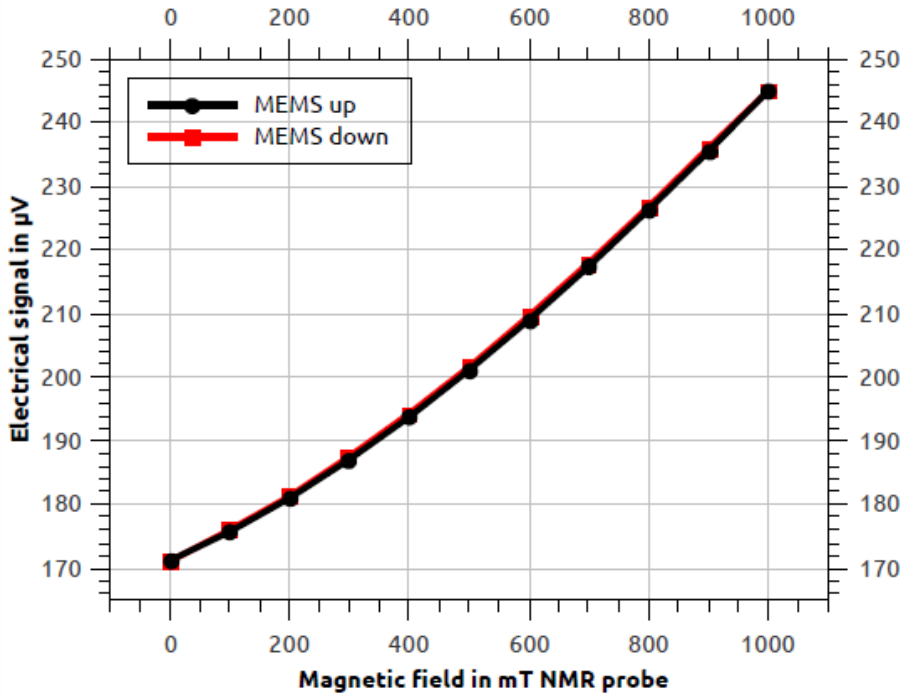

Fig. 7. Dependence of the differential capacitive electrical signal of both sensing electrodes for the first antisymmetric mode (AS1) configuration on the magnetic flux density with a resonance frequency of 20 kHz and the excitation current is 1.8 mA.

Only precise differential measurements at the first antisymmetric mode (AS1) gave satisfying results for flux densities with a relative uncertainty of 3 · 10-4 and a relative repeatability uncertainty of 6 · 10-4.

3.5 Conclusion

A novel design of a micromachined magnetometer to measure both static and alternating magnetic fields was Investigated. The device consists of a single-crystal silicon cantilever which bears a thin conductor carrying an alternating current. The cantilever and thin film metal electrodes form a vibrating plate capacitance. Movements of the cantilever were be read out conveniently by electronic circuits. A static magnetic field evokes a force acting on the conductor that alternates according to the frequency of the current. It is oriented perpendicular to the directions of both the field and the electrical current. Knowing the amount of current, the deflections of the cantilever are a measure of the component of the magnetic flux density that points perpendicular to the current. By changing the drive current, the operating range of the magnetometer can be adapted to cover more than six orders of magnitude. Which resonances are excited depends on the configuration of the field, the electrical current, and most important, on the shape of the resonating structure. In the experiments, emphasis was

laid on the investigation of the first symmetric and the first antisymmetric mode. The resonant enhancement of vibration amplitudes is expressed by the quality factor, which can easily exceed in vacuum a value of 104. At standard pressure, however, values of the order of hundred are typical indicating the impact of gas friction. Magnetic field induced deflections of the cantilever were studied with a custom made capacitive readout. Relative uncertainties of 3 · 10-4 in the range of 0.1 to 1 T were achieved for vanishing DC voltage at the vibrating plate capacitor.

Acknowledgment

The research was funded by the country of Lower Austria (NO), the European Regional Development Fund (ERDF) and the Austrian Science Fund (FWF): L477-N14. We gratefully acknowledge the technical support provided by Dr. Stephan Russenschuck and his team of the Coil Manufacture, Assembly and Calibration Facility at CERN.

3.6 References

[1] F. Keplinger, S. Kvasnica, H. Hauser, R. Grossinger, "Optical Readouts of Cantilever Bending Designed for High Magnetic Field Application," IEEE Transactions on Magnetics, 39, no. 5:3304 - 3306, 2003.

[2] M. Stifter, M. Sachse, T. Sauter, W. Hortschitz and F. Keplinger, "Pressure dependence of the quality factor of a micromachined cantilever in rarefied gases," Journal of Physics: Conference Series, 362, no. 1:1-9, 2012.

[3] M. Stifter, F. Keplinger, H. Steiner, W. Hortschitz, and T. Sauter, "Principles of nonlinear MEMS-resonators regarding magnetic-field detection and the interaction with a capacitive read-out system," Journal of Microsystem Technologies, page 9 p., 2013.

[4] J. F. Rhoads, S. W. Shaw, K. L. Turner, "Nonlinear Dynamics and Its Applications in Micro- and Nanoresonators," Journal of Dynamic Systems, 132, 2010.

[5] M. Stifter, H. Steiner, A. Kainz, F. Keplinger, W. Hortschitz, T. Sauter, "A Lorentz Force Actuated Magnetic Field Sensor with Capacitive Read- Out," Proceedings of SPIE, page 7 p., 2013.

[6] M. I.Younis, MEMS Linear and Nonlinear Statics and Dynamics. Springer New York, 2011.

[7] A. H. Nayfeh, M. I. Younis, "Dynamics of MEMS resonators under superharmonic and subharmonic excitations," J. Micromech. Microeng., 15:1840–1847, 2005.

[8] R. Lifshitz, M. C. Cross, Nonlinear Dynamics of Nanosystems. Wiley- VCH Verlag GmbH, 2010.

[9] P. Arpaia,C. Petrone, M. Buzio,S. Russenschuck, and L. Walckiers, "Multipole correction of stretched-wire measurements of field-gradients in quadrupole accelerator magnets," JINST - Journal of Instrumentation, page 12 p., 2013.

IV. Publication Two

MEMS Cantilever Based Magnetic Field Gradient Sensor

Authored by A. Dabsch, C. Rosenberg, M. Stifter and F. Keplinger
Published in: Journal of Journal of Micromechanics and Microengineering

Abstract

This paper describes major contributions to a MEMS magnetic field gradient sensor. An H-shaped structure supported by four arms with two circuit paths on the surface is designed for measuring two components of the magnetic flux density and one component of the gradient. The structure is produced from silicon wafers by a dry etching process. The gold leads on the surface carry the alternating current which interacts with the magnetic field component perpendicular to the direction of the current. If the excitation frequency is near to a mechanical resonance, vibrations with an amplitude within the range of 1 to 10^3 nm are expected. Both theoretical (simulations and analytic calculations) and experimental analysis have been carried out to optimize the structures for different strength of the magnetic gradient. In the same way the impact of the coupling structure on the resonance frequency and of different operating modes to simultaneously measure two components of the flux density were tested. For measuring the local gradient of the flux density the structure was operated at the first symmetrical and the first anti-symmetrical mode. Depending on the design, flux densities of approximately 2.5 µT and gradients starting from 1µT/mm can be measured.

4.1 Introduction

To measure a magnetic field gradient, normally two or more sensor elements are needed. The most common method applies two hall sensors but these elements suffer from large offsets. An alternative would be a single sensor element that is shifted mechanically requiring an exact positioning system that restricts the applicability. A possible solution are cantilever based sensor systems. Such sensors can be applied for example for MRTs (magnetic resonance tomography) or for dipole characterization (e.g. CERN LHC (Large Hadron Collider) cryodipole [1]) where the sensor can measure local variations of the flux density.

These mechanical based sensors are frequency-selective, e.g. the current over the structure has the same frequency as an eigenvalue of the vibrating structure [2]. This principle allows to avoid interferences with AC-fields of power lines, because the mechanical frequencies are far away from those of technical sources. It is inherent to the design, that both symmetric and antisymmetric modes can be excited at the same time. The individual resonance frequencies of those modes can be designed to differ substantially and do not influence each other. So it is possible to switch between these frequencies to perform different measurements, e.g. to measure the *x*- and *y*-component or a component of the gradient at the same time.

Such frequency-selective-structures operate with high quality factors *Q*, exhibiting high oscillation amplitudes and offering high signal to noise ratios for the readout [3].

One challenge is to handle the temperature dependence of the resonance frequency which causes a shift of the resonant peak. The mechanical temperature dependence of the material is described by the TCE (Temperature Coefficient of Young´s modulus). The TCE of silicon in uniaxial-load cases is approx. -64ppm/°C at room temperature (25°C) and -75ppm/°C at 125°C [3].

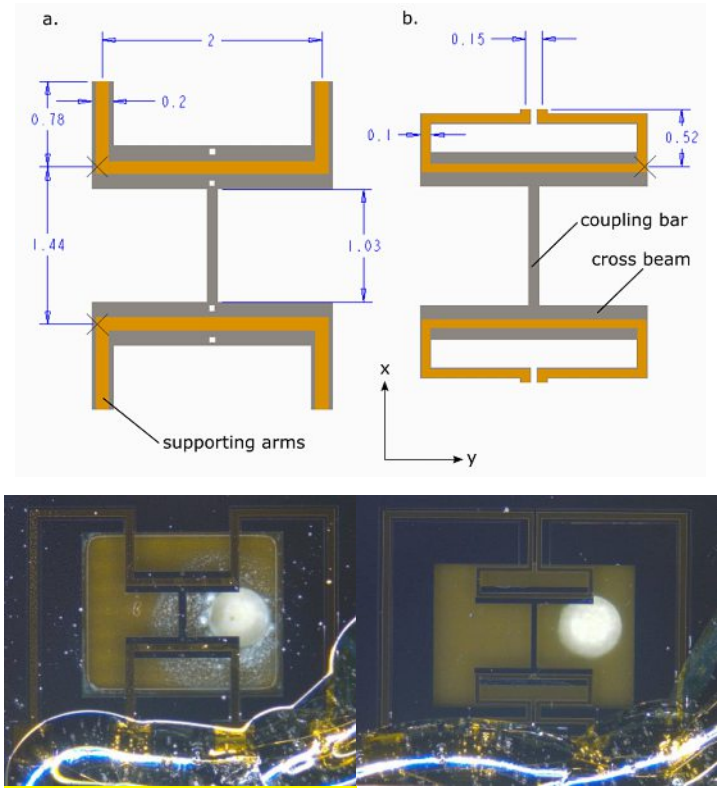

Fig. 1: Design of the two tested structures a) H-shaped-structure b) Ω-structure

Figure 1a depicts a structure that allows the measurement of two components of the flux density (B_x, B_y) and one of the gradient tensor ($\partial B_x/\partial x$). Due to the relative short supporting

arms the temperature dependency of the resonant frequency is relative high. Additionally, the sensitivity for the field in the *y*-directions is much smaller than in the *x*-direction. In contrast, the structure in Fig. 1b enables the measurement of both components with similar sensitivity and with strongly reduced temperature dependency.

4.2 Design

4.2.1 Beam theory

To simplify the mathematical problem, the U-shaped structure is reduced to a simple Euler-Bernoulli-Beam with an additional mass at the ends of each single cantilever (see fig. 2),

where, w is the displacement in z direction, ρ is the mass density, and F_q is the distributed load. Taking a single force instead of the coupling bar is a suitable approximation for symmetric modes.

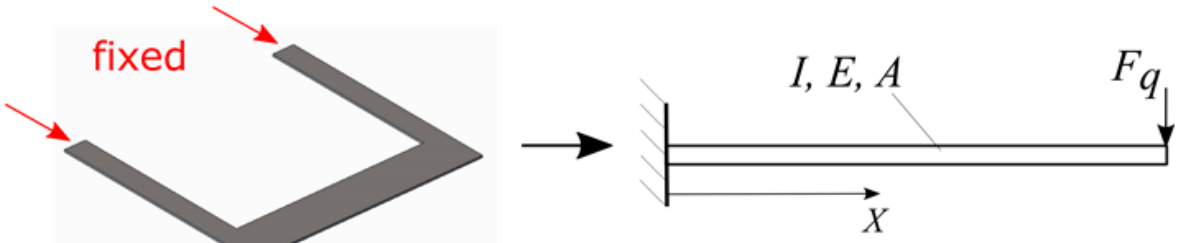

Fig. 2: Model for a U-shaped cantilever. Fq is the replacement force, *E* is the Young´s modulus of the material used, *I* is the second moment of inertia for the specific application, and *A* is cross section of the cantilever.

Solving the Euler-Bernoulli differential equation with respect to the given boundary conditions delivers the characteristic polynomial for the eigenvalues for a U-shaped cantilever.

$$1 + \cos(\kappa L)\cosh(\kappa L) + \mu\,\kappa\, L(\cos(\kappa L)\sinh(\kappa L) - \sin(\kappa L)\cosh(\kappa \mathrm{L})\,) = 0 \qquad (1)$$

with

$$\kappa = \sqrt[4]{\omega^2 \frac{\rho A}{E I_y}} \quad \text{and} \quad \mu = \frac{m}{\rho A L} \quad . \qquad (2)$$

4.2.2 Design of the structures

Measuring a gradient field requires a well-defined distance between the two points of measurement. The coupling bar between the substructures of the MEMS is necessary to couple both structures so that they can vibrate with the same frequency. This is required as the fabrication process always causes some structural differences leading to different resonance frequencies. Especially a temperature gradient can increase this mismatch and deteriorate the measurement [4].

The coupling bar between the two substructures can be represented in the model by the total energy of the coupling structure E_{tot}. It can be divided into two parts. The first one describes the potential energy, which is given by:

$$E_{pot}(y) = \frac{1}{2}\int_0^L \frac{M^2}{EI}\,dz - \int_0^L pw\,dz \tag{3}$$

$$M = -EIy^4 \tag{4}$$

Hence, the first integral is the strain energy and the second the load applied. The kinetic energy, is given by:

$$E_{kin} = \frac{\rho A}{2}\left[\int_0^L \dot{w}^2 dz + \int_0^L L^2\dot{\varphi}^2\right] \tag{5}$$

where the first integral describes the linear movement and the second the rotational energy. In this case $\dot{w}$ represents the linear velocity and $\dot{\varphi}$ is the angular velocity. Therefore, the interconnection for these simple structures can be modelled by the interconnection parameter:

$$K \rightarrow K[f(EI/L_i)]\,, \tag{6}$$

where K is a function of the Young's modulus and L_i is the length of the interconnection. K = 0 corresponds to two single structures with no connection and for K = 1 the same vibration amplitude occurs on both structures. The interconnection parameter cannot be higher than one. The most easily controllable parameter for design is the width b.

$$I = bh^3/12\ . \tag{7}$$

The Young's modulus is given by the wafer's material. The choice of the length *L* of the coupling bar (see fig. 4) determines the sensitivity of the sensor. A short connection bar is suitable for large gradient fields, while small values it has to be elongated at the cost of the spatial resolution [5].

The remaining parameter is the width of the coupling bar. The eigenfrequency of the cantilever depends first on its own and second on the eigenfrequency of the other cantilever due to the coupling bar. A too stiff coupling bar (large width) stimulates the other cantilever too much and a too thin interconnection is not able to compensate the difference between both substructures. A too small width *b* causes a weak coupling between the both substructures due to a smaller stiffness of the coupling bar. Different resonance frequencies of the substructures due to geometrical inaccuracies cause a beat between the bars. A measurement with a test structure with half the width b revealed a too weak coupling. Two slightly different resonance peaks (3961 Hz and 3969 Hz) occur combined with high quality factor and hamper the measurement at a single frequency.

The quality factor *Q* of the system is smaller than that of a single cantilever. Through the interconnection both resonance frequencies of the substructures merge into one mode. With a high quality factor, a minute modification of the resonance frequency causes a substantial change in amplitude (see section IV. B).

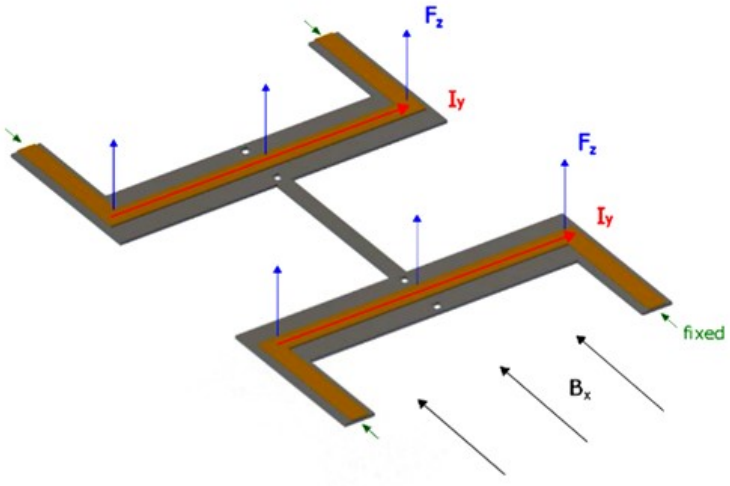

Fig. 3: H shaped cantilever with flux density in x-orientation to stimulate symmetric modes

A noteworthy advantage of the structures is the possibility to sense different orientations of the flux density at the same time. Figure 3 and 4 depict the orientation of the flux density to stimulate symmetric modes at the U-shaped and in the Omega structure. In fig. 5 the

orientation of the flux density and the valid currents to stimulate an antisymmetric mode are depicted.

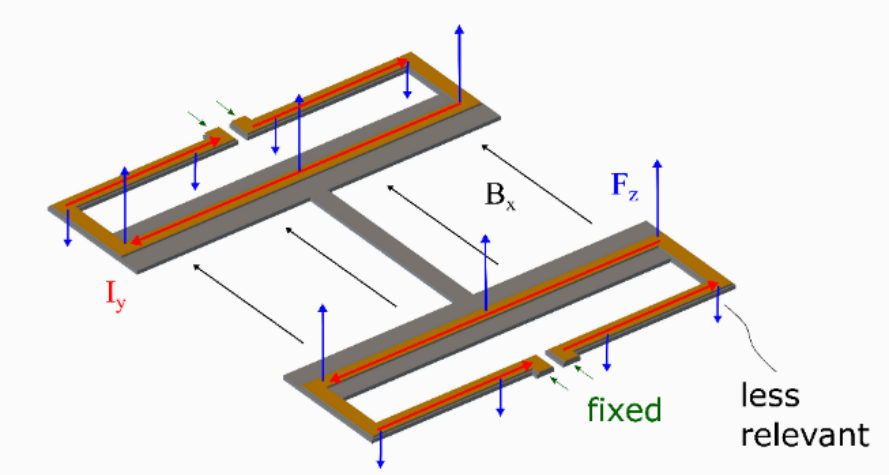

Fig. 4: Ω Structure with flux density in x-orientation and the relevant forces for the symmetric modes

The downwards directed force in Fig. 4 is less relevant, because the much shorter lever arm doesn´t cause a notable deflection.

The pure inplane mode was only excitable in the Ω structure (see fig.6). The necessary force and the field intensity cannot be generated in the *xy* direction of the H-shaped structure without overlap of vibration with other modes. To avoid electromigration the maximum current with respect to the geometry of the gold circuit is restricted at approximate 2 mA for continuous operation and 50 mA for short operations. It is not possible to use higher currents due to the limited thermal conductivity of the wafer under the lead [6]. The Ω structure proves an easier way to stimulate the first inplane mode (lower banding stiffness EI_z).

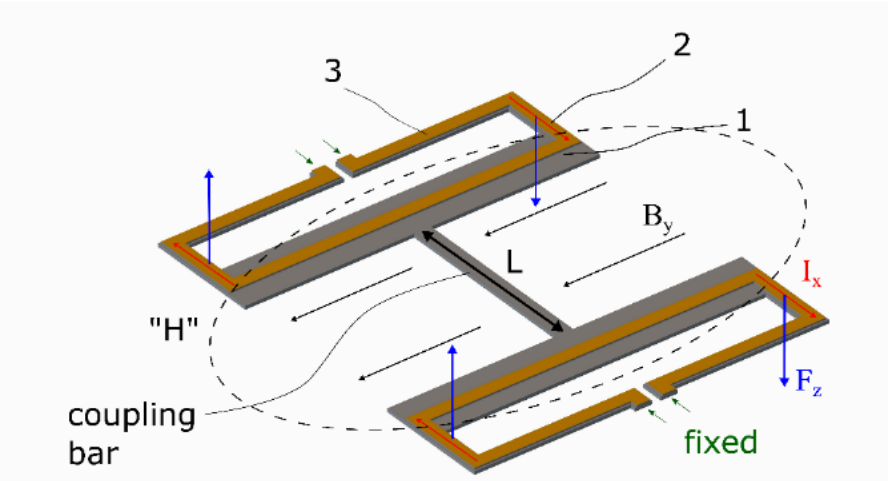

Fig. 5: Ω structure with flux density in y-orientation and the relevant forces for the anti-symmetric mode.

Fig. 6 depicts the setup for field in z direction with the relevant forces to stimulate the first inplane mode. The Lorentz forces acting on the other substructures cancel each other due to the geometry of the sensing structure.

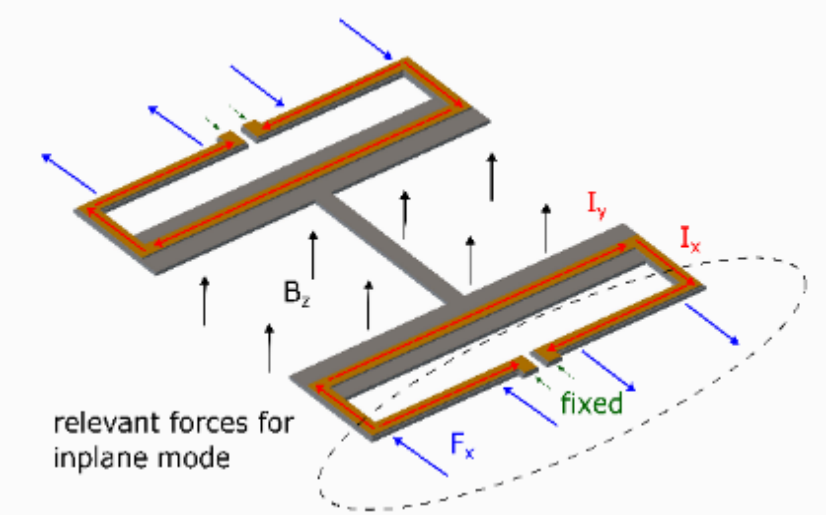

Fig. 6: Ω structure with flux density in z-orientation and the relevant forces for the anti-symmetric mode.

4.2.3 Dimensioning of the Au-leads

The critical current for the leads which is mentioned in section II.B. is calculated according to Blech et. al. [7] considering that the maximal stiffness gradient compensates gaps, generated by electro migration. This is based on occurring alternating tensile and compressive stresses. In the presented structures, tension and compressive stress occurs equally. The supply voltage has no DC-component and, therefore,

$$I_c = \frac{\Omega_a \Delta\sigma}{\rho Z^* e L} A_q \qquad [8] \tag{8}$$

$$\Omega_a = \frac{\Omega}{N_A} \tag{9}$$

TABLE I: Parameters for critical current calculation

Symbol	Quantity	value
A_q	cross section bh	$2 \cdot 10^{-9}\mathrm{m}^2$
L	length	$5 \cdot 10^{-3}\mathrm{m}$
ρ	resistivity	$0{,}022\mu\Omega\mathrm{m}$
Z^*e	specific core length	$4{,}2 \cdot 1{,}602 \cdot 10^{-19}\mathrm{C}$
$\Delta\sigma$	max. mech. stress	$5 \cdot 10^{7}\mathrm{N/m}^2$

Ω_a	atomic value	$10{,}2 \cdot 10^{-6}\mathrm{m}^3/\mathrm{mol}$
N_A	Avogadro constant	$6{,}022 \cdot 10^{23}1/\mathrm{mol}$

Inserting the values of Table 1 delivers a critical current of 2.28mA. This represents the maximum current for a continuous operation to guarantee the mechanical stability of the gold circuit.

4.2.4 Material specification

Silicon, in our case [100] oriented, exhibits an anisotropic Young's modulus with same values in $[\bar{1}10]$ and [110] directions, but reduced values in between. For calculations and simulations, it is inevitable to know the orientation of the structure on the silicon wafers. Especially at antisymmetric modes, torsional load occurs and cannot perceived simplistically. The comparison of the simulated and measured Eigen frequencies in section IV. A. reflects the importance of the different values for each direction in space. With regard to a 3D characterization of the magnetic flux density, the different moduli are advantageous, e.g. for inplane-modes where the stiffness of the material is lower than for the other modes.

4.3 Fabrication

The MEMS structures are fabricated from a 100 mm SOI-wafer built of a 350µm Si handle wafer, 250 nm burried oxide and a 20 µm Si device layer. The SOI wafer is coated on both sides with 70 nm LPCVD (low pressure chemical vapor deposition) silicon nitride.
Sensing structure (front side) and handle wafer (backside) are structured by a DRIE (Deep Reactive Ion Etching) process with 30 wt% KOH solution at 75°C, the oxide layer by hydrofluoric acid. For the electrical connection the sensor is bonded with gold wires to the printed circuit board. The wires are sealed with epoxy resin (UHU® plus rapid). This is applied with a self-built dispenser.

4.4 Results

4.4.5 Simulation

The commercial tool COMSOL Multiphysics V5.2 is used to perform the FEM (finite elemente methode) simulation. The structures are designed in PTC® Creo Parametrics.

TABLE II: Material parameters for simulation (*depending on crystal orientation of the silicon wafer)

Symbol	Quantity	value
E	Young's modulus*	170 / 147 GPa
ν	Poisson ratio*	0.28/0.2
k	Thermal conductivity	130 W/mK
ρ	Concentration	2329 Kg/m³
$\boldsymbol{\alpha}$	Thermal cofficient of expansion	$2.6 \cdot 10^6$ 1/K
$\mathbf{c_p}$	Heat capacity	700 J/kgK

The elements of the stiffness matrix (see table II) are chosen for a [100] wafer as listed in [9]. Figure 7 and 8 depict the first and second symmetric mode of an Omega structure. Comparison with Figure 12 and 13 reveal the additional bending at the cross beam from the U-shaped structure.

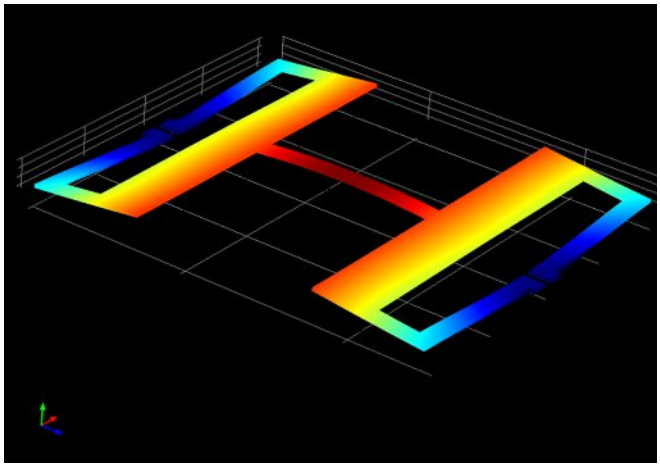

Fig. 7: First symmetric mode at 8.156 kHz, with current in parallel direction.

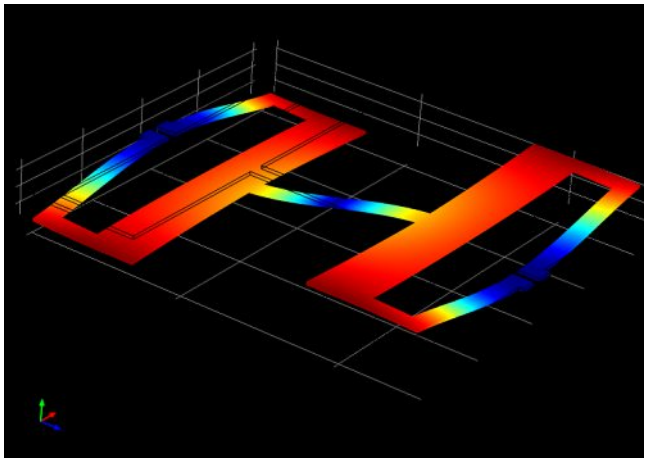

Fig. 8: Second symmetric mode at 13.432 kHz, with current in antiparallel direction.

In Fig. 9 and 10 the first and second asymmetric mode of the Omega shaped structure is pictured. There is no torsional stress in the cross beams but at the coupling bar.

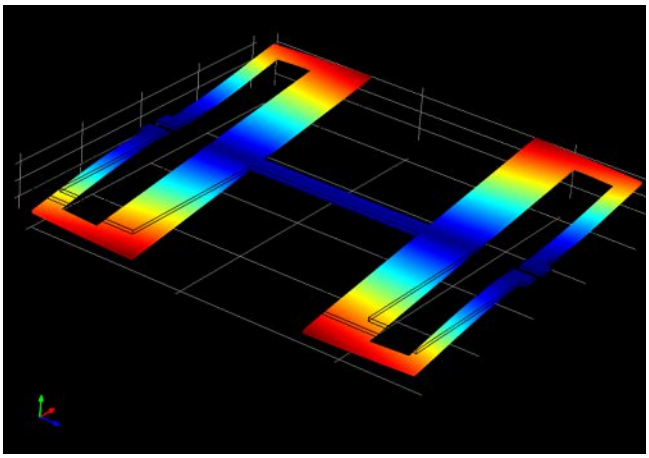

Fig. 9: First antisymmetric mode at 11.189 kHz, with current in antiparallel direction, field configuration as shown in Fig4.

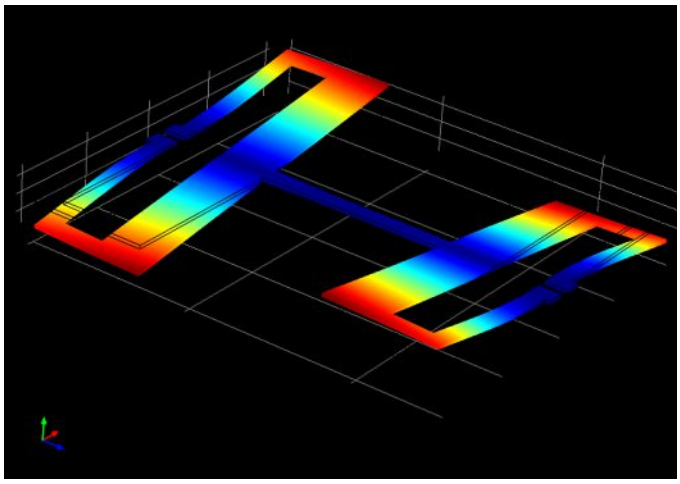

Fig. 10: Second antisymmetric mode at 12.999 kHz, with current in parallel direction.

Fig. 7 to Fig. 13 depict the simulated symmetric and antisymmetric modes for the discussed structures. The scales in the *x*- and *z*- direction are in mm. The deflections in the *y*- orientation are in nm (stimulated with U_{ss} = 2 V and B_0 = 350 mT).

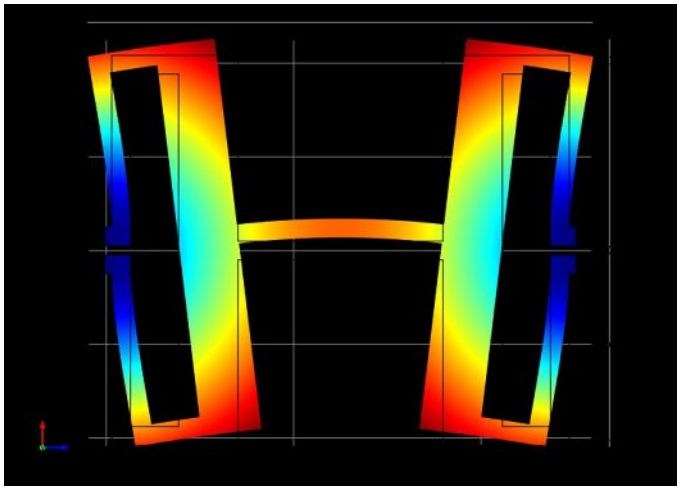

Fig. 11: Inplane mode at 45.683 kHz, with current in parallel direction.

Fig 11 depicts the first simulated inplane mode for the Omega structure. This theoretical deformation is very small and due to additional flux density components in *x*- or *z*-direction combine with out-of-plane modes.

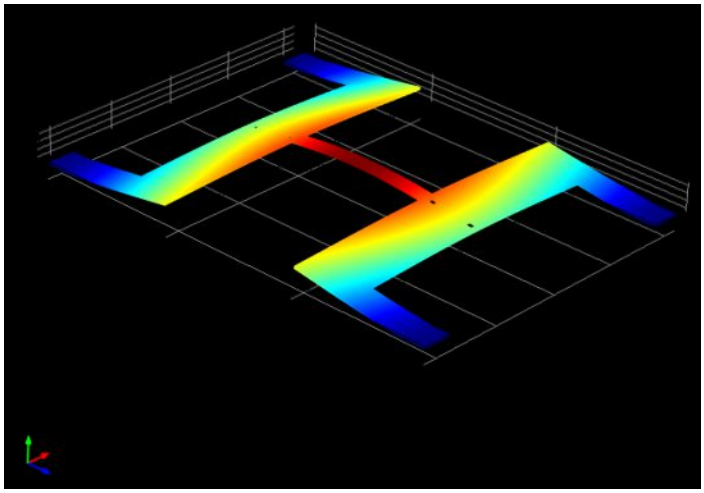

Fig. 12: First symmetric mode of the H-shaped structure at 10.23 kHz, with current in parallel direction.

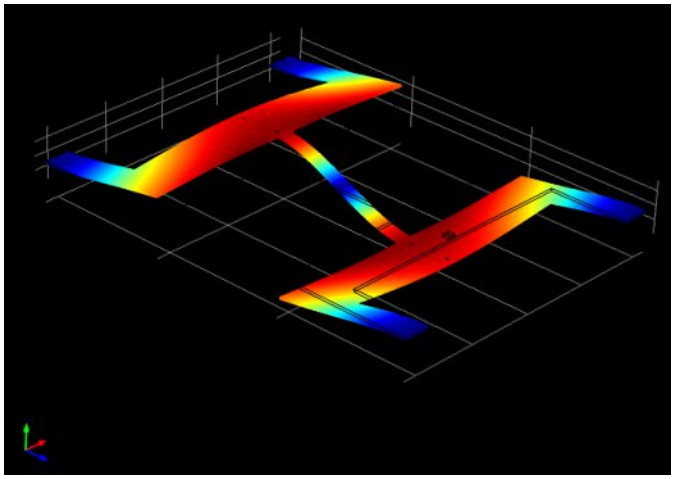

Fig. 13: Second symmetric mode of the H-shaped structure at 22.13 kHz, with current in parallel direction.

The inplane mode can be applied to measure the third field component in *y*-direction. An

antiparallel current is necessary to stimulate this mode (Fig. 6).

In comparison to other modes the stiffness is much higher which causes a lower sensitivity due for the flux density. In our case the minimal detectable field intensity is one order of magnitude higher than for the other modes. The specific range between the resonant frequencies allows to measure three field components at the same time. However, an inplane-displacement causes a shift of the resonant frequencies of the out-of-plane modes, because the inplane-displacement causes internal stresses.

The simulation delivers information about the stress in the coupling bar. Its value is important to match the resonance frequency of the two substructures. A further aspect is, that the coupling bar should not have a too small mass to limit the effect of the different resonance frequencies of both substructures.

TABLE. III: Resonant frequencies of the two structures and the rel. error between the simulated and the measured resonant frequencies in relation to the simulation.

	measured f_{res}[kHz]	simulated f_{res}[kHz]	error [%]
Ω structure	8.13	8.16	0.37
	13.32	13.43	0.82
	29.65	29.89	0.80
	37.28	36.13	3.18
H-shaped	10.35	10.23	1.17
	21.97	22.13	0.72

Table III summarizes the differences between measured and simulated eigenfrequency of the sensing structure.

The etching processes, especially the wet chemical etching, cause some under etching where the “legs” are clamped. These technological tolerances lead to small variations of the length at the legs [10]. An adjustment of the length of the supporting legs from the simulation model at the first symmetric mode, to match the resonant frequencies causes a smaller relative error at the other modes. A section of 150 nm was removed on both supporting arms. Without this adjustment, the error between simulation and measurement of the first symmetric mode of the Omega shaped structure increases to 4.18%. This reveals that the simulated model of the structure is well suited to predict the resonant frequencies

4.4.6 Measurement

The magnetic field is generated by two permanent magnets and the sensor is placed in between. One of these magnets can be moved by a micrometer screw. With this system, a magnetic gradient field can be generated. If the distance between the magnets and the sensor is equal on both sides, the field is homogenous. The characterization of the flux density is done with a Hall-sensor (Projekt Elektronik GmbH Berlin Teslameter FM 302) that can be arranged directly under each substructure.

The leads on the substructures are connected in series, whereas current can flow in parallel or antiparallel direction to excite the first symmetric or first antisymmetric mode, respectively.

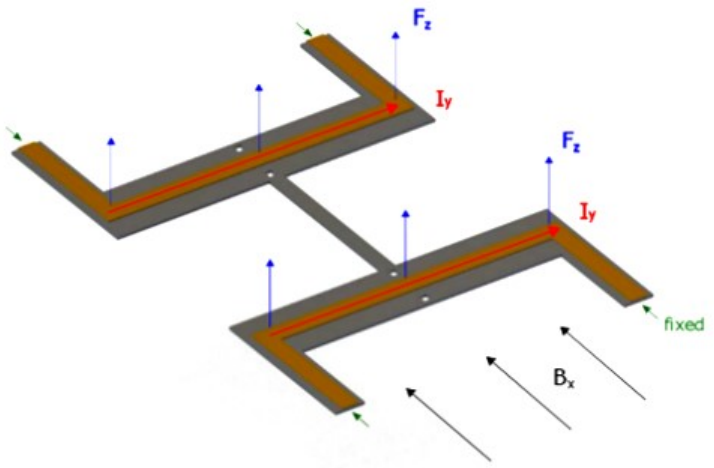

Fig. 14: H-shaped structure: parallel current mode, with the flux density in this direction, it is used for the unequal symmetric modes.

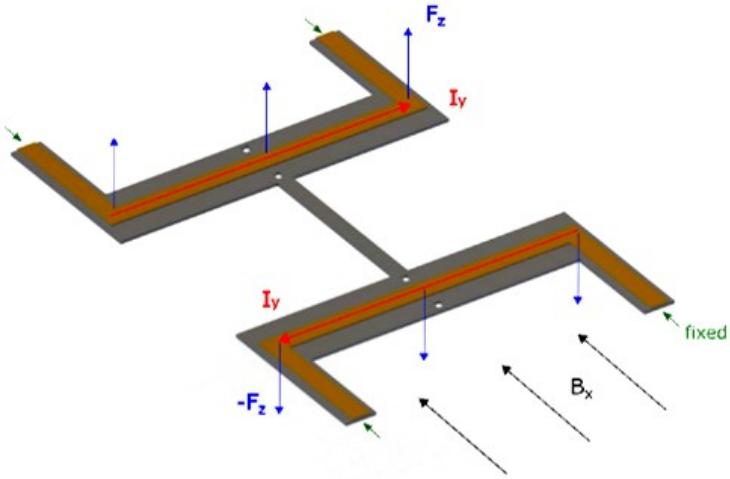

Fig. 15: H-shaped structure: antiparallel current mode, with the flux density in this direction, it is used for the equal symmetric modes.

If the current direction is parallel, symmetric modes (fig. 14) are excited. Every force on the cantilever is perpendicular to the flux density and the current direction as shown in Fig. 14. For a gradient field and symmetric excitation one of the cantilever exhibits a smaller deflection than the other one. This movement can be divided into a symmetric and an antisymmetric component (fig. 15). In the first symmetric mode of the cantilever the symmetric part is much higher than the antisymmetric. For the second symmetric mode, the current is antiparallel.

To find the resonance frequencies (fig. 16 and 17), a periodic chirp from 3 kHz to 60 kHz with 1000 measuring points over the complete range and additional 1000 measuring points in the vicinity of the simulated resonance frequencies is applied.

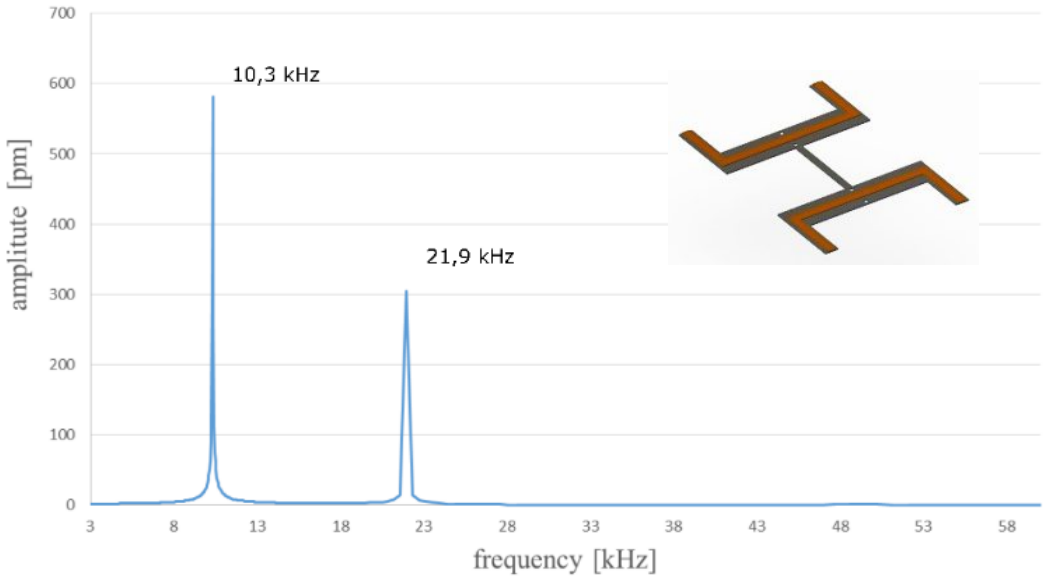

Fig. 16: Resonance spectrum of the H-shaped structure only for symmetric excitation

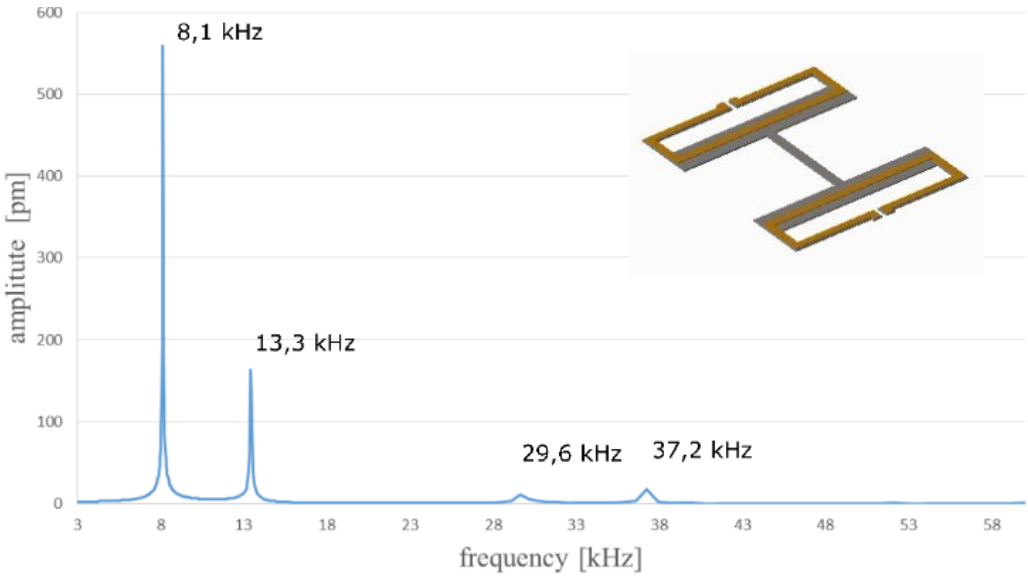

Fig. 17: Resonance spectrum of the Ω structure only for the symmetric excitation

Afterwards the structure is excited with a sinusoidal current and the resulting deflections are recorded with a Micro System Analyzer (MSA 400 from Polytec) (see fig. 18).

With the measurement of the frequency spectrum also the corresponding quality factor was determined (see table IV).

TABLE. IV: Quality factors of the respective modes of the structures in ambient conditions.

structure	mode	f_{res}[kHz]	quality factor [1]
Ω structure	S1	8.13	380
	S2	13.32	538
	S3	29.65	932
H-shaped	S1	10.35	375
	S2	21.97	291

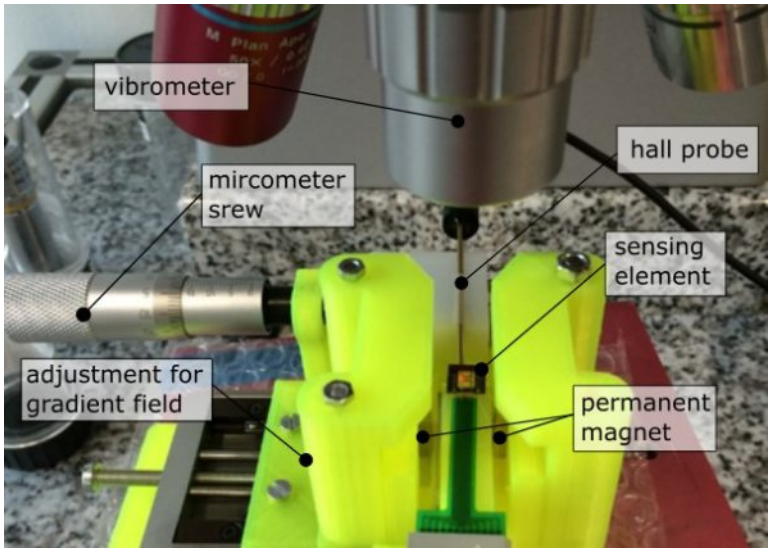

Fig.18: Measurement setup with the dipole and the H-shaped sensor.

4.4.7 Gradient measurement

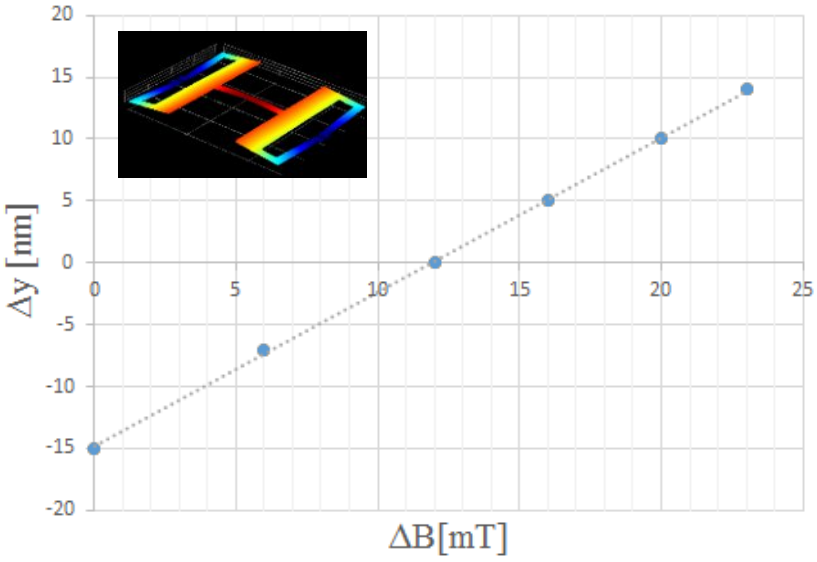

Fig 19: Measurement of the magnetic flux density gradient field with B0 =218 mT; excitation current 4 mA (R = 47 Ω),

deflections of 526 nm at the 1st symmetric mode (8.1 kHz). ΔB represents the difference of the flux density between the two sub structures. And Δy is the deflection difference between these two. With a SNR of 25,2 dB.

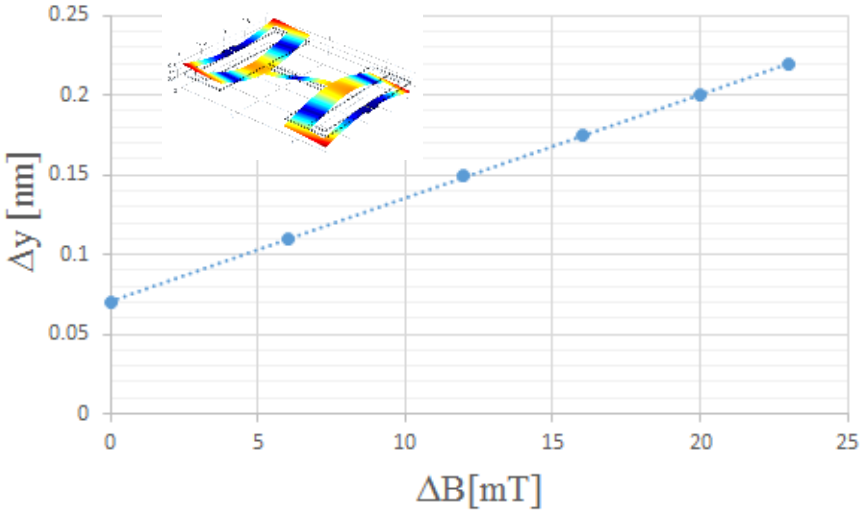

Fig 20: Measurement of a magnetic flux density gradient with B0 = 218 mT; excitation current 4 mA (R = 47 Ω), deflections of 5.6nm at the 4th symmetric mode (37.3 kHz). With a SNR of 24,9 dB.

Magnetic flux densities between 150 mT and 300 mT cause deflections of the cantilever of 300 nm to 550 nm (Fig. 19 and 20). To keep the cantilever's vibration in a linear regime, it is common to adjust the currents like done in reference [1] to measure flux densities over 1T. The flux densities in the µT regime can be measured with a ten times higher current (40 to 50 mA) on the structure, causing the same deflection. Without using antiparallel current modes, it is possible to detect gradients up to 25 mT per mm at the first symmetric mode.

4.5 Conclusion and Outlook

MEMS based magnetic field gradient sensors are able to measure minute differences in magnetic flux density per unit length. The presented design permits the measurement of the flux density in two directions and the gradient in one direction. This was achieved by two facing substructures coupled with a bar to ajust the resonance frequencies.

Higher accuracy will be achieved by using a vacuum chamber to eliminate air damping. Additional the measurement and control of the surface temperature to reduce the drift of the resonance frequency with the ambient temperature will further increase the accuracy of the results.

4.6 References

[1] M. Stifter; “MEMS µ-wire magnetic field detection method@CERN.”; IEEE Sensors Journal, 15717295, 2015 vol2; ISBN: 978-1-4799-8203-5

[2] V. Kumar; “Amplitude modulated Lorentz force MEMS magnetometer with picotesla sensitivity”; Journal of Micromechanics and Microengineering; v26 no10, 2016,

[3] M. Stifter, “Lorentz Force Actuated Resonant MEMS Magnetometer with Capacitive Read-out”, Vienna University of technologie 2012; dissertation, TU Vienna university library

[4] T.Perrier; “Optimization of a MEMS Magnetic Thin Film Vibrating Magnetometer”; vPP, i99, 2016 Volume 53 Issue 4

[5] A. Duwel, “Engineering MEMS Resonators With Low Thermoelastic Damping”; Journal of Microelectromechanical Systems, v15 i6, Dec. 2006

[6] J. Acevedo-Mijangos, C. Soler-Balcázar, H. Vazquez-Leal, J. Martínez-Castillo, A.L. Herrera-May, “Design and modeling of a novel microsensor to detect magnetic fields in two orthogonal directions” H. et. Al. Microsyst Technol (2013) 19:1897. doi:10.1007/s00542-013-1795-y

[7] I.A. Blech, „Electromigration in thin aluminium films on titanium nitride”; Journal of Applied Physics 47, 1203; 1976; 10.1063

[8] B. Stahlmecke, “Elektromigration in Gold und silber Nanostrukturen“, 2008; Page 34 (4)

[9] M.A. Hopcroft, W.D. Nix and T.W. Kenny, ”What is the Young´s Modulus of Silicon”, MEMS IEEE, vol. 19, no. 2, pp. 229-238, April 2010.

[10] C. Riesch, “Micromachined Viscosity Sensors” , ISBN 978-3-8322-8543-2; 2009

[11] F. Keplinger, “Contributions to Miniaturized Sensors”, Vienna University of technologie 2005, habilitation, TU Vienna university library

V. Publication Three

Temperature dependency of silicon structures for magnetic field gradient sensing

Authored by A. Dabsch, C. Rosenberg, M. Stifter and F. Keplinger
Published in: Journal of Journal of Micromechanics and Microengineering

Abstract

This work describes the temperature dependence of two sensors for magnetic field gradients sensors and demonstrates a structure to compensate the drift of the resonance frequency over a wide temperature range. The temperature effect of the sensing element is based on internal stresses induced by the thermal expansion of the material wherefore FEM is used to determine the change of the eigenvalues of the sensing structure. The experimental setup utilizes a Helmholtz coil system to generate the magnetic field and to excite the MEMS-structure with Lorentz forces. The MEMS structure is placed on a plate heated with resistors and cooled by a Peltier element to control the plate temperature. In the second part, we describe how one can exploit the temperature sensitivity for temperature measurements and show the opportunity to include the temperature effect to increase the sensitivity of single-crystal silicon made flux density gradient sensors.

5.1 Introduction

Typical magnetic field gradient sensors based on MEMS technology [1] exhibit a temperature dependence of the resonant frequency that is mainly caused by thermal expansion of the cantilever arms [2]. First, the sensors are built out of SOI wafers with a buried $Si0_2$-layer under the Si sensing structure. The thermal coefficient of expansion of these materials is four times lower than that of Si [3]. Second, vibrating structure and carrier frame have different masses and therefore different heat capacities, leading to different temperatures in transient processes.

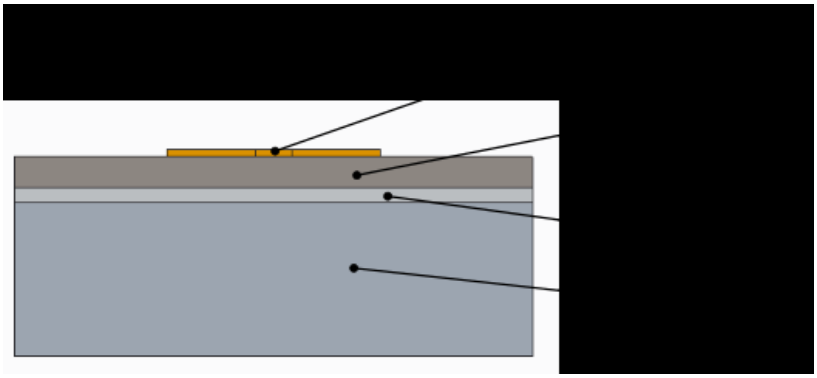

Fig. 1: Structure of the MEMS Sensor

Due to these differences, temperature variations will expand or tighten the measuring structure faster than the carrier frame. A mechanical stress is the consequence which alters the resonance frequency. The desired high quality factor of the structure causes a high error level in the amplitude due to the temperature dependence [4]. In this work, a specific mechanical substructure is designed, fabricated and proposed to compensate this temperature dependence (Fig. 1).

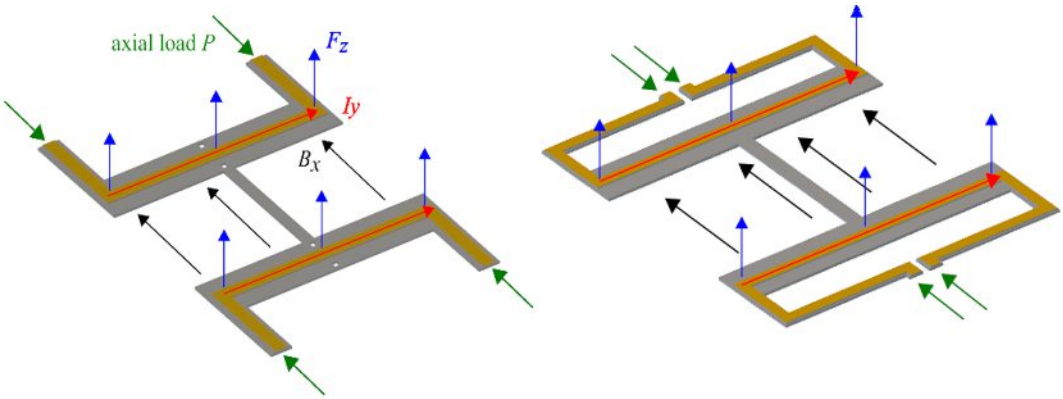

Fig. 2: Layout of two structures with relevant Lorentz-forces (Fz) for the first symmetric modes with parallel current (Iy) direction (left the double U shaped structure, right the Omega shaped structure). Bx is the magnetic flux density and P is the axial load by thermal expansion.

The sensors used within this paper are discussed in an earlier paper of our group regarding to the sensitivity of the magnetic flux density gradient (see Table IV). [5].

5.2 Theory

5.2.1 Extended Euler Bernoulli beam theory – Timoshenko beam theory

For the calculation of the temperature coefficient regarding the resonance frequency, the Euler Bernoulli beam theory must be extended with the bending and normal stresses.

Only the first symmetric mode is investigated in our experiments. Hence, Timoshenko theory can be simplified and applied to an oscillating solid-shell element for the H-shaped structure. The resonant frequency reads:

$$f = \frac{1}{2\hat{L}}\frac{1}{\sqrt{\rho v}}\sqrt{P}, \tag{1}$$

where $\hat{L}$ is the length of the oscillating structure, ρ is the mass density, v is the Possion´s ratio, and P is the force in longitudinal direction (prestress) [6].

For a long thin structure with small oscillating amplitude, a $\sqrt{P}$ dependence is expected. The resultant force is generated by the geometry of the structure due to thermal expansion. In addition, with the effect of the prestress on the eigenvalues, the Timoshenko beam theory [7] is described by:

$$\frac{\partial^4 u_y}{\partial x^4} - \frac{P}{E\,I_z}\frac{\partial^2 u_y}{\partial x^2} + \frac{\rho A}{E I_z}\frac{\partial^2 u_y}{\partial t^2} = 0\,. \tag{2}$$

Due to the huge difference of the heat capacities of the free standing structure and the carrier frame, the MEMS structure responds faster to temperature changes than the carrier frame. The occurring outer stresses can be approximately described as a function of the temperature difference of the measuring structure to the frame by:

$$\varepsilon_{\text{ges}} = \varepsilon_{\text{th}} + \varepsilon_{\text{m}}\,,\ \varepsilon_{\text{th}} = \alpha \cdot \Delta T\,,\ \varepsilon_{\text{m}} = \frac{\sigma}{E(T)}\,, \tag{3}$$

where ε_{ges} is the total strain, ε_{th} is the thermal strain, ε_{m} is the mechanical strain by stress, α is the thermal coefficient of expansion (*TCE*), σ is the tensile/compressive stress, E is the Young's modulus [8].

For a small temperature range from 300K to 350K the nonlinearity of the *TCE* of silicon, is negligible. The occurring stress is

$$\sigma = -E(T) \cdot \alpha \cdot \Delta T \tag{4}$$

The temperature coefficient from the Young's modulus of silicon for axial load is -60ppm/K and for uniaxial load -75ppm/K. The bending stiffness decreases with temperature [9].

For the theoretical consideration, we use the design of a torsional oscillator (Fig. 2).

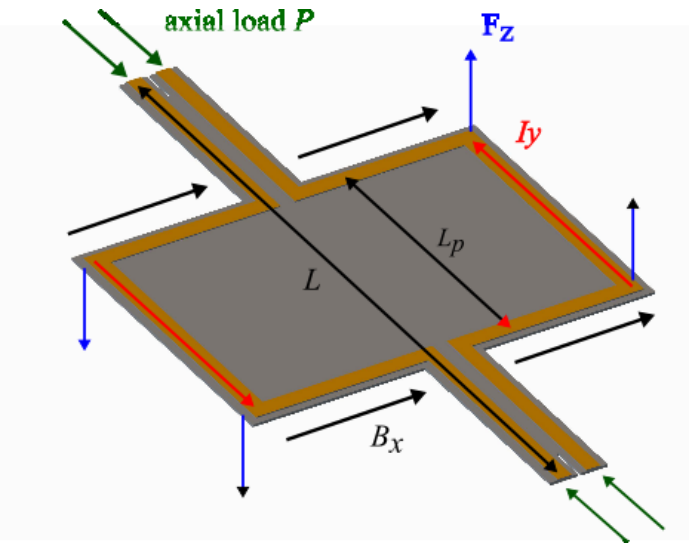

Fig.3: Design of the torsional oscillator with the forces (Fz) for the first torsional mode, with antiparallel currents (Iy), the whole length of the structure, plate and bars (L) and the length of the plate (Lp).

Applying only antiparallel currents, we excite a pure torsional oscillation without any bending components (in the *y*-direction) due to the symmetric design. The oscillation mode with axial load P is described by:

$$\left[GJ - \frac{PI_\alpha}{m}\right]\frac{\partial^2\varphi}{\partial x^2} - I\frac{\partial^2\varphi}{\partial t^2} = 0\,, \tag{4}$$

where G represents the shear modulus and J is the moment of inertia (in a good approximation the moment of inertia of the bar), I is the polar mass moment of inertia per unit length, m represents the mass of the oscillator, and φ is the angular displacement of the bar [8].

Applying (4) into design considerations, attention should be paid to some design details and boundary conditions: The plate in the middle of the oscillating system is short compared to the whole bar ($L_p < \hat{L}$) and the torsional stiffness of the plate is much higher. The majority of the total torsion occurs in the bars.

The neutral axis and the center of mass axis are congruent and are not subjected to any bending deformation.

The static deflection of the bar caused by the gravitational force on the mass of the plate is neglected. The deflections act in the linear elastic regime and boundary effects in the connection between plate and bar are neglected.

Solving the eigenvalue problem delivers the eigenfrequency of the torsional mode (only the first antisymmetric mode with antiparallel current, depicted in Fig. 3 is calculated)

$$\omega_P = \frac{\pi}{\sqrt{\hat{L}}}\sqrt{\left(\frac{GJ}{I} - \frac{P}{m}\right)}. \tag{5}$$

By setting P to zero the equation yields the eigenfrequency $\omega_0 = 4446$ Hz without any boundary load through thermal influences. The result of the simplified calculation is in good agreement with the experimental data (see chapter IV). The parameters used for the calculations are listed in Tab. 1.

TABLE I: Relevant parameters for the simulation of the silicon structure [8]

Symbol	Quantity	Value
G	Shear modulus	64.1 GPa
ν	Poisson ratio	0.28/0.2
$\hat{L}$	Free length	4 mm
J	Sec. moment of inertia	$2.66 \cdot 10^{-19}$ m^4
I	Moment of inertia per unit length	5.32 $\cdot 10^{-10}$ kgm^2
α	TCE	-60 ppm/K for axial load

5.2.2 Influence of the temperature effect of the lead on the operating temperature

Due to strong frequency changes caused by small temperature variations, the heating power of the lead has to be taken into account. Therefore, the heat balance of the lead on the Si wafer under atmospheric influence is given by:

$$K(T) = P(T) \tag{6}$$

where $K(T)$ is the heat dissipation and $P(T)$ is the produced heat by the electrical current [10]. The heat dissipation to the surroundings, it can be split into the three parts: heat conduction ($\dot{Q}_{\mathrm{cond}}$), convection ($\dot{Q}_{\mathrm{conv}}$) and thermal radiation ($\dot{Q}_{\mathrm{rad}}$).

$$K(T) = \dot{Q}_{\text{cond}}(T) + \dot{Q}_{\text{conv}}(T) + \dot{Q}_{\text{rad}}(T) \quad (7)$$

$$\dot{Q}_{\text{cond}}(T) = \lambda \frac{T_2 - T_1}{h} A_s$$

$$\dot{Q}_{\text{conv}}(T) = \alpha(\text{T})\, A_s\, (T_2 - T_e) \quad (8)$$

$$\dot{Q}_{\text{rad}}(T) = \varepsilon\, \sigma\, A_s\, (T_2^4 - T_e^4), \quad (9)$$

where T_2 is the temperature of the lead, T_1 is the temperature of the Si wafer, h is the thickness of the lead path, A_s is the contact surface of the lead with Si structure, and T_e is the ambient temperature.

To calibrate the sensor, the temperature of the sensor frame (silicon wafer) has to be known. The energy balance is:

$$P(T) = \hat{U}_{\text{eff}}\, I \quad (10)$$

$$\hat{U}_{\text{eff}}\, I = \lambda \frac{T_2 - T_1}{h} A_s + \alpha(\text{T})\, A_s\, (T_2 - T_e) + \varepsilon\, \sigma\, A_s\, (T_2^4 - T_e^4) \quad (11)$$

$$\xrightarrow{\text{convert}} T_1 = \frac{h}{\lambda}\left[\alpha(\text{T})\, (T_2 - T_e) + \varepsilon\, \sigma\, (T_2^4 - T_e^4) + \frac{\hat{U}_{\text{eff}}\, I}{A_s}\right] = 31.209\ °\text{C} \quad (12)$$

To calculate T_2 the resistance of the lead with stable power supply was recorded:

$$R_1 = \frac{L_{\text{LB}}}{A_q} \rho_{20} (1 + \alpha_R \Delta T_1) \quad \text{and} \quad (13)$$

$$R_2 = \frac{L_{\text{LB}}}{A_q} \rho_{20} (1 + \alpha_R \Delta T_2)\,, \quad (14)$$

where R_1 is the electrical resistance of the lead at room temperature, R_2 is the electrical resistance of the lead after 15 minutes of the temperature change, L_{LB} is the length of the lead, and A_q is the cross section of the lead. With the measurement results T_2 becomes:

$$T_2 = \Delta T_2 - T_R = 31.211\ °\text{C} \quad (15)$$

The dominating term is $\dot{Q}_{\text{cond}}$ which is 70 times larger than $\dot{Q}_{\text{conv}}$ and 1600 times larger than $\dot{Q}_{\text{rad}}$. $\dot{Q}_{\text{cond}}(T) = 2.33$ mW, $\dot{Q}_{\text{conv}}(T) = 0.033$ mW, $\dot{Q}_{\text{rad}}(T) = 0.0014$ mW.
Therefore, for measurements at room temperature and considering the actual geometry the, $\dot{Q}_{\text{conv}}(T)$ and $\dot{Q}_{\text{rad}}(T)$ can be neglected.(For calculation see Table II)

5.2.3 Material specifications

The applied material is [100] silicon featuring an anisotropic Young's modulus of 170 GPa in ⟨111⟩ directions and reduced values down to 130 GPa for all other directions [9].

Via the lithography process, thin gold leads with a thickness of 150 nm are deposited on the silicon structure. These leads are insignificant for the thermal tensile or compressive stress due to the Young's modulus of 78 GPa is 2.2 times higher than that of silicon and the lead is 100 times thinner than the silicon structure.

During Au evaporation mechanical stress is introduced in the metal layer and consequently within the Si-structure. Afterwards, this pre-stress is be minimised by a thermal treatment at 90°C for one hour.

Between the sensor and the Pt100 element, (see Fig 6 and 7) a two-component conductive silver epoxy is used as intermediate layer.

TABLE II: Relevant parameters for the calculation of the heat balance.

Symbol	Quantity	Value
λ_s	Thermal conductivity coefficient	117 W/mK
$\alpha(T)$	Convection coefficient for free convection	6 W/m²K
ε_{Au}	emission coefficient	0.04
σ	Stefan-Boltzmann constant	$5.6 \cdot 10^{-8}$ W/(m²K⁴)
ρ_{20}	Specific resistance of gold at room temperature	$2.2 \cdot 10^{-2}$ Ωmm²/m
α_R	Temperature coefficient of specific resistance	$3.7 \cdot 10^{-3}$ 1/K

5.3 Simulations

As a first step, the temperature dependency is simulated with the FEM-software COMSOL® Multiphysics 5.2.

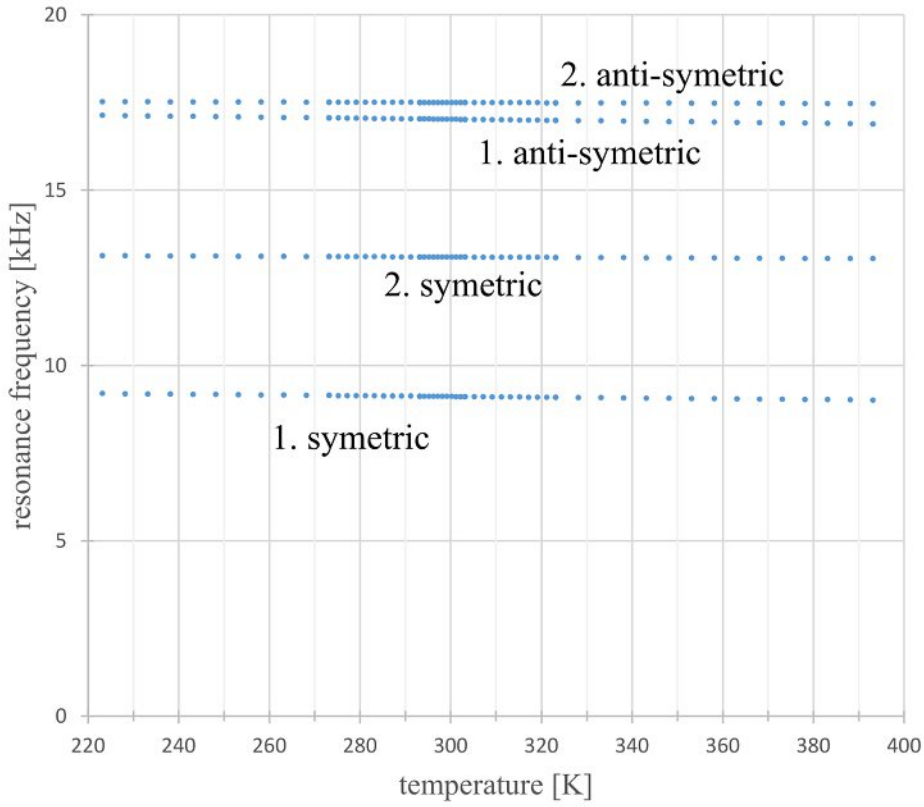

Fig. 4: Simulated temperature dependence of the resonance frequencies of the first six modes of the Omega shaped design.

Different designs are tested with FEM simulation. Figure 4 and 5 depicts the temperature dependence of the resonant frequency of the first six modes. The reference temperature was set to 300K [1].

For modelling, we assumed that there is no thermal expansion of the frame surrounding the oscillating structure. A temperature difference between frame and silicon based structure is set. For this reason, the supporting points of the structure are fixed in axial direction. Avoiding torsion of the gradient structures (plate) the suspension bars are not generally fixed in radial direction.

Comparing Fig. 4 and 5 illustrates that the Omega shaped structure has a lower adjustment of the resonant frequency. Due to the smaller stiffness in x-direction, caused by the meander sub structure (Fig.2).

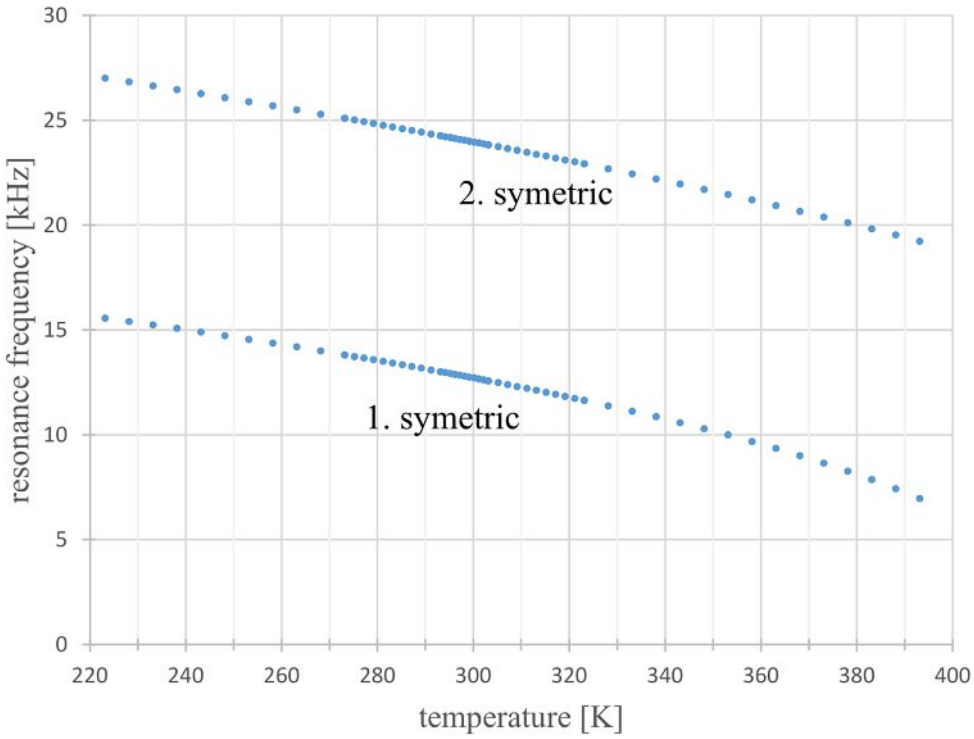

Fig. 5: Simulated temperature dependence of the resonance frequencies of the first six modes for the double U shaped design.

5.4 Measurements

The measurement setup comprises a set of Helmholtz coils where the sensor is fixed in the center on a plate that can be heated up. The leads on the structure are connected to a waveform generator that produces a periodic chirp in the range of 500 Hz around the resonant frequency of the selected sensor. (see Table III) The deflections are recorded with a Micro System Analyzer (MSA 400, Polytec).

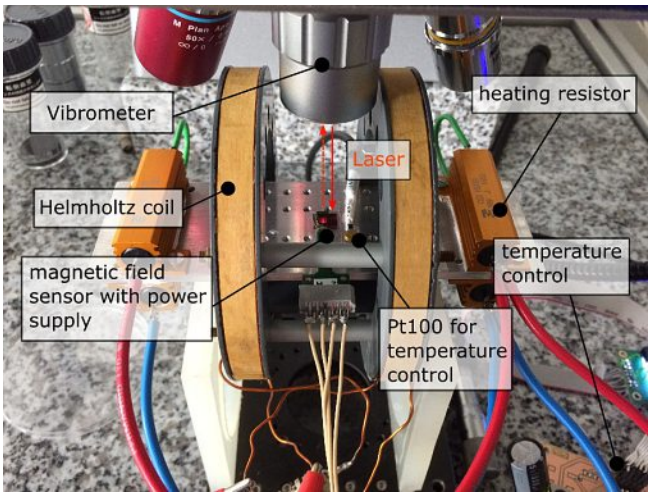

Fig. 6: Measurement setup with Helmholtz coils, heating plate and readout with the vibrometer.

The heat control plate is made from aluminum equipped with a PT100 element and four heating resistors driven by a PWM controller. To avoid any interferences with the magnetic field of the two Helmholtz coils, the heat resistors are placed outside of the coils. For good heat transfer and low distortions of the magnetic field, aluminum with its paramagnetic properties is used. In the middle of the plate, directly on the surface, the PT100 element is placed, measuring the actual temperature of the plate. The controller allows adjusting the temperature in a range from room temperature up to 100°C.

To measure the temperature of the sensor, more precisely the Si-frame, another Pt100 element is mounted directly on the Si structure (see Fig. 7 and 8). The limited heat transfer between aluminum plate and sensor will cause a slight temperature difference. The result of the sensor Pt100 element is the actual temperature for the device (reference temperature for the subsequent measurements).

TABLE III: Operating parameters

Symbol	Quantity	Value
Uss	Stimulation voltage	1 V
I_s	Parallel current mode	2.3 mA
I_H	Current Helmholtz coils	1 A
B	Magnetic field	5.4 mT

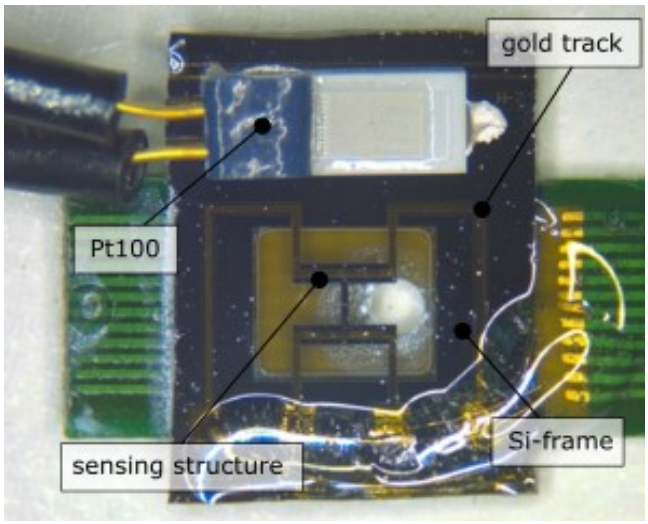

Fig. 7: Double U-shaped design with a Pt100 fixed with a silver thermal adhesive.

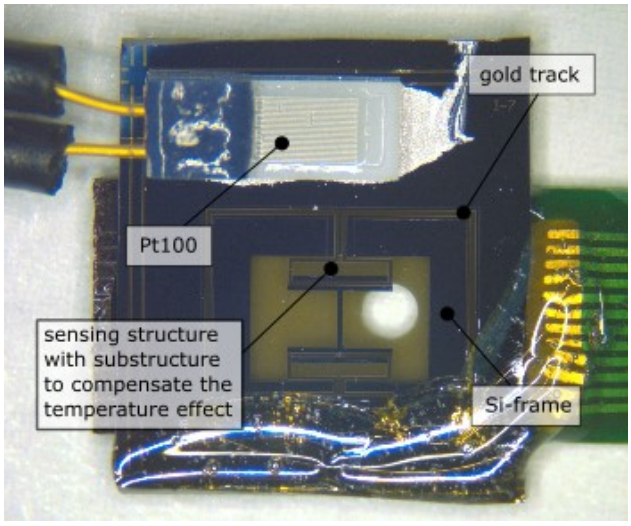

Fig. 8: Omega shaped design

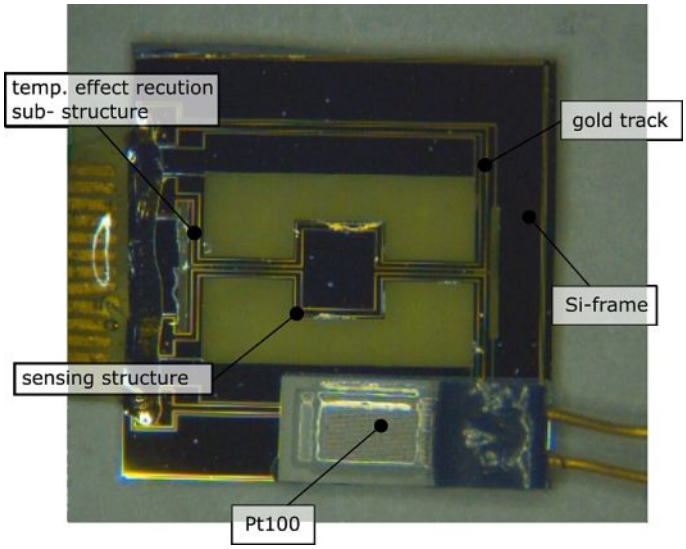

Fig. 9: Torsional oscillator design

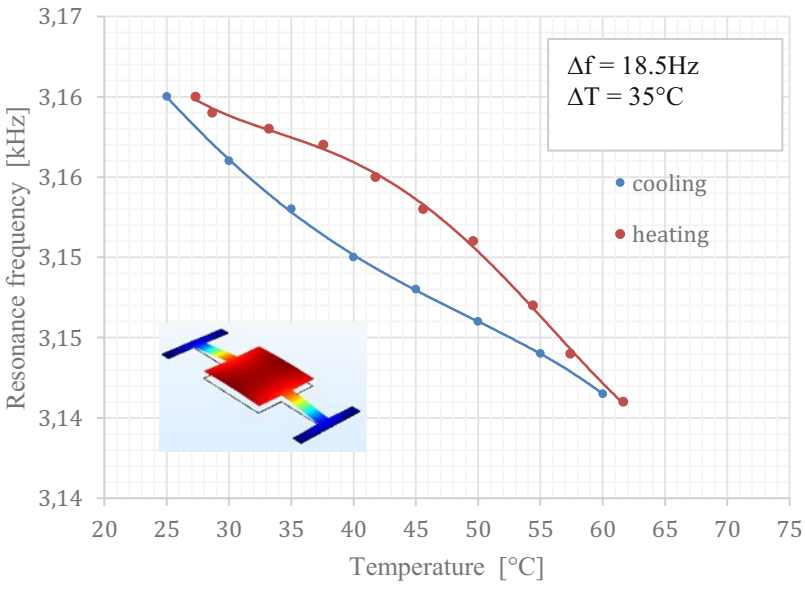

Fig. 10: Measured temperature induced change of the resonant frequency of the first symetric mode.

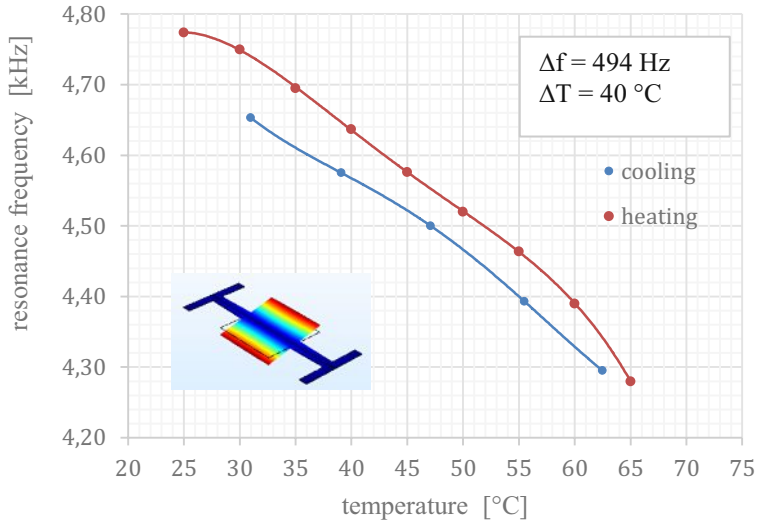

Fig. 11: Measured change of the resonant frequency of the first antisymetric (torsional) mode from the torsional bending structure in dependence of the temperature.

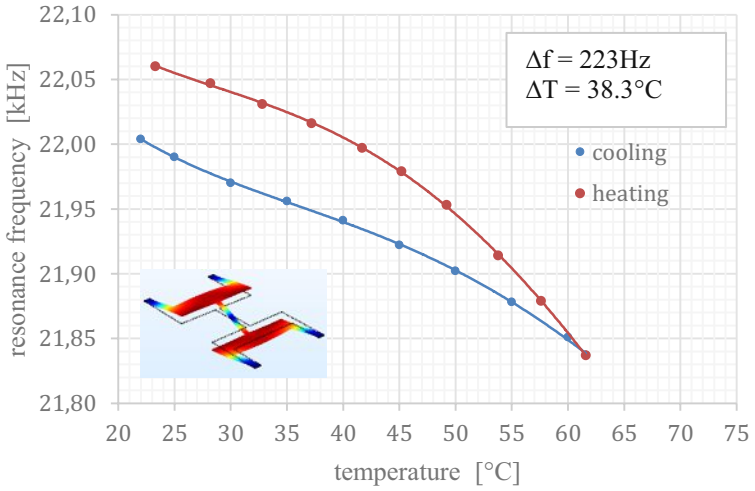

Fig. 12: : Measured change of the resonant frequency of the second symetric mode from the double U shaped structure in dependence of the temperature.

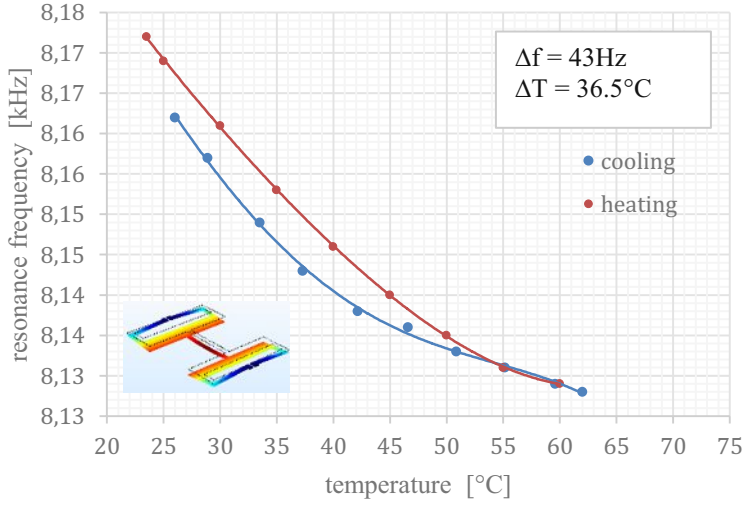

Fig. 13: Measured change of the resonant frequency of the first symetric mode from the Omega shaped structure in dependence of the temperature.

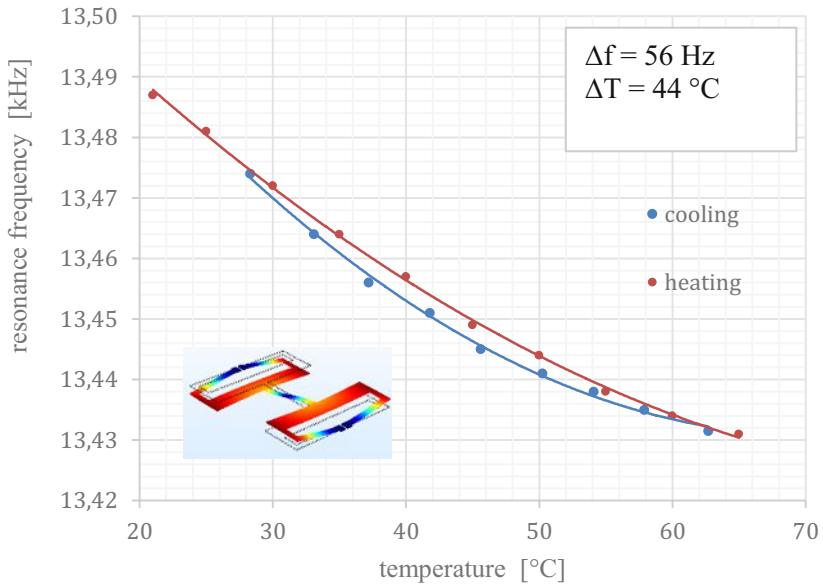

Fig. 14: Measured change of the resonant frequency of the second symetric mode from the Omega shaped structure in dependence of the temperature.

The measurements are performed with the highest possible continuous load of the Helmholtz coil. With lower flux densities, no significant change in the temperature dependency has determined.

TABLE IV: used structure types with the sensitivities for magnetic field gradient and the temperature sensitivities.

Structure	**Sensitivity [mT/mm]**	**Temp. Sensitivity [Hz/K]**
U shaped (second sym. mode)	0.09	5.8
Omega shaped (second sym. mode)	0.1	1.3
Torsional structure (first anti-sym. mode)	*	12.4
Torsional structure (first sym. mode)	0.24	0.53

*it's not possible to measure a field gradient with the torsional bending structure at the anti-symmetric modes.

5.5 Conclusion and Outlook

The drift of the resonance frequency during heating and cooling is measured versus the temperature (recorded with a second Pt100 element directly on the surface of the Si structure) for three different sensor designs. Except of the torsional mode from the torsional bending structure (Fig. 10) the depicted results are in good agreement with the simulations (Fig. 4 and 5) and show a hysteresis between heating and cooling. This effect is caused, first by the positioning of the heat plate under the sensor and the single-sided heat supply during the heating process. Second, during the cooling process, heat dissipation only occurs on the upper surface of the sensor where the Pt100 element is fixed. Third by the high self-cooling rate (approximately 1°C per second) without heat supply. To avoid influences from the excitation current, it is switched off during the heating and cooling process.

The measurements reveal the differences between the U shaped design and the Omega shaped design (Fig. 12, 13 and 14) with the temperature effect –compensating substructures (see Table IV). Using two sensors with the same sensitivity for the magnetic flux density gradient, the temperature effect decreases from 5.8 Hz/K (U shaped) to 1.3 Hz/K (Omega shaped). In particular, this effect occurs in the case of symmetric modes due to buckling. However, no significant differences between both structure types are seen for antisymmetric modes.

The torsional bending structure has a temperature effect of 0.5 Hz/K (see Fig.11) using the first symetric mode (comparable with a both side fixed beam) caused by the additional mass in the center of the beam and the temperature-effect-compensation sub-structure (see Fig.9), but 12.4 Hz/K using the first torsional mode (which is used for the magnetic flux density gradient measurement).

Subsequently to this basic characterization, the research team aim at another set of different sensors with capacitive readout as magnetic field gradient sensor on the one hand and as high sensitive temperature sensor on the other hand. The structure is very sensitive to changes of the force on the supporting points. The team will use this effect to fabricate a multi axial force sensor with high sensitivity.

5.6 References

[12] M. Stifter, “Lorentz Force Actuated Resonant MEMS Magnetometer with Capacitive Read-out”, Vienna University of Technology 2012

[13] R. Sandberg, “Temperature and pressure dependence of resonance in multi-layer microcantilevers”, Journal of Micromechanics and Microengineering, vol 15 pp 1454-1458, June 2005

[14] A.K. Sinha, „Thermal stresses and cracking resistance of dielectric films (SiN, Si3N4 and SiO2) on Si substrates“, journal of Applied Physics, vol 49, 2423 (1978)

[15] J. Acevedo-Mijangos, C. Soler-Balcázar, H. Vazquez-Leal, J. Martínez-Castillo, A.L. Herrera-May, “Design and modeling of a novel microsensor to detect magnetic fields in two orthogonal directions” H. et. Al. Microsyst Technol (2013) 19:1897. doi:10.1007/s00542-013-1795-y

[16] A. Dabsch, “MEMS cantilever based magnetic field gradient sensor”, Journal of micromechanics and microengineering, vol 27 no 5, april 2017.

[17] Christof Rohrbach, “Handbuch für experimentelle Spannungsanalyse” p.590 D 6.13-3

[18] J.Yang, „Ninlinear free vibration of single-walled carbin nanotubes using nonlocal Timoshenko beam theory“, Elsevier, January 2010

[19] J.R. Banerjee, „Coupled bending-Torsional dynamic stiffness matrix of an axially loaded Timoshenko beam element“, int. Journal of Solids Structures Vol 31, No6, pp 749-762, 1994

[20] M.A. Hopcroft, W.D. Nix and T.W. Kenny, ”What is the Young´s Modulus of Silicon”, MEMS IEEE, vol. 19, no. 2, pp. 229-238, April 2010.

[21] H.D. Baehr, K. Stephan, „Wärme- und Stoffübergang“, 4. Auflage Springer Verlag Berlin 2004 Kap.5

VI. Publication Four

Multiaxial Resonant MEMS Force Sensor

Authored by A. Dabsch, C. Rosenberg, P. Klug, M. Stifter and F. Keplinger
Published in: Journal of Journal of Micromechanics and Microengineering

Abstract

Miniaturized force sensors are indispensable components in various applications such as atomic force microscopes. In most cases the sensor is sensitive only to a single component at the force vector. For a complete characterisation of the actual load state all three components are required and this in combination with the three torque components (six-axis force / torque sensor). We report on a sensor to measure two components of the force vector and three components of the torques simultaneously using a resonant vibrating cross-shaped bar. The sensor is manufactured on an SOI Wafer with standard Si-technology. The sensing structures are excited by Lorentz forces and detuned by the mechanical stress due to the applied force and torque. Currently, the shifts of the resonant frequencies are measured with a scanning laser vibrometer. To be able to compensate the influence of temperature additional Pt-termistors on the surface of the structure measure the actual temperature. Furthermore, the sensing structure is suspended to the sensor frame with compliant structures to reduce the temperature interferences. To investigate the effect of these substructures three different types are compared. With the multiaxial MEMS Force sensor we achieved a sensitivity of almost 10 pN/Hz.

6.1 Introduction

In most cases indirect force sensors are based on strain gauges and exhibit a decreasing accuracy with smaller deflections of the measurement object [1]. Furthermore a single torsional load, especially at thin components, generates normally no exploitable signal. The presented sensor exhibits a 20 µm thick cross shaped vibrating structure suspended to the sensor-frame via sub-structures for temperature compensation as depicted in Figure 1 [2].

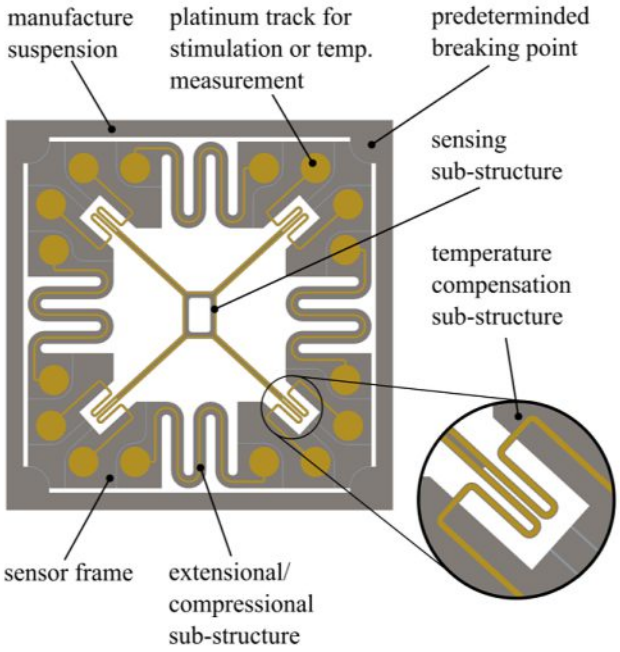

Figure 14: Design of the sensor element comprising manufacturing frame, sensor frame and sensing substructure. The insert shows the substructures for reducing the temperature influence.

Compared to sensors that are fabricated with other technologies [3][4] the presented MEMS sensor is able to sense five mechanical degrees of freedom, namely two force and three torque components by exploiting the shift of the resonant frequency of in-plane and out-of-plane vibration mode due to mechanical stress. The force components are in x and y direction and the torque moments are around the x-, y- and z- axis. F. Beyeler et. al presented a six-axis force sensor but with a capacitive readout what is less insensitive against external influences [5]. The modes are excited by Lorentz-forces applying a periodic chirp with a frequency range from 2 to 50 kHz.

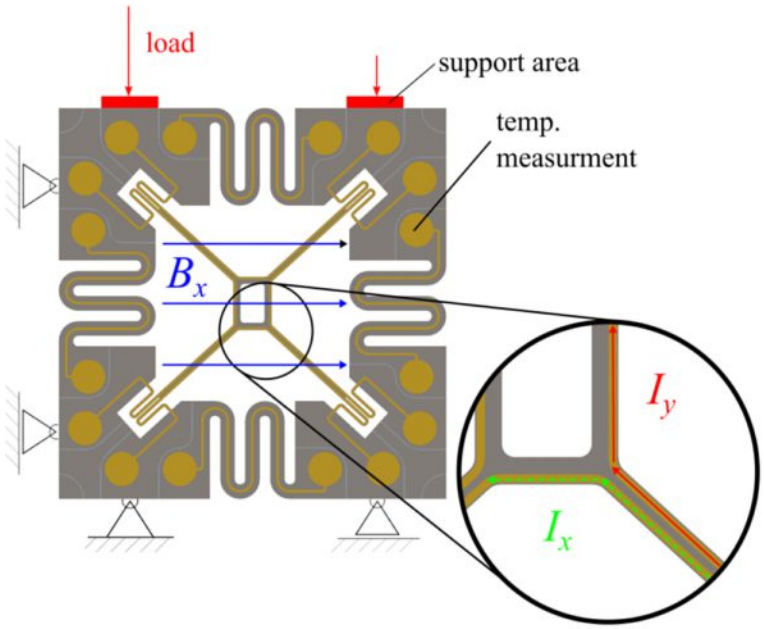

Figure 15: Sensing principle for a load in y direction and excitation with Bx, and Iy. For the reference temperature a four wire measurement is applied (Ix).

The MEMS - structure is excited by Lorentz-force caused by the currents in the leads and the magnetic field at a permanent magnet (see Figure 2) for the out-of-plane modes achieved by a permanent magnet (see Figure 11). The temperature dependence of the structure due to the different thermal expansion coefficients and due to the temperature dependent Young's and shear moduli are considered by an on-chip measurement of the temperature with a Pt-thermistor with a nominal resistance of 1 kΩ. This, in combination with a four-wire measurement, allows the compensation of the temperature dependent effects during the experiment. The asymmetrical load in Fig. 2 generates a compression of the device in *y*-direction and causes a torque around the *z*-axis. With additional vibration modes the measurement accuracy can be enhanced.

Central element of the sensor is a compliant micromechanical structure that consists of four Si parts when the load is applied. These four parts are connected by meanders (extensional/compressional sub-structure in Figure 1) their thickness and length are the main design parameter for the sensitivity of the sensor. This transducer element converts the applied Load into deflections of the Si-parts. These are deflections used by another element, the sensing substructure. Hence, the deflections change the resonant frequency of the vibration modes. Whereby the spring constant of the meander is large compared to the spring constant of the sensing sub-structure. The expected displacements are small enough allowing the springs to be considered as linear elements. Thereby it is also possible to use the sensor for micro positioning systems. Potential applications are in robotic and medicine technology,

caused thru the simultaneous multi displacement/force detection. The main focus in this study is the sensing structure and not the Readout. A. Nakai et. al presented a sensor with piezo resistive beams for the readout, which could be a role model for further development of the sensor [6].

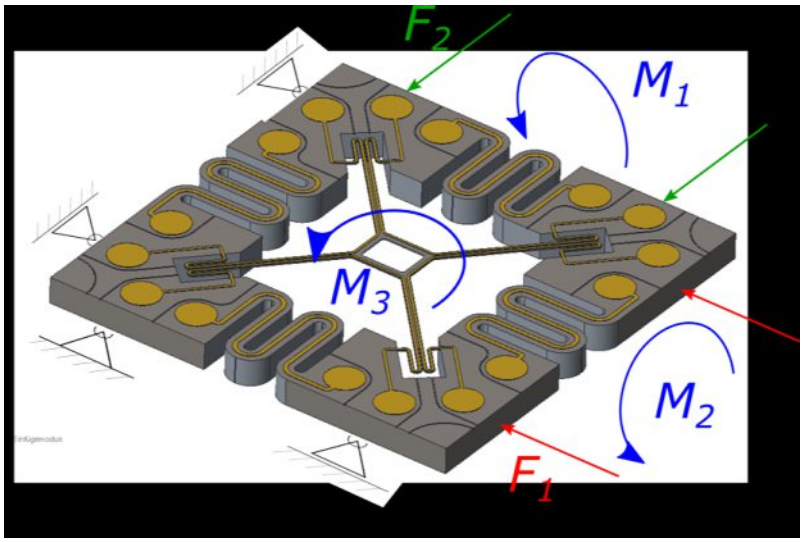

Figure 16: Five degrees of freedom, namely two force and three torgue components

The sensor is able to measure five degrees of freedom (see Figure 3). For these five degrees, five modes are necessary. In this paper only the two force components are described and presented.

6.2 Theory and Simulation

6.2.1 Timoshenko beam theory

To describe a prestressed doubly-clamped beam Timoshenko beam theory can be used [7].

$$\frac{\partial^4 u_y}{\partial x^4} - \frac{F}{E\,I_z}\frac{\partial^2 u_y}{\partial x^2} + \frac{\rho A}{E I_z}\frac{\partial^2 u_y}{\partial t^2} = 0\,. \tag{1}$$

Where u_y is the deflection, F is the pre-stress, E the Young's modulus, I_z is the moment of inertia, ρ is the density and A is the cross-section of the cantilever.

To adapt this model to any geometry a double clamped cantilever has to be extended to a cross shaped structure with an additional mass (m_a) in the middle. This mass reduces the eigenfrequency compared to the simple cantilever. Additionally, with different length L_x and L_y the resonant frequencies of the modes corresponding to the different arms will split up (see figure 3).

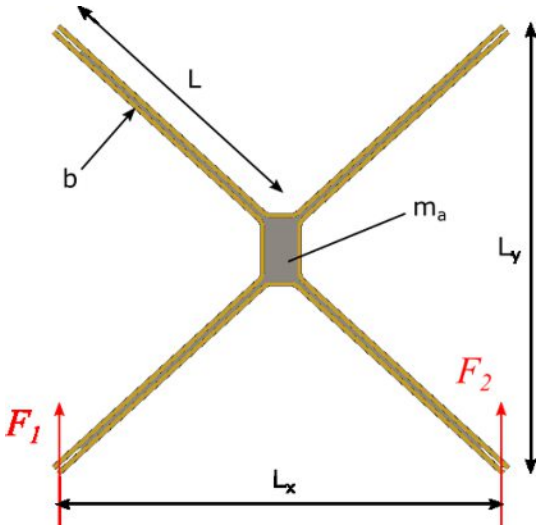

Figure 17: Sensing structure with the additional mass in the middle and the acting force F

According to the Timoshenko theory, the resonance frequency can approximately represented by [8]:

$$f_{res} \sim \sqrt{F}\ . \tag{2}$$

Where F is the pulling force or $-F$ the compressive force, acting equally on both arms of the sensing structure (see Figure 3) for symmetric loads. For an asymmetric load (a torque around z axis) we subtract the symmetric part from both forces and get a characteristic of the resonance frequency depending on two factors. First the symmetric force

$$F_{\text{sym}} = \frac{F_1+F_2}{2} \tag{3}$$

And second the torque around the z axis

$$F_{\text{asym}}\, L_x = \frac{F_1-F_2}{2} L_x \tag{4}$$

The load force is applied to the sensing structure by piezo actuators under the sensing frame. To simplify the measurement of the load we neglect the spring constant of the sensing structure and focus only on the meander structures in the frame (see Figure 1).

For the analytical model of the sensing structure we simplify the cross-shaped structure with the centered mass to a single clamped cantilever with an additional mass on the tip and a four

times higher stiffness of the cantilever and determine the boundary conditions as described below.

$$f(0) = f'(0) = f'(L) = 0 \tag{5}$$

$$f'''(L) + \kappa^4 \mu L f(L) = 0 \tag{6}$$

with

$$\kappa^4 = \omega^2 \frac{\rho A}{E I_z} \tag{7}$$

with the ratio μ of the masses of the tip and the cantilever:

$$\mu = \frac{m}{\rho A L} \tag{8}$$

To solve the eigenvalue problem we use the ansatz

$$f(x) = C_1 \sin(\kappa x) + C_2 \cos(\kappa x) + C_3 \sinh(\kappa x) + C_4 \cosh(\kappa x) \tag{9}$$

That delivers the characteristic polynom for the symmetric modes.

$$\cos(\kappa L)\sinh(\kappa L) + \cosh(\kappa L)\sin(\kappa L) + \kappa L \mu \cos(\kappa L)\cosh(\kappa L) - 1 = 0 \tag{10}$$

To solve the equation, we distinguish between three cases.

$$\mu \approx 1: \quad \kappa_1 L = 0.33; \ \kappa_2 L = 1.81 \ \ \kappa_3 L = 4.88$$
$$\mu \gg 1: \quad \kappa_1 L = 0.50; \ \kappa_2 L = 2.21 \ \ \kappa_3 L = 5.50$$
$$\mu \longrightarrow \infty: \quad \kappa_1 L = 1.57; \ \kappa_2 L = 4.71 \ \ \kappa_3 L = 7.85$$

Without additional mass $\mu = 0$ the model is identical with the double clamped cantilever.

6.2.2 Simulation

To verify the desired effect of the substructures for temperature compensation we tested three different types of suspension bars for the sensing structure (Fig. 4).

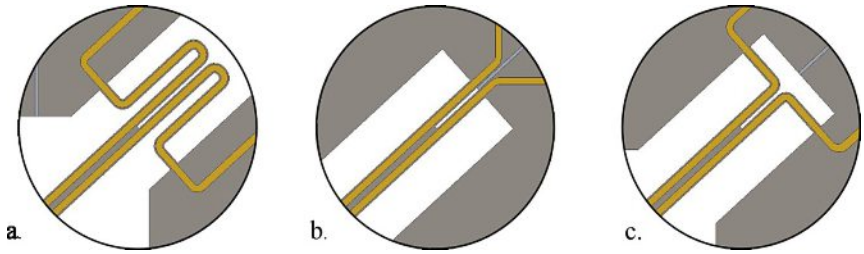

Figure 18: Different types of suspension structures

The Joule heating on the silicon structures with their small cross-section causes an overtemperature at the structure compared to the Si-frame. This causes mechanical stress and detunes the resonant frequencies of the sensing structure. The simulations confirm the expected dependence of the frequency on the temperature. Figure 5 and 6 depict the first symmetric mode of the sensing structure with the three different suspension.

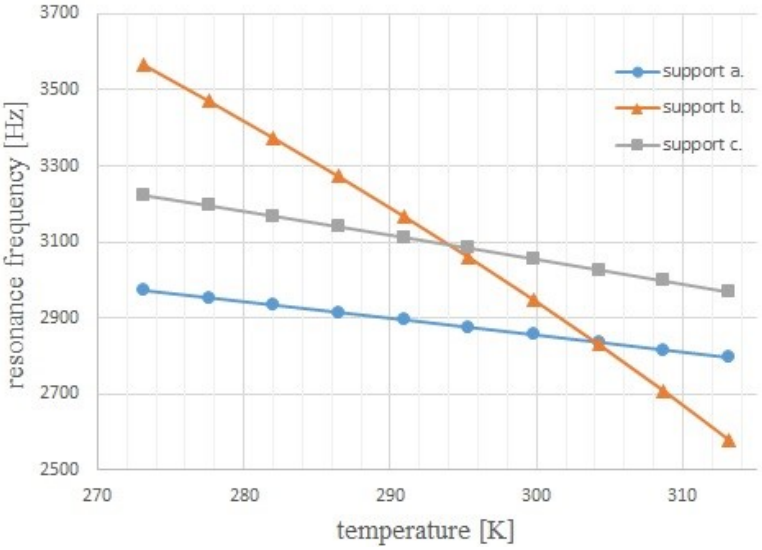

Figure 19: Temperature dependence of the resonance frequency of the first symmetric mode

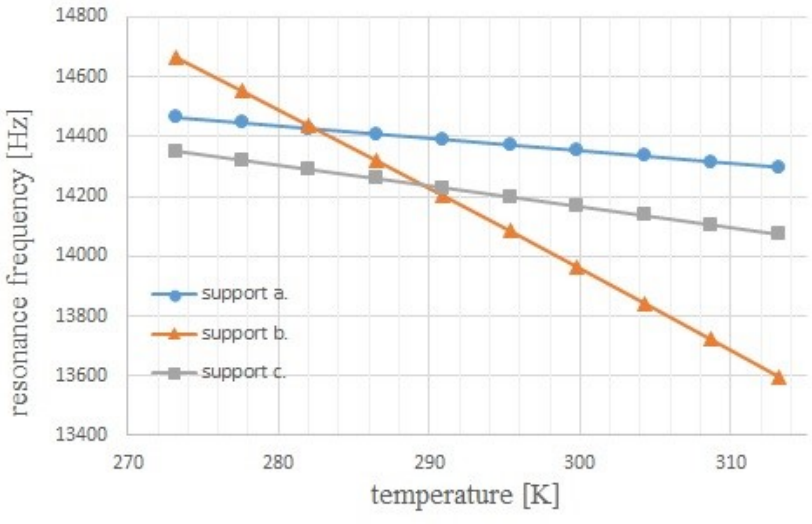

Figure 20: Temperature dependence of the resonance frequency of the first antisymmetric mode

To simulate the dependence of the resonance frequency on the applied force or a given displacement (deformation) the material parameters as listed in Table 1 are used (force load see Figure 3.

Figures 7 and 8 depict the simulation results of the dependence of the resonant frequencies of both, the first symmetric and the first anti-symmetric mode. Structure with the type A suspension-sub-structure, have a negative responsivity Δf / Δd, when Δf and Δd are the change of resonance frequency and the change of displacement, respectively. This is a result of the complex structure design. As expected, the direct clamped structure type (type b) has the highest frequency to displacement ratio but also with the highest temperature dependence ratio.

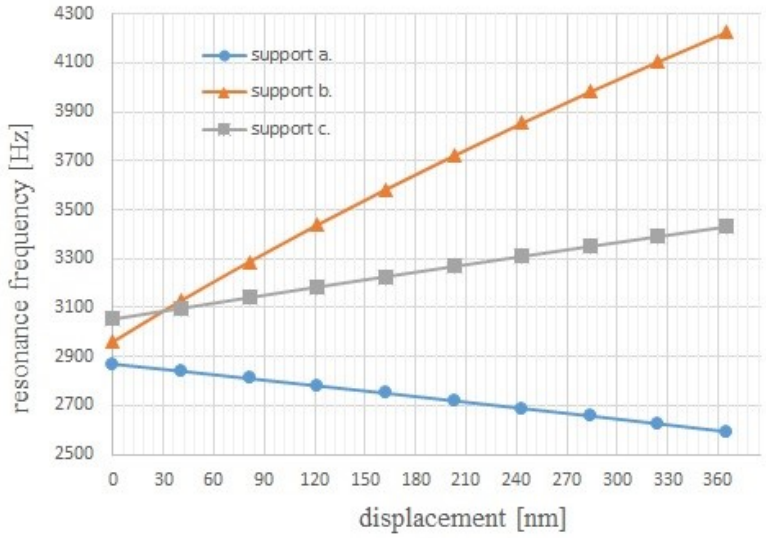

Figure 21: Dependence of the resonance frequency of the symmetric modes from the displacement.

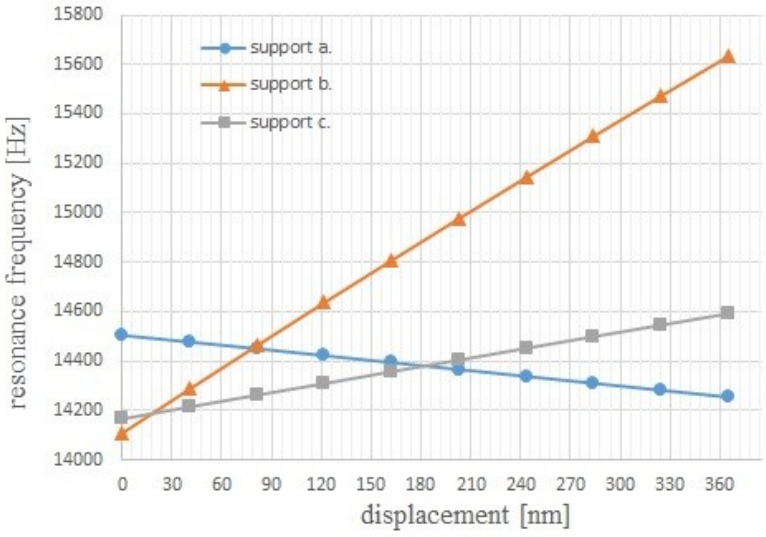

Figure 22: Dependence of the resonance frequency of the anti-symmetric modes from the displacement.

Type A has a temperature compensating substructure with a small meander to eliminate the effect caused by the thermal expansion of the sensing structure relative to the sensor frame [2]. To clarify the effect of the mechanical design two additional layouts are investigated, type B and C, without and with simple compensating structure, respectively. These layouts allow for distinction between compressive stresses and moments by simultaneously using symmetric and antisymmetric modes [7].

6.3 Fabrication and Material Parameters

The device is fabricated with Si-technology using 100 mm SOI-wafer, ⟨100⟩ oriented, with a 350 µm thick handle wafer, a burried oxide layer (250 nm) and a 20 µm Si-device layer. The wafer is coated on both sides with a 70 nm LPCVD silicon nitride layer.

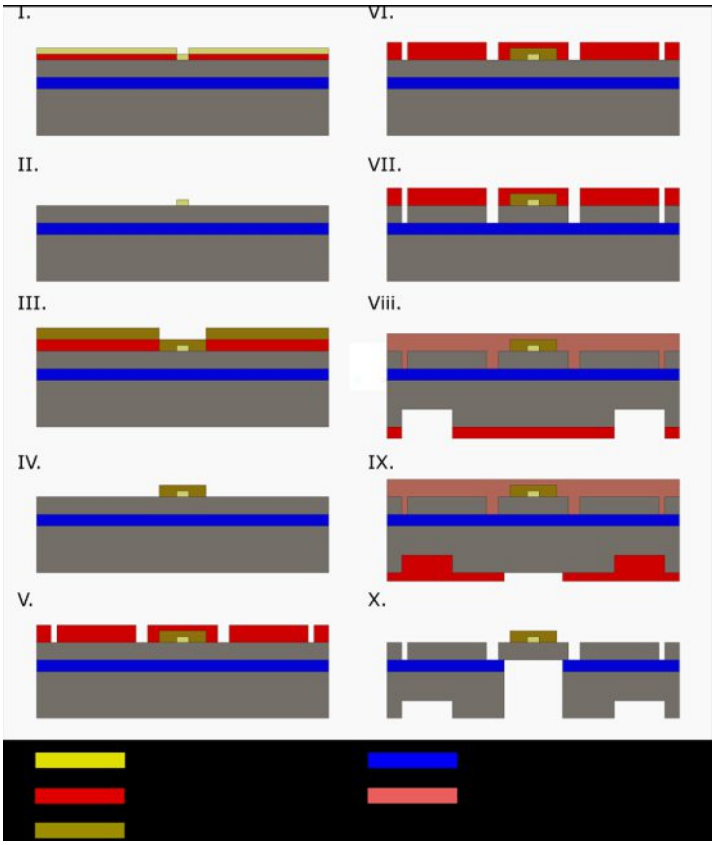

Figure 23: Fabrication process of the sensor using deep reactive ion etching and lift of technique.

Figure 9 depicts the fabrication process. After the first lithography, Pt is evaporated and structured with lift-off. (Fig. 9 I, II). Afterwards, the Au-leads are structured with the second lift-off process (Fig. 9 III, IV). The third photolithography process creates the etching mask for the dry etching process of the device – layer (VI, VII). Now the device layer has to be

protected for the subsequent procedures with a protective resist. After backside etching (Fig. 9 VIII, IX and X) the sensor element is fixed at the four corners in the suspension structure. Now the sensor is separated from the form utilizing an extraction stamp.

The single sensor element is mounted on an aluminum base with epoxide resin, aligned at two sides (see Fig. 10) and connected to a printed circuit board with Au-band wires.

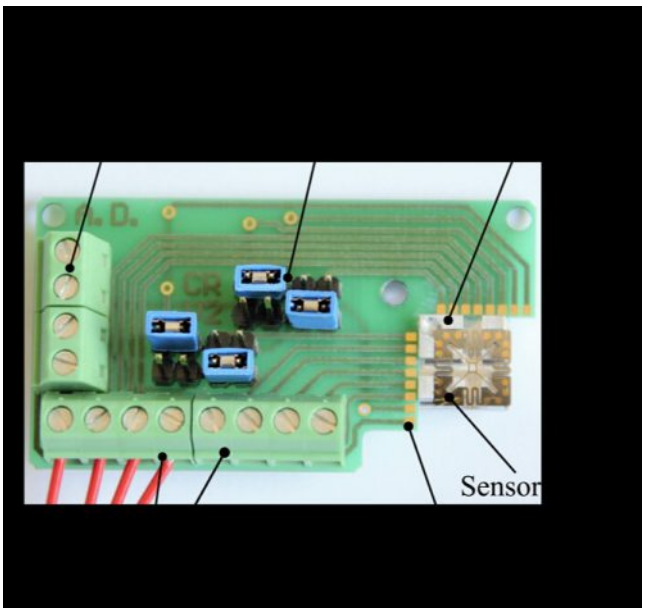

Figure 24: PCB with mounted sensor

Table 1 lists the material parameters for the leads (Au and Pt) and the different layers.

TABLE I: Material parameters for simulation (*depending on crystal orientation on the silicon wafer) and the resistance values.

Symbol	Quantity	value
E	Young's modulus*	170 / 147 GPa
ν	Poisson ratio*	0.28/0.2
k	Thermal conductivity	130 W/mK
ρ	Density	2329 kg/m³
α	Thermal cofficient of expansion	$2.6 \cdot 10^6$ 1/K
$\mathbf{c_p}$	Heat capacity	700 J/kgK
R_{LB1}	resistance of circuit 1	160 Ω
R_{LB2}	resistance of circuit 2	159 Ω
R_{temp}	resistance of platinum element	405 Ω

6.4 Measurements

6.4.3 Measurment Setup

The setup consists first of the sensor chip connected to the printed circuit board, the base plate and the four wire temperature measurement, second the four piezo actuators with their positioning device and third the dipole array for the magnetic field excitation respectively (see Figure 7).

The piezo actuators from “PI-Ceramics” are driven by two power source combined with two E-610 piezo amplifier also from “PI-Ceramics”.

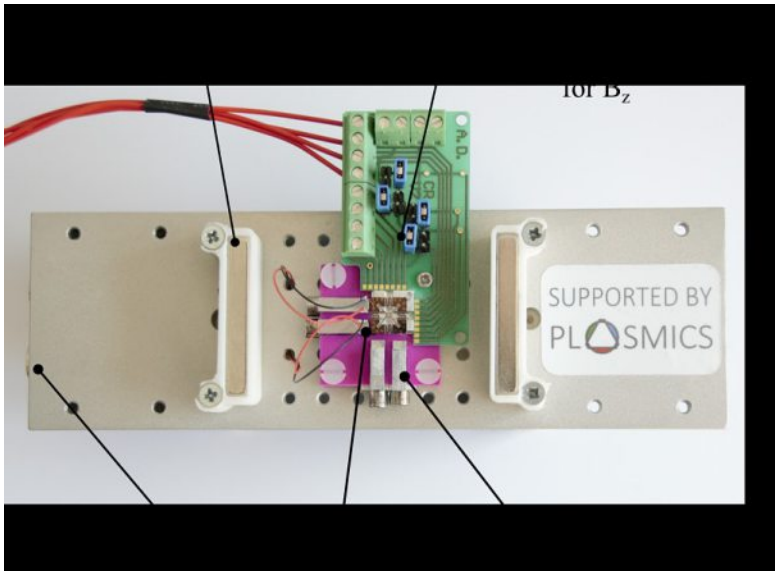

Figure 25: Measurement setup with the sensor package and the piezo actuators. The magnetic stimulation by a permanent magnet dipole

The reference temperature measurement is done with a Pt-lead on the surface of the sensor element which is connected, by four gold wires, to the circuit board. One corner of the MEMS chip is fixed on the Al-base and stick together with the circuit board. The mechanical oscillations of the sensing sub-structures are currently read-out by a micro-system analyzer (Polytec MSA 400) with 10:1 macro lens.

6.4.4 Experiments

The sensor is powered by the function generator of the MSA400 with U_{ss}=0.55 V and I=0.45 mA. A periodic chirp from 2 kHz to 20 kHz is used to excite, the first and second symmetric and anti-symmetric modes. A small excitation amplitude is used to introduce as little heat as possible to the sensing structure to reduce changes of the resonant frequency due to the thermal stress as much as possible. The permanent magnet dipole generates a flux density of 22 mT and consequently deflections of up to 1 nm. The mechanical quality factor Q is approximately 230.

The measured value is the deflection of the sensor frame caused by the piezo actuators as depicted in Fig. 11. The whole operational range of the actuators is used.

With this experiment we measure both, the symmetric and the anti-symmetric deflection which generates a moment with different symmetric offsets.

Different modes are utilized to demonstrate the various effects due to the compressive stress and moments. A large shift of the resonance frequency occurs from a compression stress while using a symmetric mode in contrast to an anti-symmetric mode with a small drift as seen by comparing figure 12, 13 and 14, 15 respectively. The different graphs in figure 13 result from three different compression pre-stresses (symmetric deflection). Noteworthy is the good correlation between measurement and simulation of the gradient. The deviation of the experimental results from the simulated results influenced by the measurement setup itself and fabrication tolerances from the sensing structure suspensions.

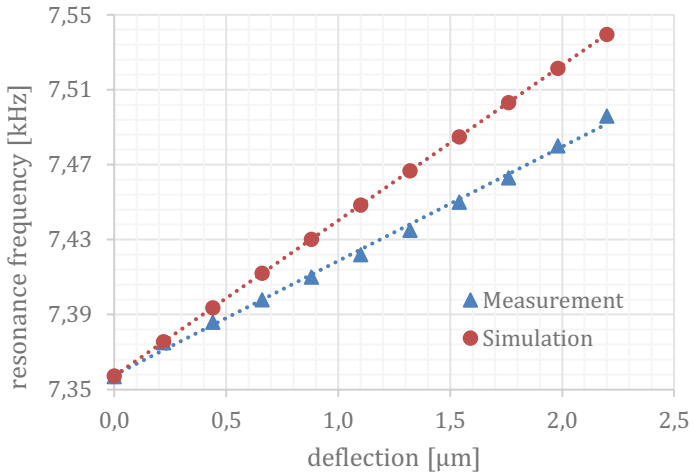

Figure 26: Shift of the resonance frequency of the second symmetric mode (7.36 kHz) by a parallel symmetric load state from both piezo actuators of 2.5 µm. Measurement results in comparison with the simulated values.

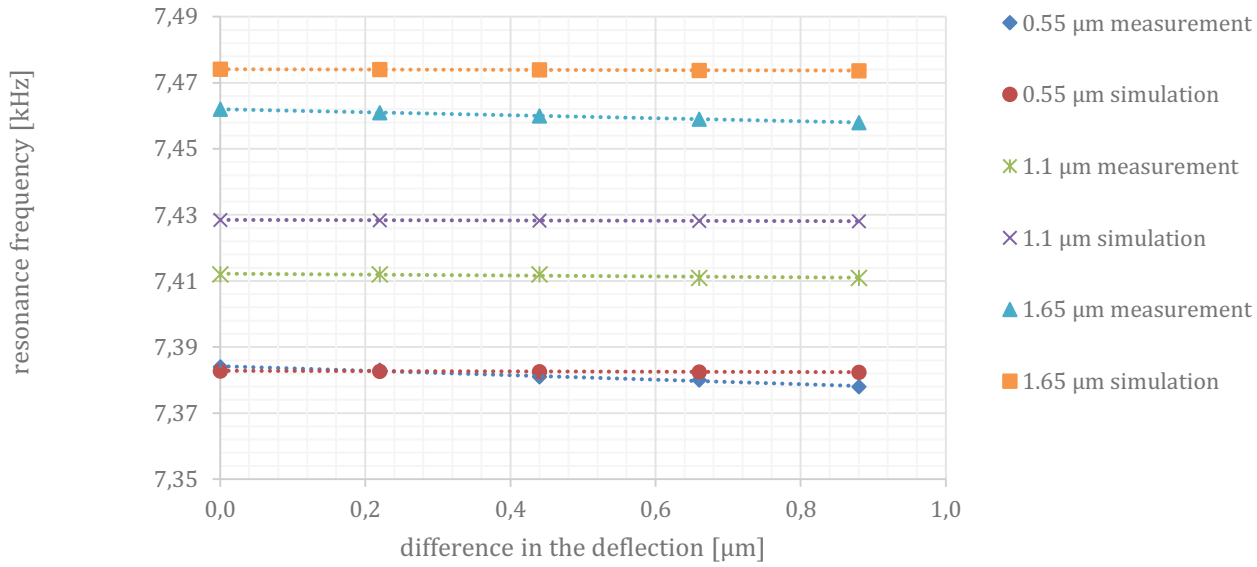

Figure 27: Shift of the resonance frequency of the second symmetric mode (7.36 kHz) stressed by a moment and with a superimposed compressive force. Measurement results in comparison with the simulated values.

The corresponding situation for the antisymmetric mode is depicted in Fig. 14, 15 and 16. Hence, a moment acting on the sensor changes the resonant frequency of the second antisymmetric mode by 300 Hz/µm, where as the resonant frequency for symmetric load is only slightly influenced (1Hz/µm).

The temperature of the device layer (including the sensing structure) was 24.6°C throughout the whole experiment, measured with the two Pt elements as described in section I.

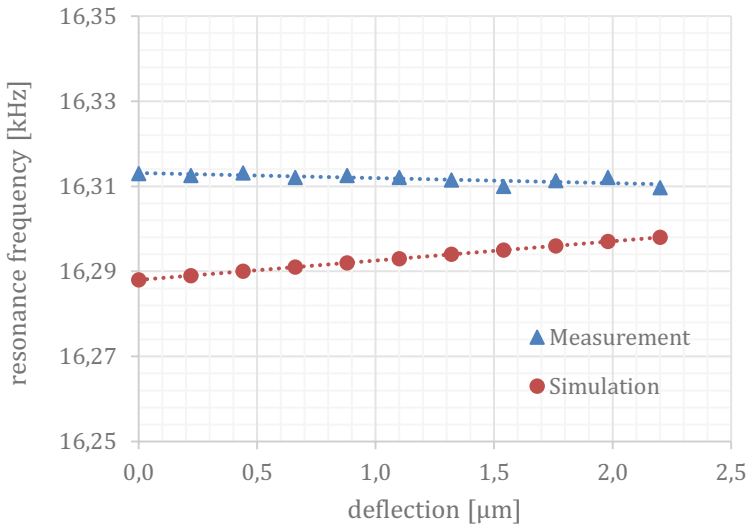

Figure 28: Shift of the resonance peak of the second anti-symmetric mode (16.3 kHz) by a parallel load state from both piezo actuators of 2.5 µm. Measurement results in comparison with the simulated values.

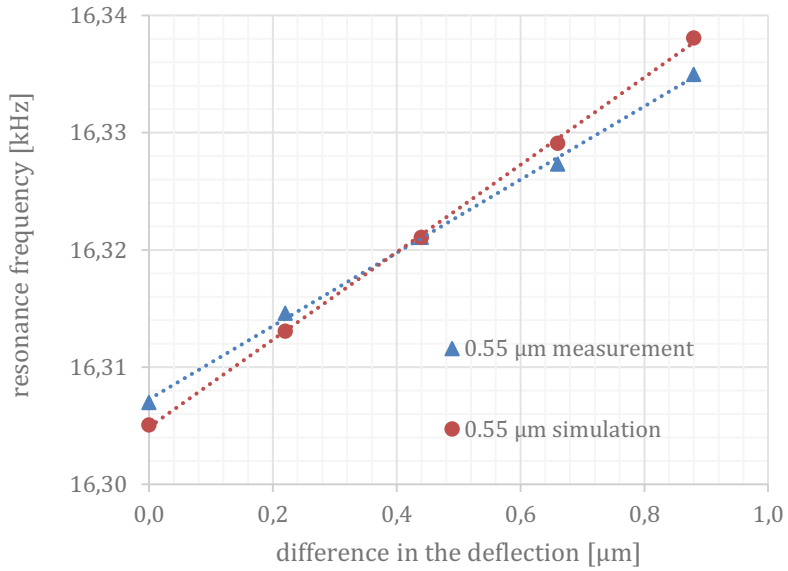

Figure 29: Shift of the resonance peak of the second anti-symmetric mode (16.3 kHz) stressed by a moment and with a superimposed compressive force. Measurement results in comparison with the simulated values.

6.5 Conclusion and Outlook

A resonant MEMS force and displacement sensor is presented to measure both, the compressive force and the moment acting on the device using two different vibration modes (one symmetric and one anti-symmetric) to distinguish the two load states, generated with two piezo actuators. A frequency change of 63 Hz/µm occurs while measuring a compressive force load state and a symmetric mode. This allows a sensitivity down to 15 nm/Hz up to now.

The measurements reveal that compressive forces and moments can be easily distinguished from each other by measuring both vibrating modes separately. To decrease the temperature effect of the silicon material and the oxide layer between support and sensing material, low power combined with short measuring intervals is used to excite the sensing structure.

Next step is the Readout with piezo resistive elements. Caused thru this mentioned method, it will push up the possible applications thru the miniaturizing of the complete sensor.

Acknowledgment

This paper is part of the “PikoSens” project funded from the AWS (Austrian economy service) at the TUW (technical university Vienna).

6.6 References

[22] M- Amjadi, “Highly stretchable and sensitive strain sensors based on silver nanowire-elastomer nanocomposite”, ACS Nano, 2015, vol 8 issue 5, pp 5154 ff.

[23] A. Dabsch, “Temperature dependency of silicon structures for magnetic field gradient sensing” Journal of Micromechanics and Microengineering, July 2017.

[24] A. Sieber, “A novel haptic platform for real time bilateral biomanipulation with a MEMS sensor for triaxial force feedback”, Sensors and Actuators A: Physical, vol 142, issue 1, March 2008, pp 19-27.

[25] S. Bütefisch, “Micromechanical three-axial tactile force sensor for micromaterial characterisation”, Microsystem Technologies, vol 7, issue 4, pp 171-174.

[26] F. Beyler, “A-Six-Axis MEMS Force-Torque Sensor with Micro-Newton and Nano-Newtonmeter Resolution”, Journal of Microelectromechanical Systems, vol. 18, pp. 433-441, 2009.

[27] A. Nakai, “6-Axis force-torque sensor chip composed of 16 piezoresistive beams”, The 28th IEEE International Conference on Micro Electro Mechanical Systems (MEMS2015), Estoril, Portugal, 18-22 January, pp.730-733, 2015.

[28] A. Dabsch; “MEMS cantilever based magnetic field gradient sensor”; Journal of Micromechanics and Microengineering; April 2017

[29] J. Acevedo-Mijagos; “Design and modelling of a novel microsensor to detect magnet field in two orthogonal directions”; Microsystem Technology; April 2013.

VII. Publication Five

Two dimensional displacement measurement with MEMS structure

Authored by A. Dabsch, C. Rosenberg, P. Klug, M. Stifter and F. Keplinger
Published in: Journal of Journal of Micromechanics and Microengineering

Abstract

In this letter we present a MEMS Sensor to measure displacement in at least two directions. The sensor device is a resonant, Lorentz force driven and cross-shaped sensing structure whereas the measurement signal is the change of the resonance frequency induced by the deformation of the sensor-frame. This device is a pre-study to implement the sensor in a two-dimensional micro manipulation system for which the team uses a micro system analyzer to detect the resonance frequencies of the different vibration modes. The sensor-frame deformation between 0.1 and 2 µm is generated by four piezo actuators. With this setup, the sensor achieves a sensitivity of up to 20 nm/Hz. The device is fabricated from a 100 mm SOI wafer with standard CMOS processes and has two Pt1000 elements integrated on the device layer to compensate any effects caused by thermal extension of the structure or temperature induced changes of material parameters.

7.1 Introduction

Multiaxial displacement sensing is required in many applications: Atomic force microscopes (AFM) that use a two dimensional displacement measurement to detect both the atomic structure of the surface and the lateral deviation of the spring-like cantilever [1] (where the difference in the deviation between lateral and vertical displacement amounts to two orders of magnitude), as well as the industrial automation systems (e.g. quality management for production facility) or micromanipulation systems.

Beyeler et. al. presented a six degrees of freedom sensor that is able to measure force and torque simultaneously by comparing seven capacitors mounted at the tips of a complex

sensing structure [2]. They reach resolutions down to mirco-Newton and nano-Newtonmeter measuring force and torque respectively.

Another sensor with six degrees of freedom is invented by Brookhuis et. al. in 2013 and uses a capacitive readout for biomechanical applications [3] and exhibits a range of up to 50 N exterior load.

The presented sensor concept is already described in previous work but only with a one-dimensional measurement (one force and one moment respectively) [4]. We apply a resonant cross-shaped and Lorentz-force stimulated sensing structure supported in the sensor frame with a temperature compensating sub-structure (see Figure 1) [5]. The sensor frame is divided into four identical parts, connected by four meander sub-structures that enable the deformation of the sensor frame and the sensing structure respectively. To generate a determinable signal change, only very little strain is necessary as compared to common strain sensors [6].

The exterior load detunes the resonance frequencies of the cross-shaped sensing-structure. To detect the complete load-set, we use the resonance frequency change of at least two vibration modes. The homogenous magnetic field is generated by a permanent magnet dipole with a flux density of 22 mT in the area of the sensing structure.

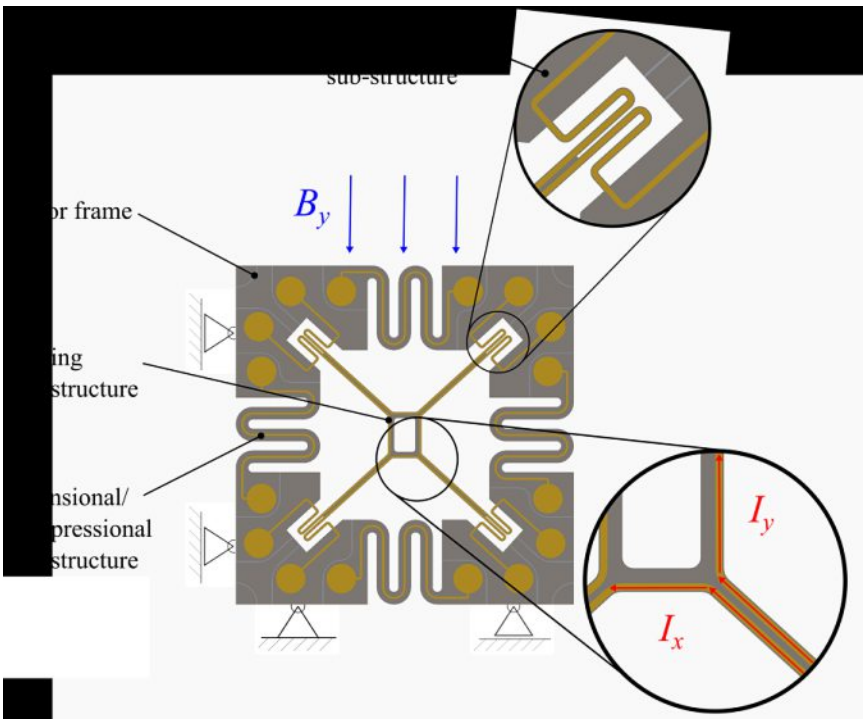

Figure 30: sensor concept of the sensing device made out of a 100 mm SOI wafer. With gold leads (stimulation) and Pt-leads (temperature measurement)

7.2 Simulation and Theory

The simulations are performed with COMSOL Multiphysics ® 5.2. The corresponding material parameters and the measurement parameters of the circuits are listed in Table 1.

TABLE I: Material parameters for simulation (*depending on crystal orientation on the silicon wafer), geometrical parameters of the meander and the resistance values of the circuits.

Symbol	Quantity	value
E	Young's modulus*	170 / 147 GPa
v	Poisson ratio*	0.28/0.2
k	Thermal conductivity	130 W/mK
ρ	Density	2329 kg/m³
α	Thermal cofficient of expansion	$2.6 \cdot 10^{-6}$ 1/K
R_{LB1}	resistance of circuit 1	160 Ω
R_{LB2}	resistance of circuit 2	159 Ω
R_{temp}	resistance of platinum	405 Ω
h	height of the meander	0.6 mm
b	width of the meander	0.26 mm
l	length of the meander	5.95 mm

To compare the simulations with the measurement data, the four piezo actuators are approximated by distributed loads on the sensor frame. With respect to the limitation in the positioning accuracy of the contact surface of the piezo actuators in relation to the sensor frame, there is an individual preload of the adjacent pressure marks within the simulation, but nevertheless with the same load set. The preload set in the simulation is designed after the complete assembly and adjustment is performed at the measuring device to match the adjusted resonance frequency of the basic vibration mode after the positioning of the piezo actuators.

To avoid non-linearities of the extension of the piezo actuators, not the entire possible range of 2.2 µm deflection is used. Therefore, an additional preload is applied to fix inaccuracies of the positioning toward the rotation of the piezo actuator against the sensor frame.

The spring constant of the extensional/compressional sub-structure (meander) of the sensor frame is approximately calculated to estimate the needed force or stress acting on the sensor frame [7]. A displacement of 2 µm is desired and the maximum applicable force coming from

the piezo actuator is 11.2 N. A first approximation of the spring constant originating from the bending beam can be assumed as:

$$c_M = \frac{3EI_z}{l^3} \tag{1}$$

where c_M is the spring constant of the meander, E is the Young's modulus of silicon (this approach neglects the 100 nm thick oxide layer between device- and handle layer), I_z is the second moment of area referred to the z-axis and l is the length of the meander structure. Using the parameters from Table 1 delivers $c_M \approx 1.77$ N/mm as well as $\sigma \approx 1850$ Pa.

The temperature dependence of the sensing structure is already simulated in [8]. The suspension sub-structure used in this work (see Figure 1) has a temperature dependence of approximately 1 Hz/K [5, figure 7], which is small if we consider the short measurement time (duration between the first capture of the resonance frequency, adjustment of the piezo actuator and the second capture of the changed resonance frequency) in relation to the small heat absorption of the sensor in this setup.

Using the calculated stress or the resulting displacement in the simulation model (F_x), we get resonance frequency changes of 110 Hz and -67 Hz for the second and fourth vibration mode respectively. These values are also stable, changing the preload of the other stress direction (F_y).

7.3 Experiments and Results

The measurement setup allows for loads in x- and y- direction (see Figure 2) and is realized by contacting four 2*2*2 mm piezo actuators on the sensor frame with micrometer screws, driven by two E-610 piezo amplifiers from "PI-Ceramics" (see Figure 3).

In addition to the depicted forces (F_x and F_y), there a three more potential degrees of freedom for measurement (namely three torques around the x-, y-, and z-axis) deforming the sensor frame. For each load, another vibration mode is used to characterize the complete load-set. Furthermore, it is necessary to note that it is possible to choose arbitrary resonance modes as long as the change of the resonance frequency of the selected modes is different.

In this work the sensor output is the change of the resonance frequency compared to the displacement of the sensor frame and thus the position of the suspension points of the sensing structure respectively. In this early stage of the sensor development, the resonance frequency is detected with a Polytec MSA 400 micro system analyzer.

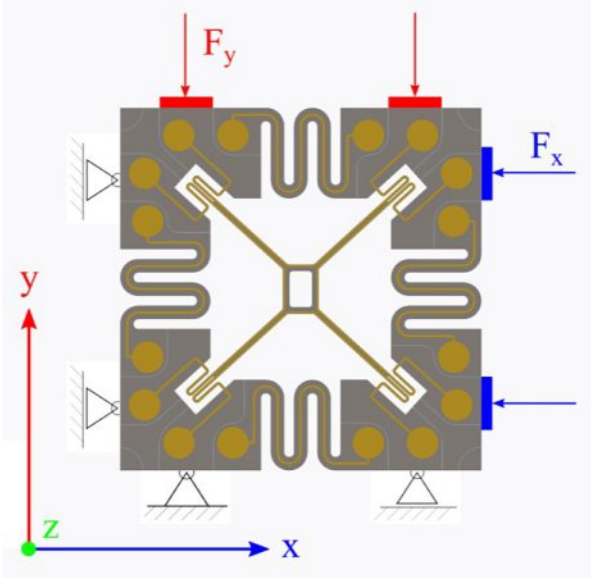

Figure 31: The principle of the measurement setup with forces in x- and y-direction.

Two permanent magnets in a dipole array create a flux density of 22 mT and with an electrical current of 1.2 mA, the Lorentz force excites deflections at a resonance of up to 20 nm.

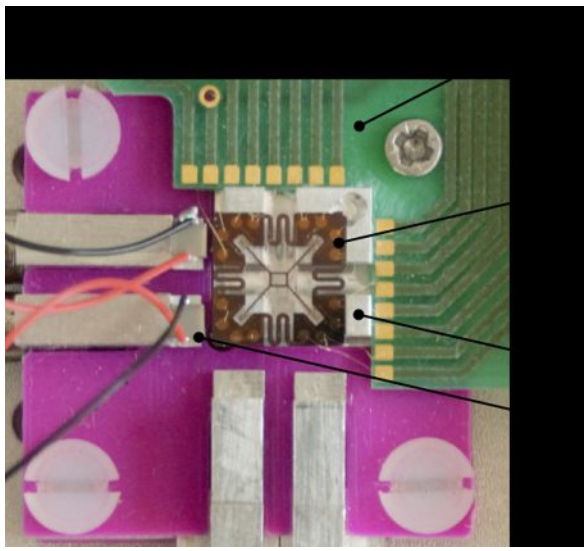

Figure 32: Measurement setup with the piezo-actuators and the MEMS device: 1. PCB; 2. MEMS chip; 3. piezo-actuator; 4. sensor mounting

Figures 4 and 5 depict the measurement results for the both selected vibration modes. Comparing with the almost linear frequency drift from the simulations we see slight rejection from the linearity causing through the measuring device and the piezo-positioning. Consider the change of the resonance frequency as a function of the displacement of the piezo actuators, we see changes of the resonance frequency around 106 Hz and -72 Hz respectively what is in good condition with the simulation results.

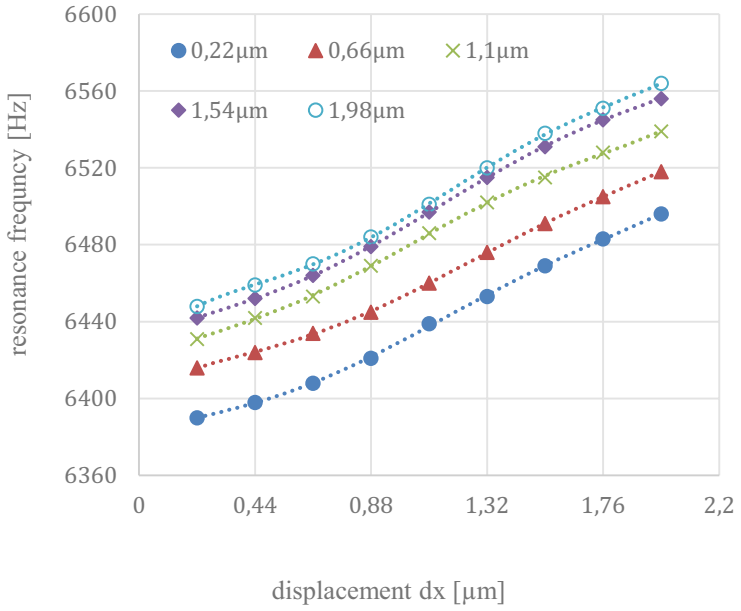

Figure 33: two dimensional displacement measurement using the second symmetric vibration mode; max. displacement +2µm; max. resonance frequency change 170 Hz. The different graphs represents the displacement in y-direction. The standard deviation within this measurement is 4 Hz in average.

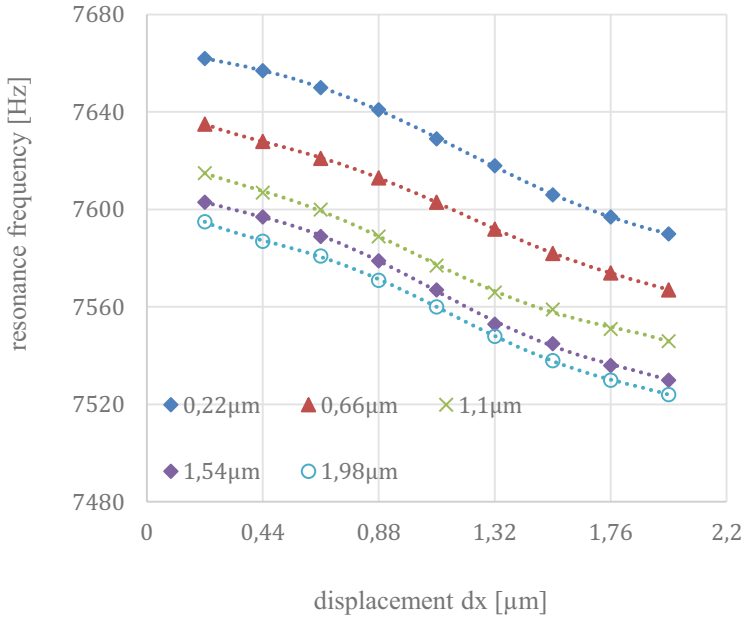

Figure 34: two dimensional displacement measurement using the fourth symmetric vibration mode; max. displacement +2µm; max. resonance frequency change 138 Hz. The different graphs represents the displacement in y-direction. The standard deviation within this measurement is 4.5 Hz in average.

7.4 Conclusion and Outlook

The presented sensor concept enables simultaneous measurement of two displacement directions that are perpendicular to each other. The setup consists of a resonant Lorentz force stimulated MEMS device and four piezo-actuators to realize the lateral displacement. The change of the resonance frequency of the sensing structure is the measurement output signal of the sensor. For a displacement of 2 µm, we get a change of 100 Hz of the resonance frequency at the second antisymmetric and 70 Hz at the third antisymmetric mode. The sensitivity of the sensor in this stage is 20 nm/Hz (standard deviation 0.6 Hz) with a resolution of 0.5 Hz from the micro-system-analyzer.

In a further step, the team will develop a piezo-resistive readout [8] integrated in the sensing structure suspensions to miniaturize the sensor concept and to enlarge the field of application. Furthermore, an encapsulation of the sensor will be created to minimize environmental influences on the sensing structure. To this end, an elastic connecting element will have to be designed to avoid effects of the encapsulation on the sensor function.

7.5 References

[1.] K.M. Lang; Conducting atomic force microscopy for nanoscale tunnel barrier characterization; Review of Scientific Instruments 2726 (2004); Volume 75; Issue 8

[2.] J. M. R. Weaver; High resolution atomic force microscopy potentiometry; Journal of Vacuum Science & Technology B: Microelectronics and Nanometer Structures Processing, Measurement, and Phenomena Volume 9, Issue 3

[3.] F. Beyeler; A six-axis MEMS force-torque sensor with micro-newton and nano-newtonmeter resolution; journal of microelectromechanical systems; vol.18; issue 2; April 2009

[4.] P. Estevez; "6 DOF force and torque sensor for micro-manipulation applications", Sensor. Actuat. A-Phys., vol. 186, pp. 86-93, 2011.

[5.] A. Dabsch; Multiaxial Resonant MEMS Force Sensor;
Journal of Micromechanics and Microengineering XXX

[6.] M- Amjadi, “Highly stretchable and sensitive strain sensors based on silver nanowire-elastomer nanocomposite”, ACS Nano, 2015, vol 8 issue 5, pp 5154 ff.

[7.] M.A. Hopcroft, W.D. Nix and T.W. Kenny, ”What is the Young´s Modulus of Silicon”, MEMS IEEE, vol. 19, no. 2, pp. 229-238, April 2010.

[8.] A. Dabsch, “Temperature dependency of silicon structures for magnetic field gradient sensing” Journal of Micromechanics and Microengineering, July 2017.

[9.] A. Rahafrooz; High-Frequency Thermally Actuated Electromechanical Resonators with Piezoresistive Readout; IEEE Transactions on electron devices; vol. 58; Issue 4 April 2011

Publication XI

(12) NACH DEM VERTRAG ÜBER DIE INTERNATIONALE ZUSAMMENARBEIT AUF DEM GEBIET DES PATENTWESENS (PCT) VERÖFFENTLICHTE INTERNATIONALE ANMELDUNG

(19) Weltorganisation für geistiges Eigentum
Internationales Büro

(43) Internationales Veröffentlichungsdatum
04. Oktober 2018 (04.10.2018)

WIPO | PCT

(10) Internationale Veröffentlichungsnummer
WO 2018/176069 A1

(51) Internationale Patentklassifikation:
G01L 1/10 (2006.01) *G01L 5/16* (2006.01)

(21) Internationales Aktenzeichen: PCT/AT2017/060082

(22) Internationales Anmeldedatum:
31. März 2017 (31.03.2017)

(25) Einreichungssprache: Deutsch

(26) Veröffentlichungssprache: Deutsch

(71) Anmelder: **TECHNISCHE UNIVERSITÄT WIEN** [AT/AT]; Karlsplatz 13, 1040 Wien (AT).

(72) Erfinder: **DABSCH, Alexander**; Hietzinger Hauptstraße 56, 1130 Wien (AT). **KEPLINGER, Franz**; Gerasdorfer Straße 153/70, 1210 Wien (AT). **ROSENBERG, Christoph**; Dr.-Karl-Renner-Gasse 31/1, 2542 Kottingbrunn (AT).

(74) Anwalt: **KLIMENT & HENHAPEL PATENTANWALTE OG**; Singerstrasse 8/3/9, 1010 Wien (AT).

(81) Bestimmungsstaaten *(soweit nicht anders angegeben, für jede verfügbare nationale Schutzrechtsart)*: AE, AG, AL, AM, AO, AT, AU, AZ, BA, BB, BG, BH, BN, BR, BW, BY, BZ, CA, CH, CL, CN, CO, CR, CU, CZ, DE, DJ, DK, DM, DO, DZ, EC, EE, EG, ES, FI, GB, GD, GE, GH, GM, GT, HN, HR, HU, ID, IL, IN, IR, IS, JP, KE, KG, KH, KN, KP, KR, KW, KZ, LA, LC, LK, LR, LS, LU, LY, MA, MD, ME, MG, MK, MN, MW, MX, MY, MZ, NA, NG, NI, NO, NZ, OM, PA, PE, PG, PH, PL, PT, QA, RO, RS, RU, RW, SA, SC, SD, SE, SG, SK, SL, SM, ST, SV, SY, TH, TJ, TM, TN, TR, TT, TZ, UA, UG, US, UZ, VC, VN, ZA, ZM, ZW.

(54) **Title:** FORCE SENSOR

(54) **Bezeichnung:** KRAFTSENSOR

WO 2018/176069 A1

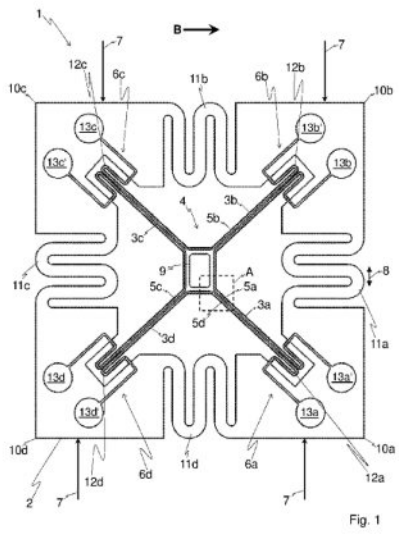

Fig. 1

(57) **Abstract:** Force sensor (1) comprising a frame (2) and also an oscillation structure (4) which has a plurality of arms (3a-d) and can oscillate freely in the frame (2), wherein the arms (3a-d) are fixed to suspension regions (6a-d) of the frame (2) and run transverse to one another at least in sections, wherein at least one guiding means (5a-d) is provided, which guiding means extends along at least two arms (3a-b; 3b-c; 3c-d; 3d-a), wherein an AC voltage can be applied to the at least one guiding means (5a-d) in order to excite at least one oscillation mode of the oscillation structure (4) with a resonant frequency using Lorentz force (F_L), wherein the force sensor (1) is designed such that the suspension regions (6a-d) are at least partially spatially displaced relative to one another when a force (7) is applied to the frame (2), that the magnitude of the spatial displacement (8) of the suspension regions (6a-d) depends on the magnitude of the force (7), that the spatial displacement (8) of the suspension regions (6a-d) causes detuning of the resonant frequency, the magnitude of which depends on the magnitude of the spatial displacement (8).

(57) **Zusammenfassung:** Kraftsensor (1) umfassend einen Rahmen (2) sowie eine Schwingstruktur (4), die mehrere Arme (3a-d) aufweist und im Rahmen (2) frei schwingen kann, wobei die Arme (3a-d) an Aufhängungsbereichen (6a-d) des Rahmens (2) fixiert sind und zumindest abschnittsweise quer zueinander verlaufen, wobei mindestens ein Leitmittel (5a-d) vorgesehen ist, das sich entlang von zumindest zwei Armen (3a-b; 3b-c; 3c-d; 3d-a) erstreckt, wobei das mindestens eine Leitmittel (5a-d) mit einer Wechselspannung beaufschlagbar ist, um unter Ausnutzung der Lorentz-Kraft (F_L) mindestens eine Schwingungsmode der Schwingstruktur (4) mit einer Resonanzfrequenz anzuregen, wobei der Kraftsensor (1) so ausgelegt ist, dass sich die Aufhängungsbereiche (6a-d) zumindest teilweise räumlich relativ zueinander

[Fortsetzung auf der nächsten Seite]

WO 2018/176069 A1

(84) **Bestimmungsstaaten** *(soweit nicht anders angegeben, für jede verfügbare regionale Schutzrechtsart)*: ARIPO (BW, GH, GM, KE, LR, LS, MW, MZ, NA, RW, SD, SL, ST, SZ, TZ, UG, ZM, ZW), eurasisches (AM, AZ, BY, KG, KZ, RU, TJ, TM), europäisches (AL, AT, BE, BG, CH, CY, CZ, DE, DK, EE, ES, FI, FR, GB, GR, HR, HU, IE, IS, IT, LT, LU, LV, MC, MK, MT, NL, NO, PL, PT, RO, RS, SE, SI, SK, SM, TR), OAPI (BF, BJ, CF, CG, CI, CM, GA, GN, GQ, GW, KM, ML, MR, NE, SN, TD, TG).

Veröffentlicht:

— *mit internationalem Recherchenbericht (Artikel 21 Absatz 3)*

verschieben, wenn der Rahmen (2) mit einer Kraft (7) beaufschlagt wird, dass die Größe der räumlichen Verschiebung (8) der Aufhängungsbereiche (6a-d) von der Größe der Kraft (7) abhängt, dass die räumliche Verschiebung (8) der Aufhängungsbereiche (6a-d) eine Verstimmung der Resonanzfrequenz bewirkt, deren Größe von der Größe der räumlichen Verschiebung (8) abhängt.

KRAFTSENSOR

GEBIET DER ERFINDUNG

Die vorliegende Erfindung betrifft einen Kraftsensor umfassend einen Rahmen sowie eine Schwingstruktur, die mehrere Arme aufweist und im Rahmen frei schwingen kann.

STAND DER TECHNIK

In der Praxis werden zur Messung von Kräften üblicherweise Dehnmessstreifen verwendet, welche an Bauteilen, die Kräften ausgesetzt sind und sich dabei verformen, befestigt werden. Über die ermittelte Dehnung kann so indirekt auf die Kraft rückgerechnet werden. Dehnmessstreifen sind zwar relativ genau und können bei Verwendung mehrerer, quer zueinander angeordneter Dehnmessstreifen auch zur Vermessung von Kraftvektoren in zumindest zwei Dimensionen verwendet werden. Grundsätzliche Probleme ergeben sich jedoch bei der Bestimmung von Druckkräften sowie durch Imperfektionen bei der Montage der Dehnmessstreifen, welche üblicherweise durch Kleben erfolgt.

Darüberhinaus treten bei gewissen Anwendungen, insbesondere bei Anwendungen der Biologie und/oder Medizin, sehr kleine Kräfte im Bereich von kleiner gleich 1 µN oder sogar kleiner gleich 1 nN (also im Piko-Newton-Bereich) auf. Derart kleine

Kräfte können mit Dehnmessstreifen üblicherweise nicht gemessen werden.

AUFGABE DER ERFINDUNG

Es ist daher Aufgabe der vorliegenden Erfindung, eine verbesserte Möglichkeit zur Messung von Kräften zu schaffen, die die oben geschilderten Nachteile vermeidet. Insbesondere sollen sehr kleiner Kräfte, vorzugsweise bis in den pN-Bereich, gemessen werden können.

DARSTELLUNG DER ERFINDUNG

Kern der Erfindung zur Lösung der genannten Aufgabe ist es, einen Kraftsensor mit einer Schwingstruktur zur Verfügung zu stellen, welche Schwingstruktur in einem Magnetfeld durch Beaufschlagung mit Wechselstrom zum Schwingen angeregt werden kann und deren Resonanzfrequenz sich ändert, wenn eine auf den Kraftsensor einwirkende Kraft zu einer Verzerrung des Kraftsensors führt. Die resultierende Verstimmung der Resonanzfrequenz ist ein Maß für die Größe der Verzerrung und somit für die Größe der einwirkenden Kraft. Durch Dimensionierung und Design der Struktur des Kraftsensors, insbesondere als MEMS (micro electro mechanical system), und in Abhängigkeit vom Auflösungsvermögen der Frequenzmessung können somit sehr kleine Kräfte gemessen werden, die im nN- oder sogar pN-Bereich liegen.

Daher ist erfindungsgemäß ein Kraftsensor umfassend einen Rahmen sowie eine Schwingstruktur, die mehrere Arme aufweist und im Rahmen frei schwingen kann, vorgesehen, wobei die Arme an Aufhängungsbereichen des Rahmens fixiert sind und zumindest abschnittsweise quer zueinander verlaufen, wobei mindestens ein Leitmittel vorgesehen ist, das sich entlang von zumindest

zwei Armen erstreckt, um einen Stromfluss in Form von bewegten Ladungsträgern zumindest zwischen zwei Aufhängungsbereichen zu ermöglichen, wobei das mindestens eine Leitmittel mit einer Wechselspannung beaufschlagbar ist, um, insbesondere in einem unbelasteten Zustand des Kraftsensors, unter Ausnutzung der Lorentz-Kraft mindestens eine Schwingungsmode der Schwingstruktur mit einer Resonanzfrequenz anzuregen, wenn sich die Schwingstruktur in einem Magnetfeld befindet, wobei der Kraftsensor so ausgelegt ist, dass sich die Aufhängungsbereiche zumindest teilweise räumlich relativ zueinander verschieben, wenn der Rahmen mit einer Kraft beaufschlagt wird, dass die Größe der räumlichen Verschiebung der Aufhängungsbereiche von der Größe der Kraft abhängt, dass die räumliche Verschiebung der Aufhängungsbereiche eine Verstimmung der Resonanzfrequenz bewirkt und dass die Größe der Verstimmung von der Größe der räumlichen Verschiebung der Aufhängungsbereiche abhängt.

D.h. jeder Arm weist ein Ende bzw. einen Endbereich auf, mit dem er an einem der Aufhängungsbereiche fixiert ist.

Weiters weist jeder Arm einen Abschnitt auf, der zumindest zu einem Abschnitt eines anderen Arms quer verläuft. Vorzugsweise verläuft jeder Arm dabei zumindest abschnittsweise geradlinig, wobei ein zumindest abschnittsweise gekrümmter Verlauf jedoch auch denkbar ist.

Die Erstreckung des Leitmittels entlang der zumindest zwei Arme ist vorzugsweise als durchgehend zu verstehen, um den Stromfluss entlang dieser Arme zu ermöglichen. Aufgrund der Kopplung des mindestens einen Leitmittels mit den Armen bzw. der Schwingstruktur kann auch auf die Schwingstruktur die Lorentz-Kraft wirken, wenn sich die Schwingstruktur bzw. der Kraftsensor im Magnetfeld befindet. Wird nun das mindestens eine Leitmittel mit einer Wechselspannung beaufschlagt und befindet sich die Schwingstruktur bzw. deren Arme in einem

Magnetfeld, so wird aufgrund der sich ergebenden oszillierenden Lorentz-Kraft eine Schwingung der Schwingstruktur angeregt. Dabei kann, insbesondere bei einem zeitlich statischen oder sich nur vergleichsweise langsam ändernden Magnetfeld, eine besonders effektive Anregung erfolgen, indem die Frequenz des Wechselstroms einer Resonanzfrequenz der Schwingstruktur bzw. einer Schwingungsmode der Schwingstruktur entspricht.

Eine herstellungstechnisch vorteilhafte Ausführungsform des Kraftsensors ergibt sich, indem als das mindestens eine Leitmittel eine Leiterbahn, z.B. aus Gold der Platin, vorgesehen ist. Die Leiterbahn verläuft entsprechend zumindest abschnittsweise entlang der Längsrichtung eines Arms und zumindest abschnittsweise entlang der Längsrichtung eines anderen Arms.

Um einen Schutz des mindestens einen Leitmittels gegen äußere Einflüsse sicherzustellen, kann es auch vorgesehen sein, dass das mindestens eine Leitmittel in die Schwingstruktur bzw. in deren Arme integriert ist. In diesem Fall kann das mindestens eine Leitmittel beispielsweise als mikromechanische Struktur aus Metall, insbesondere aus Aluminium ausgeführt sein.

Denkbar wäre es auch, die Schwingstruktur bzw. deren Arme sowie das mindestens eine Leitmittel zumindest abschnittsweise einstückig auszuführen um auszuschließen, dass das mindestens eine Leitmittel durch die Schwingungen der Schwingstruktur mechanisch beschädigt oder gar zerstört wird. D.h. in diesem Fall ist die Schwingstruktur bzw. sind deren Arme zumindest abschnittsweise selbst elektrisch leitend.

Zur räumlichen Verschiebung der Aufhängungsbereiche ist zu bemerken, dass es z.B. denkbar ist, dass die einwirkende Kraft bzw. die einwirkenden Kräfte so orientiert ist bzw. sind, dass zwei Aufhängungsbereiche denselben Abstand zu einander beibehalten und zu anderen Aufhängungsbereichen nicht.

Eine Verstimmung der Resonanzfrequenz wird insbesondere gegenüber einem unbelasteten Zustand, wo also keinerlei Kraft auf den Kraftsensor einwirkt, erzielt. Darüberhinaus ergibt sich eine Verstimmung der Resonanzfrequenz aber natürlich auch gegenüber einem zuvor vorhandenen Zustand, wo bereits eine (zumindest etwas andere) Krafteinwirkung vorgeherrscht hat und eine gegenüber dem unbelasteten Zustand andere Resonanzfrequenz vorgelegen ist. Mit anderen Worten hat auch eine Änderung einer Krafteinwirkung eine Änderung bzw. Verstimmung der Resonanzfrequenz zur Folge.

Es sei bemerkt, dass grundsätzlich unterschiedliche Schwingungsmoden angeregt werden können. Insbesondere können auch gezielt Schwingungsmoden angeregt werden, deren Resonanzfrequenz speziell sensitiv auf Verzerrungen bzw. Verschiebungen nur in einer bestimmten Richtung sind, womit eine richtungsaufgelöste Kraftmessung erfolgen kann. Bei Anregbarkeit von solchen Schwingungsmoden für zwei linear unabhängige Richtungen kann eine zweidimensionale Auflösung der Kraft erfolgen, bei Anregbarkeit von solchen Schwingungsmoden für drei linear unabhängige Richtungen eine dreidimensionale Auflösung. D.h. es kann ein multiaxialer Kraftsensor realisiert werden.

Weiters sei bemerkt, dass sich die gemessene Kraft auch aus einem auf den Rahmen wirkenden Drehmoment ergeben kann, welches zu einer Torsion des Rahmens und entsprechenden Verschiebungen der Aufhängungsbereiche führen kann. Entsprechend kann der erfindungsgemäße Kraftsensor also grundsätzlich auch zur Messung von Drehmomenten bzw. Torsionen verwendet werden.

Schließlich sei bemerkt, dass im Falle von mehreren Leitmitteln in Form von Leiterbahnen nicht zwangsweise alle Leiterbahnen gleichzeitig für die Anregung von Schwingungen verwendet bzw. gleichzeitig mit Wechselspannung beaufschlagt

werden müssen. Beispielsweise kann eine der Leiterbahnen zur Temperaturmessung verwendet werden, indem diese Leiterbahn nicht mit Wechselspannung beaufschlagt wird, sondern der elektrische Widerstand dieser Leiterbahn gemessen wird. Zusätzlich oder alternativ können für die Temperaturmessung aber auch eine oder mehrere zusätzliche Leiterbahnen, insbesondere aus Platin, vorgesehen sein, deren elektrischer Widerstand zur Bestimmung der Temperatur gemessen wird. Diese zusätzlichen Leiterbahnen können dabei zumindest abschnittsweise über die Schwingstruktur, insbesondere zumindest abschnittsweise über zumindest einen der Arme der Schwingstruktur, verlaufen und/oder in zumindest einem der Aufhängungsbereiche.

Hinsichtlich der Montage des erfindungsgemäßen Kraftsensors an einem Objekt, das zu bestimmenden Krafteinwirkungen ausgesetzt ist, ist festzuhalten, dass unterschiedlichste Befestigungsmöglichkeiten existieren, die an dieser Stelle nicht abschließend aufgezählt werden können. Typischerweise ist der erfindungsgemäße Kraftsensor dabei fix mit dem Objekt verbunden und, wenn keine Krafteinwirkung vorliegt, eben angeordnet. Beispielsweise kann der erfindungsgemäße Kraftsensor bei der Überwachung eines spezifischen Bauteils in die Oberfläche des Bauteils, d.h. in eine dafür vorgesehene Ausnehmung des Bauteils, eingebracht und dann vergossen werden (natürlich ohne dabei die Schwingstruktur zu verkleben). Ein weiteres, spezielleres Anwendungsbeispiel wäre der Einsatz des erfindungsgemäßen Kraftsensors als Ersatz und/oder Erweiterung einer Kraftmessdose, wo die Kraft von außen aufgebracht wird. Hierbei wäre es auch denkbar, den Kraftsensor nur einseitig (aufgestellt) zu montieren.

Um eine gegenüber äußeren Einflüssen besonders stabile Schwingung der Schwingstruktur zu ermöglichen, ist es bei einer bevorzugten Ausführungsform des erfindungsgemäßen

Kraftsensors vorgesehen, dass die Aufhängungsbereiche im Bereich von Ecken des Rahmens angeordnet sind.

Um eine herstellungstechnisch einfache Lösung zu ermöglichen, ist es bei einer bevorzugten Ausführungsform des erfindungsgemäßen Kraftsensors vorgesehen, dass vier Ecken des Rahmens vorgesehen sind, die in einer Ebene des Rahmens angeordnet sind und bevorzugt ein Rechteck, besonders bevorzugt ein Quadrat, in der Ebene ausbilden.

Typischerweise ist die Erstreckung des Rahmens in einer normal auf die Ebene des Rahmens stehenden Normalrichtung deutlich geringer als in der Ebene. Beispielsweise kann der Rahmen in der Ebene von 1 mm * 1 mm bis 15 mm * 15 mm groß sein und in der Normalrichtung z.B. von 100 µm bis 500 µm, vorzugsweise 250 µm. Die Schwingstruktur kann in Normalrichtung eine nochmals reduzierte Größe aufweisen, z.B. von 10 µm bis 50 µm, vorzugsweise 20 µm.

Um die Sensitivität des Kraftsensors zu besonders kleinen Kräften hin zu erweitern, ist es bei einer bevorzugten Ausführungsform des erfindungsgemäßen Kraftsensors vorgesehen, dass der Rahmen mindestens einen mäanderförmigen Abschnitt aufweist, der vorzugsweise zwischen zumindest zwei Aufhängungsbereichen angeordnet ist. Die Mäanderstruktur bewirkt dabei - ähnlich einer Spiralfeder - eine elastische Verformbarkeit des entsprechenden Abschnitts des Rahmens entlang zumindest einer Richtung bei verringerter Krafteinwirkung im Vergleich zur notwendigen Krafteinwirkung für dieselbe Verformung ohne Mäanderstruktur.

D.h. es wird eine Verformbarkeit des Rahmens schon bei sehr kleinen Kräften ermöglicht. Vorzugsweise sind dabei die zumindest zwei Aufhängungsbereiche durch einen Abschnitt des Rahmens miteinander verbunden, der den mäanderförmigen Abschnitt enthält.

Vorzugsweise weist jede Seite des Rahmens einen solchen mäanderförmigen Abschnitt auf und/oder ist entlang des Umfangs des Rahmens jeweils zwischen zwei aufeinanderfolgenden Aufhängungsabschnitten ein mäanderförmiger Abschnitt vorgesehen um eine erhöhte Kraftempfindlichkeit in zumindest zwei Dimensionen, d.h. für Kräfte in sämtlichen Richtungen innerhalb der Ebene des Rahmens, zu erzielen.

Umgekehrt kann auch bewusst kein mäanderförmiger Abschnitt im Rahmen vorgesehen sein, um analog zum oben Gesagten gezielt den Messbereich zu höheren Kräften zu verschieben.

Um zu gewährleisten, dass die Schwingstruktur Schwingungsmoden in unterschiedlichsten Richtungen aufweist, die in weiterer Folge angeregt werden können, ist es bei einer bevorzugten Ausführungsform des erfindungsgemäßen Kraftsensors vorgesehen, dass die Anzahl der Arme ein ganzzahliges Vielfaches von vier, vorzugsweise genau vier, ist. Letztere Anzahl stellt gewissermaßen das Optimum dar zwischen den möglichen anzuregenden Schwingungsmoden, einer exakten Aufspaltung der zu messenden Belastung in x- und y-Richtung (bzw. in zwei zueinander rechtwinkeligen Richtungen, insbesondere in der Ebene des Rahmens) sowie den auftretenden Momenten zueinander. Zudem wird bei mehr als vier Armen das System wieder komplizierter in Hinblick auf die möglichen Schwingungen sowie die Temperaturabhängigkeit.

Bei einer bevorzugten Ausführungsform des erfindungsgemäßen Kraftsensors ist vorgesehen, dass die Schwingstruktur ein Kopplungselement aufweist, durch das die Arme miteinander mechanisch gekoppelt sind, wobei jeder Arm vorzugsweise mit einem Ende am Kopplungselement fixiert ist. Durch geeignete Wahl bzw. strukturelle Gestaltung des Kopplungselements können die Schwingungsmoden der Schwingstruktur gezielt gestaltet werden, um z.B. ein besonders stabiles Schwingungsverhalten, insbesondere in bevorzugten Richtungen, zu erzielen.

Im einfachsten Fall könnte das Kopplungselement auch einfach im Wesentlichen punktförmig sein, wenn sich also die Arme in diesem Punkt treffen und insbesondere von diesem Punkt sternförmig abstehen. Bei vier geradlinigen Armen ergibt sich dann eine einfache Kreuz- oder X-Form.

Bei einer bevorzugten Ausführungsform des erfindungsgemäßen Kraftsensors ist vorgesehen, dass das Kopplungselement eine Fläche umrandet, die vorzugsweise in einer Ebene des Rahmens liegt. Es zeigt sich, dass durch diese Gestaltung sehr stabile Schwingungsmoden erzielt werden können.

Das Kopplungselement muss dabei nicht eckig bzw. vieleckig sein, sondern kann auch rund oder zumindest abschnittsweise rund sein.

Bei einer herstellungstechnisch besonders einfachen Ausführungsform des erfindungsgemäßen Kraftsensors ist vorgesehen, dass das Kopplungselement vieleckig ist, vorzugsweise viereckig, bevorzugt rechteckig, besonders bevorzugt quadratisch.

Bei einer besonders bevorzugten Ausführungsform des erfindungsgemäßen Kraftsensors ist vorgesehen, dass jeder Arm im Bereich eines Eckpunkts des Kopplungselements an diesem fixiert ist.

Vorzugsweise ist dabei jeder Arm mit einem Ende am Kopplungselement fixiert.

Es zeigt sich, dass diese Anordnung besonders stabile Schwingungsmoden garantiert, die insbesondere Normalmoden ausbilden können.

Um ein Wölben der Arme und - damit eine Verstimmung der Resonanzfrequenz - aufgrund einer thermisch bedingten Ausdehnung oder Kontraktion zu unterbinden, ist es bei einer bevorzugten Ausführungsform des erfindungsgemäßen Kraftsensors

vorgesehen, dass die Arme jeweils mittels einer zumindest abschnittsweise mäanderförmigen Temperaturausgleichsstruktur am jeweiligen Aufhängungsbereich fixiert sind. Die jeweilige Temperaturausgleichsstruktur kann dabei durch einen Kragarm ausgebildet sein. Die derart ausgeführten, am Rahmen fixierten Temperaturausgleichsstrukturen unterliegen selbst einer thermischen Ausdehnung bzw. Kontraktion und sind so zu den Armen angeordnet, dass die thermische Ausdehnung der Arme kompensiert wird, wodurch ein Wölben verhindert wird.

Vorzugsweise sind die Temperaturausgleichsstrukturen jeweils einstückig mit dem zugehörigen Arm ausgeführt.

Um Kraftsensoren mit einer wohldefinierten Struktur und wohldefinierten mechanischen Eigenschaften des Rahmens sowie der Schwingstruktur herstellen zu können, ist es bei einer bevorzugten Ausführungsform des erfindungsgemäßen Kraftsensors vorgesehen, dass der Rahmen und die Schwingstruktur einstückig aus, vorzugsweise einkristallinem, Silizium gefertigt sind. Dies ermöglicht beispielsweise die Herstellung auf Basis eines Silizium-Wafers in einem sogenannten, an sich bekannten Silicon-On-Insulator (SOI)-Verfahren.

Um die (Resonanz-)Schwingungen der Schwingstruktur, insbesondere die Frequenzen der (Resonanz-)Schwingungen, zu bestimmen, können an sich bekannte Auslesemittel verwendet werden. Entsprechend ist erfindungsgemäß ein System umfassend einen erfindungsgemäßen Kraftsensor sowie Auslesemittel zur Bestimmung der Resonanzfrequenz vorgesehen, wobei die Auslesemittel vorzugsweise mindestens einen optischen Sensor und/oder mindestens einen kapazitiven Sensor umfassen. Derlei Sensoren sind, wie gesagt, an sich bekannt.

Kapazitive Sensoren sind insbesondere zur Messung von Schwingungsmoden, deren Schwingungsebene bzw. Amplitude normal zur Ebene des Rahmens steht, geeignet, wobei die kapazitiven Sensoren dann über und/oder unter der Ebene des Rahmens

angeordnet sein können. Mit optischen Sensoren können insbesondere Schwingungsmoden, deren Schwingungsebene bzw. Amplitude in der Ebene des Rahmens liegt, gemessen werden. Z.B. kann eine optische Messung in Transmissionsgeometrie (normal auf die Ebene des Rahmens) erfolgen und kann so die periodische Änderung der Anordnung bzw. Geometrie der Schwingstruktur in der Ebene des Rahmens detektiert werden.

Bei einer bevorzugten Ausführungsform des erfindungsgemäßen Systems ist vorgesehen, dass eine Steuereinheit vorgesehen ist, mit der das mindestens eine Leitmittel mit Wechselspannung beaufschlagbar ist, um die Schwingstruktur zum Schwingen anzuregen, und wobei die Steuereinheit mit den Auslesemitteln zur Bestimmung der Resonanzfrequenz verbunden ist, wobei vorzugsweise mindestens zwei Leitmittel vorgesehen sind und die Steuereinheit zur Beaufschlagung der mindestens zwei Leitmittel mit gegenphasigen Wechselspannungen ausgelegt ist. Die Steuereinheit kann somit - insbesondere nacheinander - Wechselspannungen unterschiedlicher Frequenzen zur Beaufschlagung verwenden und kann auf Basis der Detektion der jeweils resultierenden Schwingung der Schwingstruktur mindestens eine Resonanzfrequenz bestimmen, wobei die Wahl der nächsten Frequenz vom aktuellen Detektionsergebnis abhängig gemacht werden kann.

Die Beaufschlagung mit gegenphasiger Wechselspannung kann messtechnische Vorteile haben, insbesondere wenn neben der Frequenz auch die Amplitude bestimmt werden soll, da sich hierdurch sehr leicht und ohne zusätzlichen Rechenaufwand ein Differenzsignal der Auslesemittel, mit deren Hilfe die Amplituden der Schwingungsmoden gemessen werden, generieren lässt. Beispielsweise wäre die Realisierung eines Differentialkondensators bei einer kapazitiven Auslese der Amplituden möglich.

Um besonders rasch zumindest eine Resonanzfrequenz bestimmen zu können, ist es bei einer bevorzugten Ausführungsform des erfindungsgemäßen Systems vorgesehen, dass die Steuereinheit zur Beaufschlagung des mindestens einen Leitmittels mit mindestens einem Puls von Wechselspannungen ausgelegt ist, um die Schwingstruktur zum Schwingen anzuregen, wobei der mindestens eine Puls eine Bandbreite von Frequenzen aufweist, welche Bandbreite die Resonanzfrequenz mindestens einer Schwingungsmode der Schwingstruktur, vorzugsweise in einem unbelasteten Zustand des Kraftsensors, umfasst. Das oben geschilderte, sequentielle Beaufschlagen mit Wechselspannungen unterschiedlicher Frequenzen, ist demgegenüber deutlich zeitaufwändiger. Insbesondere ausgehend von der Kenntnis mindestens einer Resonanzfrequenz im unbelasteten Zustand (d.h. ohne Krafteinwirkung auf den Sensor) kann ein geeignetes bzw. hinreichend großes Frequenzband gewählt werden, um die aufgrund der Krafteinwirkung verstimmte Resonanzfrequenz zu ermitteln.

In der Praxis wäre z.B. die Verwendung eines Scanners, insbesondere Handscanners, denkbar, der in die Nähe des Kraftsensors gebracht wird und die Beaufschlagung des mindestens einen Leitmittels mit dem mindestens einen Puls (insbesondere induktiv) bewirkt. In den Handscanner können darüber hinaus die Auslesemittel sowie die Steuereinheit integriert sein. Entsprechend kann der Kraftsensor an einem Objekt montiert bleiben, bei welchem man mögliche Krafteinwirkungen auf dieses nur von Zeit zu Zeit (und nicht laufend) bestimmen möchte. Bei einem solchen Objekt kann es sich z.B. um ein Bauwerk oder eine von einem Menschen getragene Prothese handeln.

Grundsätzlich ist es dabei möglich, auch mehrere Resonanzfrequenzen für unterschiedliche Moden mit einem Puls anzuregen.

Um gezielt unterschiedliche Resonanzfrequenzen anzuregen, z.B. um Richtungsabhängigkeiten der entsprechenden Schwingungsmoden für eine richtungsaufgelöste Kraftmessung messtechnisch bequem auszunutzen, ist es bei einer besonders bevorzugten Ausführungsform des erfindungsgemäßen Systems vorgesehen, dass die Steuereinheit zur Beaufschlagung des mindestens einen Leitmittels mit mehreren Pulsen von Wechselspannungen nacheinander ausgelegt ist, wobei die unterschiedlichen Pulse Resonanzfrequenzen unterschiedlicher Schwingungsmoden der Schwingstruktur, vorzugsweise im unbelasteten Zustand des Kraftsensors, umfassen. D.h. ein erster Puls umfasst zumindest eine erste resonante Schwingungsmode der Schwingstruktur, vorzugsweise im unbelasteten Zustand; ein weiterer Puls umfasst zumindest eine weitere resonante Schwingungsmode der Schwingstruktur, vorzugsweise im unbelasteten Zustand, wobei die erste Schwingungsmode und die weitere Schwingungsmode unterschiedlich sind.

Bei einer bevorzugten Ausführungsform des erfindungsgemäßen Systems ist vorgesehen, dass das System Mittel zur Erzeugung des Magnetfelds umfasst, vorzugsweise mindestens einen Permanentmagnet und/oder mindestens eine Helmholtz-Spule. Auf diese Weise kann sichergestellt werden, dass stets ein zumindest einigermaßen definiertes Magnetfeld für die Kraftmessungen vorliegt, womit sich gewünschte Schwingungsmoden der Schwingstruktur sehr genau einstellen bzw. detektieren lassen, um sehr präzise Kraftmessungen zu ermöglichen.

Besonders exakt muss das Magnetfeld dabei nicht definiert sein, da es für die Anregung einer gewünschten Schwingungsmode der Schwingstruktur genügt, die entsprechende Resonanzfrequenz durch geeignete Wahl der Frequenz der Wechselspannung zu treffen. Die Mittel zur Erzeugung des Magnetfelds müssen daher auch nicht fix bzw. permanent am erfindungsgemäßen Kraftsensor befestigt bzw. angeordnet sein. Stattdessen können die Mittel

zur Erzeugung des Magnetfelds, insbesondere ein Permanentmagnet, im weiter oben bereits erwähnten Scanner, insbesondere Handscanner, angeordnet sein. Der Scanner dient dann nicht nur zur Beaufschlagung mit Wechselspannung, sondern stellt gleichzeitig auch das für die Schwingungsanregung mittels Lorentz-Kraft notwendige Magnetfeld zur Verfügung.

Auf die geschilderte Weise kann auch die Anregung von so genannten In-Plane-Schwingungen leicht gewährleistet werden, also von Schwingungsmoden, deren Schwingungsebene bzw. Amplitude in der Ebene des Rahmens liegt. Hierdurch lassen sich Torsionen des Rahmens bzw. an diesem anliegende Drehmomente besonders gut messen. Entsprechend ist es bei einer besonders bevorzugten Ausführungsform des erfindungsgemäßen Systems vorgesehen, dass die Steuereinheit zur Anregung von Schwingungen der Schwingstruktur in einer Ebene des Rahmens ausgelegt ist.

Wie bereits festgehalten, eignet sich der erfindungsgemäße Kraftsensor insbesondere für Anwendungen in der Biologie oder Medizin, z.B. an medizinischen Instrumenten, sowie in der Prothetik. Insbesondere der Komfort einer Prothese und die Vermeidung von Schäden am Körper hängen wesentlich von einer optimalen Kraftverteilung ab. Es ist denkbar, Prothesen und/oder Implantate mit erfindungsgemäßen Kraftsensoren auszustatten, um bei Verwendung der Prothesen bzw. Implantate Feedback über den jeweiligen Belastungszustand zu erhalten.

Entsprechend ist erfindungsgemäß eine Prothese umfassend einen erfindungsgemäßen Kraftsensor und/oder ein erfindungsgemäßes System vorgesehen.

KURZE BESCHREIBUNG DER FIGUREN

Die Erfindung wird nun anhand eines Ausführungsbeispiels näher erläutert. Die Zeichnungen sind beispielhaft und sollen den Erfindungsgedanken zwar darlegen, ihn aber keinesfalls einengen oder gar abschließend wiedergeben.

Dabei zeigt:

Fig. 1 einen erfindungsgemäßen Kraftsensor in Aufsicht

Fig. 2 eine vergrößerte Ansicht des Details A aus Fig. 1

Fig. 3 ein schematisches Blockschaltbild eines erfindungsgemäßen Systems mit dem Kraftsensor der Fig. 1

WEGE ZUR AUSFÜHRUNG DER ERFINDUNG

Fig. 1 zeit einen erfindungsgemäßen Kraftsensor 1 in Aufsicht, der zur Messung sehr kleiner Kräfte von kleiner gleich 1 µN, vorzugsweise von kleiner gleich 1nN, geeignet ist. Der Kraftsensor 1 weist einen Rahmen 2 mit vier Ecken 10a, 10b, 10c, 10d auf, die in einer Ebene des Rahmens 2 liegen, wobei in Fig. 1 die Ebene des Rahmens 2 mit der Zeicheneben zusammenfällt. Im dargestellten Ausführungsbeispiel markieren die Ecken 10a-d Eckpunkte eines Quadrats mit einer Seitenlänge von typischerweise 2 mm. Es sei jedoch betont, dass prinzipiell auch andere Formen, insbesondere eine Rechteckform, des Rahmens 2 möglich wären.

Der Kraftsensor 1 weist weiters eine Schwingstruktur 4 auf, die im Rahmen 2 frei schwingen kann. Hierzu weist die Schwingstruktur 4 im dargestellten Ausführungsbeispiel vier Arme 3a, 3b, 3c und 3d auf, mit denen die Schwingstruktur 4 am Rahmen 2 befestigt ist, wobei jeder der Arme 3a-d mit einem Ende in einem zugehörigen Aufhängungsbereich 6a, 6b, 6c, 6d

des Rahmens 2 fixiert ist. Die Aufhängungsbereiche 6a-d sind jeweils im Bereich einer der Ecken 10a-d des Rahmens 2 angeordnet.

Die Arme 3a-d weisen weiters jeweils ein Ende auf, das an einem Kopplungselement 9 der Schwingstruktur 4 fixiert ist. Das Kopplungselement 9 wiederum ist im dargestellten Ausführungsbeispiel mittig innerhalb des Rahmens 2 angeordnet und im Wesentlichen rechteckförmig ausgebildet, wobei jeder der Arme 3a-d im Bereich eines Eckpunkts des Kopplungselements 9 in dieses mündet.

Im dargestellten Ausführungsbeispiel erstreckt sich jeder der Arme 3a-d mit einem im Wesentlichen geradlinigen Abschnitt zwischen dem zugehörigen Aufhängungsbereich 6a-d und dem zugehörigen Eckpunkt des Kopplungselements 9. Hierdurch ergibt sich eine Anordnung der Arme 3a-d, die einer X-Form ähnelt, sodass jeder der Arme 3a-d zumindest abschnittsweise quer zu zwei anderen der Arme 3a-d verläuft (die besagten geradlinigen Abschnitte der Arme 3a und 3c verlaufen parallel zueinander und quer zu den entsprechenden geradlinigen Abschnitten der Arme 3b und 3d und vice versa).

Auf den Armen 3a-d sind im dargestellten Ausführungsbeispiel Leitmittel in Form von Leiterbahnen 5a, 5b, 5c, 5d, vorzugsweise aus Platin, angeordnet. Jede der Leiterbahnen 5a-d erstreckt sich entlang von jeweils zwei der Arme 3a-d, um einen Stromfluss in Form von bewegten Ladungsträgern, insbesondere Elektronen, zwischen den Aufhängungsbereichen 6a-d der jeweiligen zwei Arme 3a-d zu ermöglichen. Konkret erstreckt sich im dargestellten Ausführungsbeispiel die Leiterbahn 5a entlang der Arme 3a und 3b zwischen den Aufhängungsbereichen 6a und 6b, die Leiterbahn 5b entlang der Arme 3b und 3c zwischen den Aufhängungsbereichen 6b und 6c, die Leiterbahn 5c entlang der Arme 3c und 3d zwischen den Aufhängungsbereichen 6c und 6d und die Leiterbahn 5d entlang

der Arme 3d und 3a zwischen den Aufhängungsbereichen 6d und 6a.

Um die Leiterbahnen 5a-d einfach mit einer Wechselspannung beaufschlagen zu können, sind in den Aufhängungsbereichen 6a-d kreisförmige Kontaktstellen 13a, 13a', 13b, 13b', 13c, 13c', 13d, 13d' vorgesehen. Diese sind so groß ausgeführt, dass eine Kontaktierung mit einer Wechselspannungsquelle bzw. mit Leitern einer solchen (nicht dargestellt) zur Wechselspannungsbeaufschlagung von zumindest einer der Leiterbahnen 5a-d bequem möglich ist. Konkret verläuft die Leiterbahn 5a zwischen den Kontaktstellen 13a' und 13b, die Leiterbahn 5b zwischen den Kontaktstellen 13b' und 13c, die Leiterbahn 5c zwischen den Kontaktstellen 13c' und 13d und die Leiterbahn 5d zwischen den Kontaktstellen 13d' und 13a.

Zur besseren Verdeutlichung der Leiterbahnen 5a-d zeigt Fig. 2 eine vergrößerte Ansicht des Details A aus Fig. 1, in welcher die Leiterbahnen 5a und 5d klar erkennbar sind. Weiters ist in Fig. 2 ein durch die Leiterbahn 5a fließender Wechselstrom i mit einem Pfeil symbolisiert. Wenn der Kraftsensor 1 in diesem Fall in einem Magnetfeld mit einer Flussdichte B angeordnet ist, die im dargestellten Ausführungsbeispiel im gesamten Bereich des Kraftsensors 1 als gleichförmig mit einem in den Fig. 1 und Fig. 2 von links nach rechts weisenden Vektor angenommen ist, so resultiert eine normal auf die Zeichenebene stehende und in diese weisende Lorentz-Kraft F_L, die in Fig. 2 schematisch eingezeichnet ist. Wechselt der Wechselstrom sein Vorzeichen bzw. seine Richtung, so weist auch die Lorentz-Kraft F_L in die entgegengesetzte Richtung (also aus der Zeichenebene heraus). Die Lorentz-Kraft wirkt auf die Ladungsträger in der Leiterbahn 5a und damit auf die Leiterbahn 5a selbst bzw. auf die Arme 3a, 3b und regt durch den ständigen Vorzeichenwechsel die Arme 3a, 3b und damit die gesamte Schwingstruktur 4 zum Schwingen im Rahmen 2 an. Eine besonders effiziente Anregung erfolgt dann, wenn der

Wechselstrom i eine Resonanzfrequenz aufweist, also die Frequenz einer resonanten Schwingungsmode der Schwingstruktur 4.

Es sei bemerkt, dass nicht alle Leiterbahnen 5a-d zwangsweise gleichzeitig für die Anregung von Schwingungen der Schwingstruktur 4 verwendet bzw. gleichzeitig mit Wechselspannung beaufschlagt werden müssen. In Fig. 2 könnte z.B. die Leiterbahn 5d bewusst nicht mit Wechselspannung beaufschlagt werden, sodass durch die Leiterbahn 5d kein Wechselstrom i fließt (sondern in Fig. 2 nur durch die Leiterbahn 5a). Die Leiterbahn 5d kann dann beispielsweise zur Temperaturmessung verwendet werden, indem der elektrischer Widerstand der Leiterbahn 5d gemessen wird, wobei bei dieser Messung die Kontaktstellen 13d‘ und 13a zur Kontaktierung verwendet werden können.

Die Resonanzfrequenz der Schwingstruktur 4 hängt insbesondere von der relativen Position der Aufhängungsbereiche 6a-d zueinander ab. Eine Änderung bewirkt ein Verspannen der Schwingstruktur 4, insbesondere der Arme 3a-d, was eine entsprechende Änderung der Resonanzfrequenz zur Folge hat. Um diesen Effekt zur Kraftmessung optimal ausnutzen zu können, ist der Kraftsensor 1 so ausgelegt, dass sich die Aufhängungsbereiche 6a-d zumindest teilweise räumlich relativ zueinander verschieben, wenn der Rahmen 2 mit einer Kraft 7 beaufschlagt wird, dass die Größe der räumlichen Verschiebung 8 der Aufhängungsbereiche 6a-d von der Größe der Kraft 7 abhängt, dass die räumliche Verschiebung 8 der Aufhängungsbereiche 6a-d eine Verstimmung der Resonanzfrequenz bewirkt und dass die Größe der Verstimmung von der Größe der räumlichen Verschiebung 8 der Aufhängungsbereiche 6a-d abhängt.

Indem die Resonanzfrequenz der Schwingstruktur 4 in einem unbelasteten Zustand des Kraftsensors 1, also ohne

Krafteinwirkung, bekannt ist oder bestimmt wird, und dann die Resonanzfrequenz im belasteten Zustand, also bei Einwirkung der Kraft 7 auf den Kraftsensor 1 bzw. den Rahmen 2, kann auf die Größe der Kraft 7 rückgerechnet werden. Ebenso ist es ausgehend von einem belasteten Zustand und Kenntnis bzw. Bestimmung der Resonanzfrequenz in diesem belasteten Zustand möglich, durch Bestimmung der Resonanzfrequenz in einem weiteren belasteten Zustand mit einer anderen Kraft 7 die entsprechende Kraftänderung (vom belasteten Zustand zum weiteren belasteten Zustand) zu ermitteln.

Besonders gut lassen sich Kräfte 7 messen, die zumindest eine Komponente innerhalb der Ebene des Rahmens 2 haben. In Fig. 1 liegt die eingezeichnete Kraft 7 vollständig in der Ebene des Rahmens 2. Dabei wird gegen den Rahmen 2 im Bereich der Aufhängungsbereiche 6b, 6c von oben nach unten gedrückt und im Bereich der Aufhängungsbereiche 6d, 6a von unten nach oben. In diesem Beispiel werden die Aufhängungsbereiche 6b, 6c einerseits und die Aufhängungsbereiche 6d, 6a andererseits um die Verschiebung 8 aufeinander zu verschoben. Die relative Position der Aufhängungsbereiche 6d und 6a zueinander ändert sich hierbei nicht, ebenso wie die relative Position der Aufhängungsbereiche 6b und 6c zueinander.

Damit auch bei sehr kleinen Kräften 7 die Verschiebung 8 hinreichend groß ist, weist der Rahmen 2 mäanderförmige Abschnitte 11a, 11b, 11c, 11d auf, die jeweils zwischen zwei der Aufhängungsbereiche 6a-d angeordnet sind und eine elastische Verformbarkeit des Rahmens 2 in einer Richtung parallel zu einer Verbindungslinie zwischen diesen zwei der Aufhängungsbereiche 6a-d begünstigt. Im dargestellten Ausführungsbeispiel werden durch die Kraft 7 die mäanderförmigen Abschnitte 11a und 11c verformt, was zur Verschiebung 8 führt.

Um zu verhindern, dass es aufgrund von Temperaturänderungen zu thermisch bedingten Wölbungen bzw. Verspannungen durch Ausdehnung oder Kontraktion der Arme 3a-d kommt, die eine Änderung der Resonanzfrequenz der Schwingstruktur 4 nach sich ziehen würden, sind im dargestellten Ausführungsbeispiel Temperaturausgleichsstrukturen 12a, 12b, 12c, 12d vorgesehen. Jeder der Arme 3a-d ist mittels einer der Temperaturausgleichsstrukturen 12a-d am Rahmen befestigt. Die Temperaturausgleichsstrukturen 12a-d sind mäanderförmig ausgeführt. Eine Temperaturänderung hat eine Ausdehnung bzw. Kontraktion der Temperaturausgleichsstrukturen 12a-d zur Folge, die die thermische Ausdehnung bzw. Kontraktion des zugehörigen Arms 3a-d genau kompensieren, sodass es zu keiner Verstimmung kommt.

Hierbei verlaufen die Leiterbahnen 5a-d entlang der Temperaturausgleichsstrukturen 12a-d, also ebenfalls zumindest abschnittsweise mäanderförmig.

Rahmen 2 und Schwingstruktur 4 des Kraftsensors 1 sind im dargestellten Ausführungsbeispiel mittels der an sich bekannten Silicon-On-Insulator-Technologie hergestellt. Bei dieser Herstellungsmethode kann der Rahmen 2 gemeinsam mit der Schwingstruktur 4 einstückig in einem Herstellungsrahmen erzeugt werden, wobei nach der Fertigstellung der Rahmen 2 bzw. der Kraftsensor 1 aus dem Herstellungsrahmen an dafür vorgesehenen Sollbruchstellen herausgebrochen wird.

Um die (Resonanz-)Schwingungen der Schwingstruktur 4, insbesondere die Frequenzen der (Resonanz-)Schwingungen, zu bestimmen, können an sich bekannte Auslesemittel verwendet werden, insbesondere optische Sensoren 15 und/oder kapazitive Sensoren (nicht dargestellt). Kapazitive Sensoren sind insbesondere zur Messung von Schwingungsmoden, deren Schwingungsebene bzw. Amplitude normal zur Ebene des Rahmens 2 steht, geeignet, wobei die kapazitiven Sensoren dann über

und/oder unter der Ebene angeordnet sein können. Mit optischen Sensoren 15 können insbesondere Schwingungsmoden, deren Schwingungsebene bzw. Amplitude in der Ebene des Rahmens 2 liegt, gemessen werden. Z.B. kann eine optische Messung in Transmissionsgeometrie (quer, insbesondere normal auf die Ebene des Rahmens 2; der mindestens eine optische Sensor 15 ist dann über und/oder unter der Ebene des Rahmens 2 angeordnet) erfolgen und kann so die periodische Änderung der Anordnung bzw. Geometrie der Schwingstruktur 4 in der Ebene des Rahmens 2 detektiert werden.

Fig. 3 zeigt eine schematische Darstellung eines erfindungsgemäßen Systems 14, das den Kraftsensor 1 sowie mindestens einen optischen Sensor 15 umfasst. Die punktierte Linie zwischen dem mindestens einen optischen Sensor 15 und dem Kraftsensor 1 deutet in Fig. 3 an, dass mittels des mindestens einen optischen Sensors 15 die Schwingungen, insbesondere die Frequenz der Schwingstruktur 4 des Kraftsensors 1 detektiert werden. Der optische Sensor 15 ist dabei mit einer Steuereinheit 16 des Systems 14 verbunden, um die bzw. zumindest eine Resonanzfrequenz der Schwingstruktur 4 bestimmen zu können. Weiters ist die Steuereinheit 16 mit dem Kraftsensor 1 bzw. mit mindestens einer der Leiterbahnen 5a-d (insbesondere über die entsprechenden Kontaktstellen 13a-d') verbunden, um mindestens eine der Leiterbahnen 5a-d mit Wechselspannung beaufschlagen und die Schwingstruktur 4 zum Schwingen anregen zu können.

In der Praxis kann dies auch so realisiert sein, dass die Steuereinheit 16 eine separate Wechselspannungsquelle ansteuert, die wiederum mit dem Kraftsensor 1 bzw. mit mindestens einer der Leiterbahnen 5a-d verbunden ist. In diesem Fall handelt es sich also um eine indirekte Verbindung der Steuereinheit 16 mit dem Kraftsensor 1 bzw. wird die mindestens eine der Leiterbahnen 5a-d indirekt mittels der Steuereinheit 16 mit Wechselspannung beaufschlagt.

Die Steuereinheit 16 kann somit - insbesondere nacheinander - Wechselspannungen unterschiedlicher Frequenzen zur Beaufschlagung verwenden und kann auf Basis der Detektion der jeweils resultierenden Schwingung der Schwingstruktur 4 mindestens eine Resonanzfrequenz bestimmen, wobei die Wahl der nächsten Frequenz vom aktuellen Detektionsergebnis abhängig gemacht werden kann.

Vorzugsweise werden zur Anregung einer Schwingungsmode der Schwingstruktur 4 zwei der Leiterbahnen 5a-d mit gegenphasiger Wechselspannung mittels der Steuereinheit 16 beaufschlagt, wobei diese zwei Leiterbahnen vorzugsweise einander gegenüber liegen, z.B. die Leiterbahnen 5a und 5c.

Um besonders rasch zumindest eine Resonanzfrequenz bestimmen zu können, kann die Steuereinheit 16 zur Beaufschlagung der mindestens einen der Leiterbahnen 5a-d mit mindestens einem Puls von Wechselspannungen ausgelegt sein, um die Schwingstruktur 4 zum Schwingen anzuregen, wobei der mindestens eine Puls eine Bandbreite von Frequenzen aufweist, welche Bandbreite die Resonanzfrequenz mindestens einer Schwingungsmode der Schwingstruktur 4, vorzugsweise in einem unbelasteten Zustand des Kraftsensors 1, umfasst. Das oben geschilderte, sequentielle Beaufschlagen mit Wechselspannungen unterschiedlicher Frequenzen, ist demgegenüber deutlich zeitaufwändiger. Insbesondere ausgehend von der Kenntnis mindestens einer Resonanzfrequenz im unbelasteten Zustand (d.h. ohne Krafteinwirkung auf den Kraftsensor 1) kann ein geeignetes bzw. hinreichend großes Frequenzband gewählt werden, um die aufgrund der Krafteinwirkung verstimmte Resonanzfrequenz zu ermitteln.

Um gezielt unterschiedliche Resonanzfrequenzen anzuregen, z.B. um Richtungsabhängigkeiten der entsprechenden Schwingungsmoden für eine richtungsaufgelöste Kraftmessung messtechnisch bequem auszunutzen, kann die Steuereinheit 16 zur Beaufschlagung der

mindestens einen der Leiterbahnen 5a-d mit mehreren Pulsen von Wechselspannungen nacheinander ausgelegt sein, wobei die unterschiedlichen Pulse Resonanzfrequenzen unterschiedlicher Schwingungsmoden der Schwingstruktur 4, vorzugsweise im unbelasteten Zustand des Kraftsensors 1, umfassen. D.h. ein erster Puls umfasst zumindest eine erste resonante Schwingungsmode der Schwingstruktur 4, vorzugsweise im unbelasteten Zustand; ein weiterer Puls umfasst zumindest eine weitere resonante Schwingungsmode der Schwingstruktur 4, vorzugsweise im unbelasteten Zustand, wobei die erste Schwingungsmode und die weitere Schwingungsmode unterschiedlich sind.

Um ein wohldefiniertes Magnetfeld zur Verfügung zu stellen, umfasst das System 14 Mittel 17 zur Erzeugung des Magnetfelds. Diese können insbesondere mindestens einen Permanentmagnet und/oder mindestens eine Helmholtz-Spule beinhalten. Die strichlierte Linie in Fig. 3 deutet an, dass es denkbar ist, dass die Mittel 17 von der Steuereinheit 16 angesteuert werden, um ein gewünschtes Magnetfeld einzustellen. Beispielsweise könnte eine Helmholtz-Spule von der Steuereinheit 16 angesteuert werden.

Durch die Sicherstellung eines wohldefinierten Magnetfelds lassen sich gewünschte Schwingungsmoden der Schwingstruktur 4 sehr genau einstellen, was wiederum besonders präzise Kraftmessungen ermöglicht. Insbesondere kann auf diese Weise die Anregung von so genannten In-Plane-Schwingungen gewährleistet werden, also von Schwingungsmoden, deren Schwingungsebene bzw. Amplitude in der Ebene des Rahmens liegt. Es zeigt sich, dass solche In-Plane-Schwingungen eine besonders genaue Detektion von Torsionen des Rahmens 2 ermöglichen.

BEZUGSZEICHENLISTE

1	Kraftsensor
2	Rahmen
3a, 3b, 3c, 3d	Arm
4	Schwingstruktur
5a, 5b, 5c, 5d	Leiterbahn
6a, 6b, 6c, 6d	Aufhängungsbereich
7	Kraft
8	Räumliche Verschiebung der Aufhängungsbereiche
9	Kopplungselement
10a, 10b, 10c, 10d	Ecke des Rahmens
11a, 11b, 11c, 11d	Mäanderförmiger Abschnitt des Rahmens
12a, 12b, 12c, 12d	Temperaturausgleichsstruktur
13a, 13a', 13b, 13b', 13c, 13c', 13d, 13d'	Kontaktstelle
14	System
15	Optischer Sensor
16	Steuereinheit
17	Mittel zur Erzeugung eines Magnetfelds
B	Magnetische Flussdichte
F_L	Lorentz-Kraft
i	Wechselstrom

A N S P R Ü C H E

1. Kraftsensor (1) umfassend einen Rahmen (2) sowie eine Schwingstruktur (4), die mehrere Arme (3a-d) aufweist und im Rahmen (2) frei schwingen kann, wobei die Arme (3a-d) an Aufhängungsbereichen (6a-d) des Rahmens (2) fixiert sind und zumindest abschnittsweise quer zueinander verlaufen,
wobei mindestens ein Leitmittel (5a-d) vorgesehen ist, das sich entlang von zumindest zwei Armen (3a-b; 3b-c; 3c-d; 3d-a) erstreckt, um einen Stromfluss (i) in Form von bewegten Ladungsträgern zumindest zwischen zwei Aufhängungsbereichen (6a-b; 6b-c; 6c-d; 6d-a) zu ermöglichen,
wobei das mindestens eine Leitmittel (5a-d) mit einer Wechselspannung beaufschlagbar ist, um, insbesondere in einem unbelasteten Zustand des Kraftsensors (1), unter Ausnutzung der Lorentz-Kraft (F_L) mindestens eine Schwingungsmode der Schwingstruktur (4) mit einer Resonanzfrequenz anzuregen, wenn sich die Schwingstruktur (4) in einem Magnetfeld (B) befindet,
wobei der Kraftsensor (1) so ausgelegt ist, dass sich die Aufhängungsbereiche (6a-d) zumindest teilweise räumlich relativ zueinander verschieben, wenn der Rahmen (2) mit einer Kraft (7) beaufschlagt wird, dass die Größe der räumlichen Verschiebung (8) der Aufhängungsbereiche (6a-d) von der Größe der Kraft (7) abhängt, dass die räumliche Verschiebung (8) der Aufhängungsbereiche (6a-d) eine Verstimmung der Resonanzfrequenz bewirkt und dass die Größe der Verstimmung von der Größe der räumlichen Verschiebung (8) der Aufhängungsbereiche (6a-d) abhängt.

2. Kraftsensor (1) nach Anspruch 1, **dadurch gekennzeichnet, dass** die Aufhängungsbereiche (6a-d) im Bereich von Ecken (10a-d) des Rahmens (2) angeordnet sind.

3. Kraftsensor (1) nach einem der Ansprüche 1 bis 2, **dadurch gekennzeichnet, dass** vier Ecken (10a-d) des Rahmens (2) vorgesehen sind, die in einer Ebene des Rahmens (2) angeordnet sind und bevorzugt ein Rechteck, besonders bevorzugt ein Quadrat, in der Ebene ausbilden.

4. Kraftsensor (1) nach einem der Ansprüche 1 bis 3, **dadurch gekennzeichnet, dass** der Rahmen (2) mindestens einen mäanderförmigen Abschnitt (11a-d) aufweist, der vorzugsweise zwischen zumindest zwei Aufhängungsbereichen (6a-b; 6b-c; 6c-d; 6d-a) angeordnet ist

5. Kraftsensor (1) nach einem der Ansprüche 1 bis 4, **dadurch gekennzeichnet, dass** die Anzahl der Arme (3a-d) ein ganzzahliges Vielfaches von vier, vorzugsweise genau vier, ist.

6. Kraftsensor (1) nach einem der Ansprüche 1 bis 5, **dadurch gekennzeichnet, dass** die Schwingstruktur (4) ein Kopplungselement (9) aufweist, durch das die Arme (3a-d) miteinander mechanisch gekoppelt sind, wobei jeder Arm (3a-d) vorzugsweise mit einem Ende am Kopplungselement (9) fixiert ist.

7. Kraftsensor (1) nach Anspruch 6, **dadurch gekennzeichnet, dass** das Kopplungselement (9) eine Fläche umrandet, die vorzugsweise in einer Ebene des Rahmens (2) liegt.

8. Kraftsensor (1) nach Anspruch 7, **dadurch gekennzeichnet, dass** das Kopplungselement (9) vieleckig ist, vorzugsweise viereckig, bevorzugt rechteckig, besonders bevorzugt quadratisch.

9. Kraftsensor (1) nach Anspruch 8, **dadurch gekennzeichnet, dass** jeder Arm (3a-d) im Bereich eines Eckpunkts des Kopplungselements (9) an diesem fixiert ist.

10. Kraftsensor (1) nach einem der Ansprüche 1 bis 9, **dadurch gekennzeichnet, dass** die Arme (3a-d) jeweils mittels einer zumindest abschnittsweise mäanderförmigen Temperaturausgleichsstruktur (12a-d) am jeweiligen Aufhängungsbereich (6a-d) fixiert sind.

11. Kraftsensor (1) nach einem der Ansprüche 1 bis 10, **dadurch gekennzeichnet, dass** der Rahmen (2) und die Schwingstruktur (4) einstückig aus, vorzugsweise einkristallinem, Silizium gefertigt sind.

12. System (14) umfassend einen Kraftsensor (1) nach einem der Ansprüche 1 bis 11 sowie Auslesemittel zur Bestimmung der Resonanzfrequenz, wobei die Auslesemittel vorzugsweise mindestens einen optischen Sensor (15) und/oder mindestens einen kapazitiven Sensor umfassen.

13. System (14) nach Anspruch 12, **dadurch gekennzeichnet, dass** eine Steuereinheit (16) vorgesehen ist, mit der das mindestens eine Leitmittel (5a-d) mit Wechselspannung beaufschlagbar ist, um die Schwingstruktur (4) zum Schwingen anzuregen, und wobei die Steuereinheit (16) mit den Auslesemitteln (15) zur Bestimmung der Resonanzfrequenz verbunden ist, wobei vorzugsweise mindestens zwei Leitmittel (5a-d) vorgesehen sind und die Steuereinheit (16) zur Beaufschlagung der mindestens zwei Leitmittel (5a-d) mit gegenphasigen Wechselspannungen ausgelegt ist.

14. System (14) nach Anspruch 13, **dadurch gekennzeichnet, dass** die Steuereinheit (16) zur Beaufschlagung des mindestens einen Leitmittels (5a-d) mit mindestens einem Puls von Wechselspannungen ausgelegt ist, um die Schwingstruktur (4) zum Schwingen anzuregen, wobei der mindestens eine Puls eine Bandbreite von Frequenzen aufweist, welche Bandbreite die Resonanzfrequenz mindestens einer Schwingungsmode der Schwingstruktur (4),

vorzugsweise in einem unbelasteten Zustand des Kraftsensors (1), umfasst.

15. System (14) nach Anspruch 14, **dadurch gekennzeichnet, dass** die Steuereinheit zur Beaufschlagung des mindestens einen Leitmittels (5a-d) mit mehreren Pulsen von Wechselspannungen nacheinander ausgelegt ist, wobei die unterschiedlichen Pulse Resonanzfrequenzen unterschiedlicher Schwingungsmoden der Schwingstruktur (4), vorzugsweise im unbelasteten Zustand des Kraftsensors (1), umfassen.

16. System (14) nach einem der Ansprüche 12 bis 15, **dadurch gekennzeichnet, dass** das System Mittel (17) zur Erzeugung des Magnetfelds (B) umfasst, vorzugsweise mindestens einen Permanentmagnet und/oder mindestens eine Helmholtz-Spule.

17. System (14) nach einem der Ansprüche 13 bis 16, **dadurch gekennzeichnet, dass** die Steuereinheit (16) zur Anregung von Schwingungen der Schwingstruktur (4) in einer Ebene des Rahmens (2) ausgelegt ist.

18. Prothese umfassend einen Kraftsensor (1) nach einem der Ansprüche 1 bis 11 und/oder ein System (14) nach einem der Ansprüche 12 bis 17.

1/3

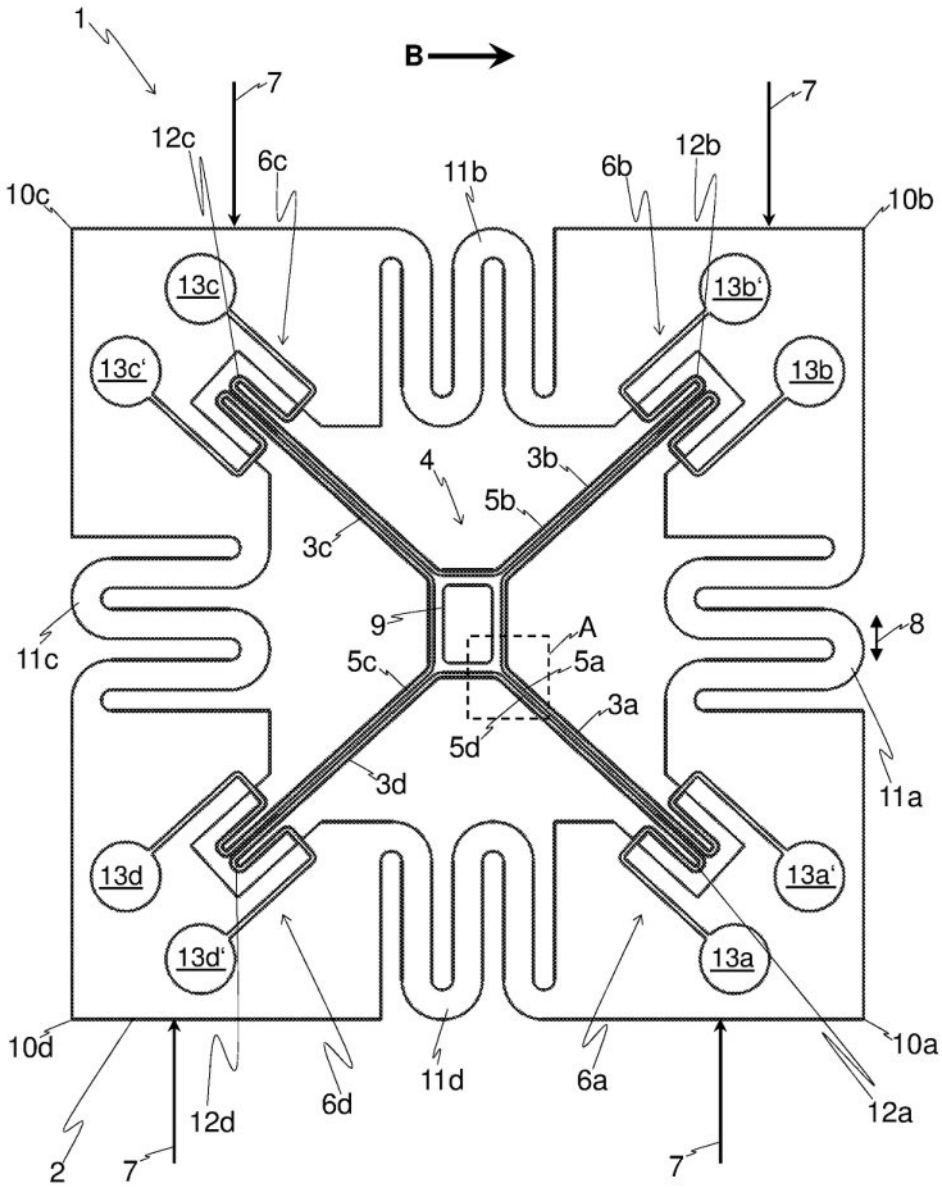

Fig. 1

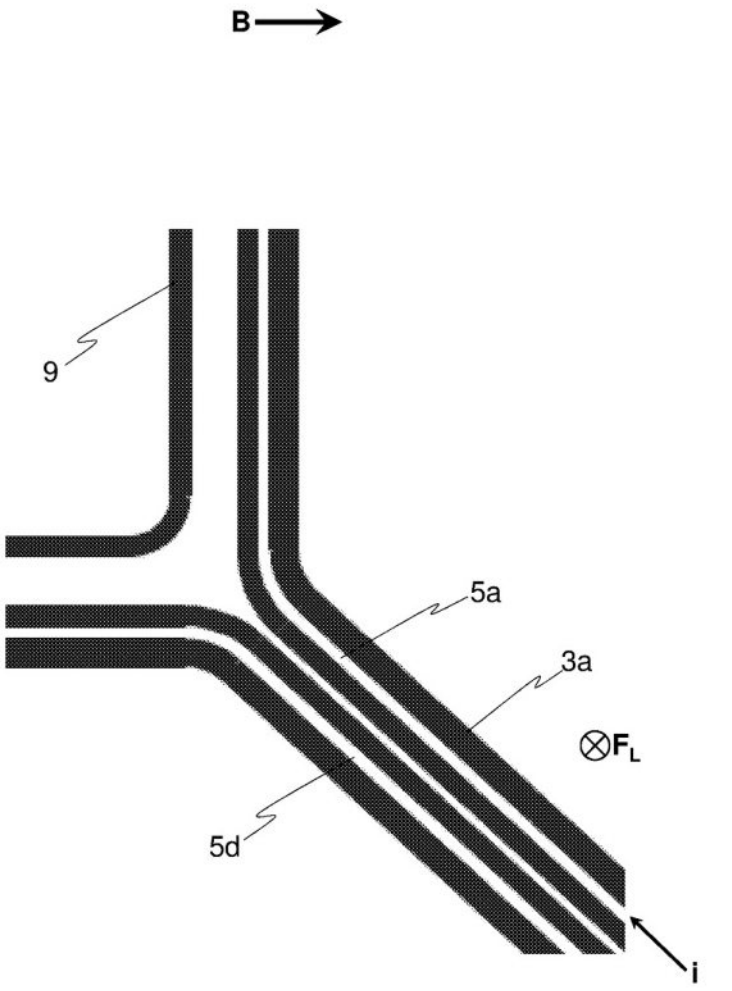

Fig. 2

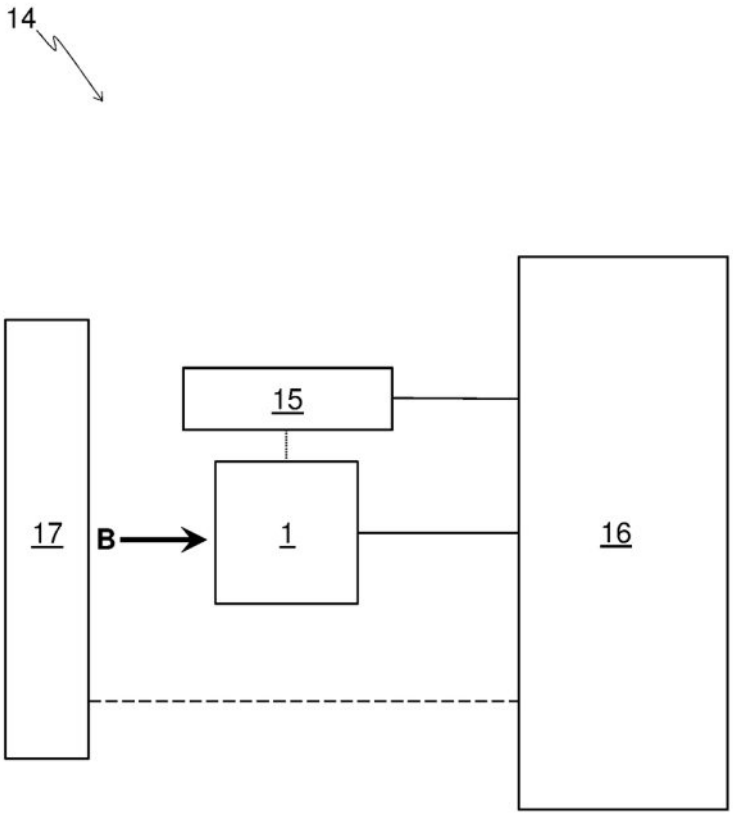

Fig. 3

INTERNATIONAL SEARCH REPORT

International application No
PCT/AT2017/060082

A. CLASSIFICATION OF SUBJECT MATTER
INV. G01L1/10 G01L5/16
ADD.

According to International Patent Classification (IPC) or to both national classification and IPC

B. FIELDS SEARCHED

Minimum documentation searched (classification system followed by classification symbols)
G01L

Documentation searched other than minimum documentation to the extent that such documents are included in the fields searched

Electronic data base consulted during the international search (name of data base and, where practicable, search terms used)
EPO-Internal, WPI Data

C. DOCUMENTS CONSIDERED TO BE RELEVANT

Category*	Citation of document, with indication, where appropriate, of the relevant passages	Relevant to claim No.
X	WO 2011/163058 A2 (UNIV ILLINOIS [US]; BASHIR RASHID [US]; PARK KIDONG [KR]; MILLET LARRY) 29 December 2011 (2011-12-29) figures 1A, 3a-j, 4a, 6, 9C paragraphs [0092], [0100], [0113], [0143], [0190]	1-3,5,6, 11-14,16
Y	JP S61 194325 A (SHINKO DENSHI KK) 28 August 1986 (1986-08-28) figures 3a, 3b, 8, 9	1,4, 7-10,15, 17,18
Y	US 5 095 763 A (DELATORRE LEROY C [US]) 17 March 1992 (1992-03-17) column 6, lines 13-24	1,4, 7-10,15, 17,18

☐ Further documents are listed in the continuation of Box C.

☒ See patent family annex.

* Special categories of cited documents :

"A" document defining the general state of the art which is not considered to be of particular relevance

"E" earlier application or patent but published on or after the international filing date

"L" document which may throw doubts on priority claim(s) or which is cited to establish the publication date of another citation or other special reason (as specified)

"O" document referring to an oral disclosure, use, exhibition or other means

"P" document published prior to the international filing date but later than the priority date claimed

"T" later document published after the international filing date or priority date and not in conflict with the application but cited to understand the principle or theory underlying the invention

"X" document of particular relevance; the claimed invention cannot be considered novel or cannot be considered to involve an inventive step when the document is taken alone

"Y" document of particular relevance; the claimed invention cannot be considered to involve an inventive step when the document is combined with one or more other such documents, such combination being obvious to a person skilled in the art

"&" document member of the same patent family

Date of the actual completion of the international search	Date of mailing of the international search report
27 November 2017	12/12/2017

Name and mailing address of the ISA/	Authorized officer
European Patent Office, P.B. 5818 Patentlaan 2 NL - 2280 HV Rijswijk Tel. (+31-70) 340-2040, Fax: (+31-70) 340-3016	Schambach, Philip

1

Form PCT/ISA/210 (second sheet) (April 2005)

INTERNATIONAL SEARCH REPORT

Information on patent family members

International application No
PCT/AT2017/060082

Patent document cited in search report	Publication date	Patent family member(s)	Publication date
WO 2011163058 A2	29-12-2011	US 2014026686 A1	30-01-2014
		WO 2011163058 A2	29-12-2011
JP S61194325 A	28-08-1986	NONE	
US 5095763 A	17-03-1992	NONE	

Form PCT/ISA/210 (patent family annex) (April 2005)

INTERNATIONALER RECHERCHENBERICHT

Internationales Aktenzeichen
PCT/AT2017/060082

A. KLASSIFIZIERUNG DES ANMELDUNGSGEGENSTANDES
INV. G01L1/10 G01L5/16
ADD.

Nach der Internationalen Patentklassifikation (IPC) oder nach der nationalen Klassifikation und der IPC

B. RECHERCHIERTE GEBIETE

Recherchierter Mindestprüfstoff (Klassifikationssystem und Klassifikationssymbole)
G01L

Recherchierte, aber nicht zum Mindestprüfstoff gehörende Veröffentlichungen, soweit diese unter die recherchierten Gebiete fallen

Während der internationalen Recherche konsultierte elektronische Datenbank (Name der Datenbank und evtl. verwendete Suchbegriffe)
EPO-Internal, WPI Data

C. ALS WESENTLICH ANGESEHENE UNTERLAGEN

Kategorie*	Bezeichnung der Veröffentlichung, soweit erforderlich unter Angabe der in Betracht kommenden Teile	Betr. Anspruch Nr.
X	WO 2011/163058 A2 (UNIV ILLINOIS [US]; BASHIR RASHID [US]; PARK KIDONG [KR]; MILLET LARRY) 29. Dezember 2011 (2011-12-29) Abbildungen 1A, 3a-j, 4a, 6, 9C Absätze [0092], [0100], [0113], [0143], [0190]	1-3,5,6, 11-14,16
Y	JP S61 194325 A (SHINKO DENSHI KK) 28. August 1986 (1986-08-28) Abbildungen 3a, 3b, 8, 9	1,4, 7-10,15, 17,18
Y	US 5 095 763 A (DELATORRE LEROY C [US]) 17. März 1992 (1992-03-17) Spalte 6, Zeilen 13-24	1,4, 7-10,15, 17,18

☐ Weitere Veröffentlichungen sind der Fortsetzung von Feld C zu entnehmen ☒ Siehe Anhang Patentfamilie

* Besondere Kategorien von angegebenen Veröffentlichungen :
"A" Veröffentlichung, die den allgemeinen Stand der Technik definiert, aber nicht als besonders bedeutsam anzusehen ist
"E" frühere Anmeldung oder Patent, die bzw. das jedoch erst am oder nach dem internationalen Anmeldedatum veröffentlicht worden ist
"L" Veröffentlichung, die geeignet ist, einen Prioritätsanspruch zweifelhaft erscheinen zu lassen, oder durch die das Veröffentlichungsdatum einer anderen im Recherchenbericht genannten Veröffentlichung belegt werden soll oder die aus einem anderen besonderen Grund angegeben ist (wie ausgeführt)
"O" Veröffentlichung, die sich auf eine mündliche Offenbarung, eine Benutzung, eine Ausstellung oder andere Maßnahmen bezieht
"P" Veröffentlichung, die vor dem internationalen Anmeldedatum, aber nach dem beanspruchten Prioritätsdatum veröffentlicht worden ist
"T" Spätere Veröffentlichung, die nach dem internationalen Anmeldedatum oder dem Prioritätsdatum veröffentlicht worden ist und mit der Anmeldung nicht kollidiert, sondern nur zum Verständnis des der Erfindung zugrundeliegenden Prinzips oder der ihr zugrundeliegenden Theorie angegeben ist
"X" Veröffentlichung von besonderer Bedeutung; die beanspruchte Erfindung kann allein aufgrund dieser Veröffentlichung nicht als neu oder auf erfinderischer Tätigkeit beruhend betrachtet werden
"Y" Veröffentlichung von besonderer Bedeutung; die beanspruchte Erfindung kann nicht als auf erfinderischer Tätigkeit beruhend betrachtet werden, wenn die Veröffentlichung mit einer oder mehreren Veröffentlichungen dieser Kategorie in Verbindung gebracht wird und diese Verbindung für einen Fachmann naheliegend ist
"&" Veröffentlichung, die Mitglied derselben Patentfamilie ist

Datum des Abschlusses der internationalen Recherche	Absendedatum des internationalen Recherchenberichts
27. November 2017	12/12/2017

Name und Postanschrift der Internationalen Recherchenbehörde	Bevollmächtigter Bediensteter
Europäisches Patentamt, P.B. 5818 Patentlaan 2 NL - 2280 HV Rijswijk Tel. (+31-70) 340-2040, Fax: (+31-70) 340-3016	Schambach, Philip

1

Formblatt PCT/ISA/210 (Blatt 2) (April 2005)

INTERNATIONALER RECHERCHENBERICHT

Angaben zu Veröffentlichungen, die zur selben Patentfamilie gehören

Internationales Aktenzeichen
PCT/AT2017/060082

Im Recherchenbericht angeführtes Patentdokument	Datum der Veröffentlichung	Mitglied(er) der Patentfamilie	Datum der Veröffentlichung
WO 2011163058 A2	29-12-2011	US 2014026686 A1 WO 2011163058 A2	30-01-2014 29-12-2011
JP S61194325 A	28-08-1986	KEINE	
US 5095763 A	17-03-1992	KEINE	

Formblatt PCT/ISA/210 (Anhang Patentfamilie) (April 2005)

VIII. Conclusio and Outlook

In this present thesis we demonstrated a set of different mechanical sensor structures to measure at first the magnetic flux density in at least two directions in space as well as the local flux density gradient. The last parameter deserves closer attention especially in high sensitive applications like the accelerator dipoles at the LHC (large hadron collider) of every other particle accelerator. The second sensor type is an outcome of the magnetic field sensors and is able to measure displacement in at least two directions in space or torsion around two axis perpendicular two each other. In the presented papers are simulation data as well as the belonging measurement data compared with each other. We constitute mathematical analogous models for the simplest cases all the resonant sensing structures in the theoretical part of this thesis.

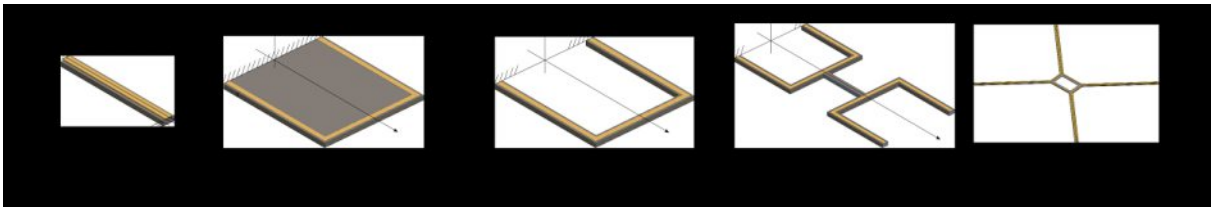

Figure 35: This figure demonstrates the growth of the sensor development during this thesis. Origin from the simple cantilever (first and second picture) for magnetic field sensing as well as chemical experiments (e.g. mass-spectroscopy) we find the U-shaped magnetic field sensing structure (for one- and two-dimensional flux density sensing) and the double-U-shaped structure (fourth picture) as well as the omega-shaped-structure (not depicted here) for flux density gradient sensing. Finally the cross shaped structure from the displacement sensor is depicted at last.

The magnetic flux density gradient sensor has an overall sensitivity of 2.5µT and a minimal detectable field gradient of 1µT/mm. During the experiments with the double-U-shaped structure and the omega-shaped structure the temperature effect of the resonance frequency decreases from 5.8Hz/K to 1.3Hz/K respectively. We also investigated a torsional bending structure to demonstrate the temperature effects of a simple double clamped cantilever at higher vibration modes and find that the dependency from the resonance frequency is 12.4Hz/K. The displacement sensor is investigated with a deformation in one direction as well as in two dimensions. Using a symmetric and an antisymmetric vibration mode the crosstalk between the different load states is almost zero. For a one-dimensional displacement we get a sensitivity of 15nm/Hz and 20nm/Hz for two-dimensional displacement.

In the years ahead the sensor development will reach new dimensions induced by a large growing automatization sector and even more by an exponential increase of the number of so

called smart devices (e.g. in the automotive sector as well as the portable devices) and the trend to IoT (internet of things) cross-linking of formerly non digital appliances. Not a quarter as good growing is the sector of high specialised sensing devices like AFM (atomic force microscopes) modules or testing machines but their requirements are become ever larger and therefore the requirements for sensing devices will even harder to handle. In this sector our research-projects will find a niche to position the high precise devices for selected unexplored applications.

IX. Appendix

9.1 RMAS

The **R**esonant **M**emory **A**rray **S**ystem is a theoretical simulation model. The idea comes from the calculations to the PikoSens project and monitors the possibility to store information in a cantilever array by varying the positions of mass-points over the length of the cantilever. This array is a non-rewritable permanent information storage. Three mass-points located on a double clamped cantilever with initial positions distributed symmetrically over the length of the cantilever. The ratio μ between the additional mass and the cantilever mass is approximately one. Each cantilever has a parallel one with the same masses located in the initial positions. Apart from manufacturing deviations the two cantilevers have the same resonance frequencies and also the temperature induced variations affect equal on both cantilevers.

In theory there are 343 possible variations with these three mass-points provided that each has seven possible positions (the initial position and three positions left and right respectively delivers 7^3 states). To avoid undifferentiable mirrored positions we have to subtract 168 states and get 175 possible variations.

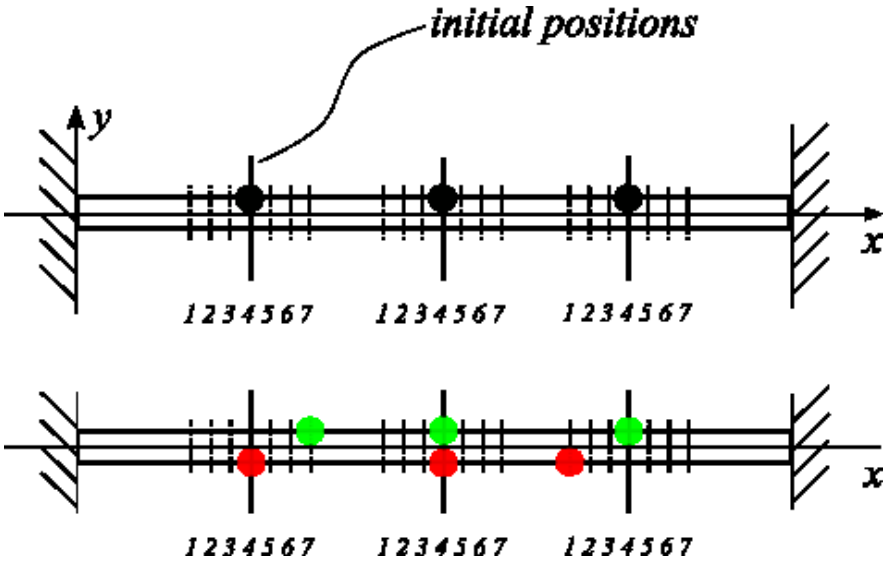

Figure 36: above: mass-points on their initial positions (ground state). below: a possible state marked green and a redundant mirrored state marked red.

To store information in the system the position of at least one mass-point on one of the cantilevers varies towards the other cantilever to change the resonance frequency. The position of the mass-points varies in discrete values to get well defined differences in the resonance frequency. The smallest variations depends on the minimal detectable frequency change in relation with the readout proceed.

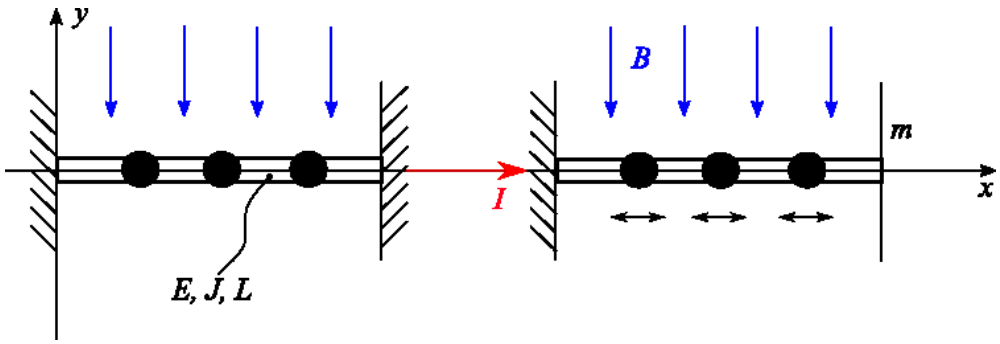

Figure 37: Model of the Resonant Memory Array System with the two cantilevers including additional mass-points in their initial positions. The left cantilever is the reference one and the right has the adjustable mass-points do detune the resonance frequency. The cantilevers are even Lorentz Force driven whereby the main parameters are depicted.

The frequency variation is, avoiding mirrored shifts of the mass-points, representative for the positions and therefore a measure for the stored information.

The length of the cantilever is 350nm, the width 30nm with a thickness of 10nm

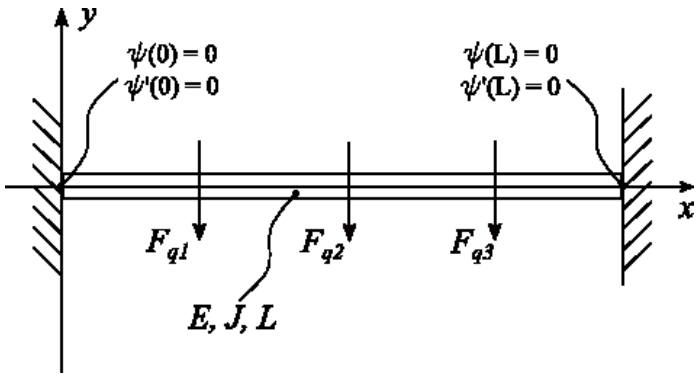

Figure 38: Analogous model for the calculations and simulations. The additional masses produces shear forces which generates three more boundary conditions.

Well sealed, the RMAS with the permanent written cantilevers are largely independent from external influences like magnetic fields or extreme temperatures as aging processes of the material occur equal on both, the measurement and the reference cantilever.

X. Publications

10.1 Journal articles

(1) M. Stifter; “MEMS µ-wire magnetic field detection method@CERN.”; IEEE Sensors Journal, 15717295, 2015 vol2
Co-author; in print
Internet publication: https://ieeexplore.ieee.org/abstract/document/7370244

(2) A. Dabsch, “MEMS cantilever based magnetic field gradient sensor”, Journal of micromechanics and microengineering, vol 27 no 5, april 2017
Lead author; in print
Internet publication: https://iopscience.iop.org/article/10.1088/1361-6439/aa654f/meta

(3) Dabsch; “Temperature dependency of solicon structures for magnetic field gradient sensing”; Journal of Micromechanics and Microengineering; July 2017
Lead author; in print
Internet publication: https://iopscience.iop.org/article/10.1088/1361-6439/aa7d28/meta

(4) A. Dabsch; “Multiaxial Resonant MEMS Force Sensor”; Journal of Micromechanics and Microengineering; vol 28 no 10; june 2018
Lead author, in print
Internet Publication: https://iopscience.iop.org/article/10.1088/1361-6439/aac13e/meta

(5) A. Dabsch; “Two dimensional displacement measurement with MEMS structure”; Journal of Micromechanics and Microengineering
Lead author, under review

10.2 Patents

(1) WO2017083898A1; Sensor zur Bestimmung eines Drehwinkels; main inventor; A. Dabsch, A. Kainz, F. Keplinger; 17.11.2015
Internet Publication:
https://worldwide.espacenet.com/patent/search/family/057482111/publication/AT517945A4?q=pn%3DAT517945A4

(2) WO2018/176069A1; Force Sensor; main inventor A. Dabsch, F. Keplinger, C. Rosenberg, 31.03.2017
Internet Publication:
https://worldwide.espacenet.com/patent/search/family/058638618/publication/WO2018176069A1?q=pn%3DWO2018176069A1

(3) WO2019071281A1; Modulares System für Warenausgabeautomaten sowie ein Modul für ein solches modulares System; main inventor; A. Dabsch, R. Harrer; 11.10.2017
Internet Publication:
https://worldwide.espacenet.com/patent/search?q=pn%3DWO2019071281A1

(4) AT521357A4; Warenausgabeautomat; main inventor; A. Dabsch, R. Harrer; 24.07.2018 Internet Publication: https://worldwide.espacenet.com/patent/search/family/069146845/publication/AT521357A4?q=pn%3DAT521357A4

XI. Bibliography

[i] E. Donzier et. al.; „Integrated Magnetic Field Sensor“; Sensors and Actuators A, 26:357-361; 1991

ii M. R. Koblischka and U. Hartmann; “Recent advances in magnetic force microscopy”; Ultramicroscopy, 97(1–4):103–112, 2003.

iii M. Stifter; Lorentz Force Actuated Resonant MEMS Magnetometer with Capacitive Read-out; Technische Universität Wien; October 2012

[iv] M. Stifter; “MEMS µ-wire magnetic field detection method@CERN.”; IEEE Sensors Journal, 15717295, 2015 vol2

v H. Lang et. al.; “A chemical sensor based on a micromechanical cantilever array for the identification of gases and vapors”. Appl. Phys., A 66:S61–S64, 1998.

vi T. Thundat et. al.; Appl. Phys. Lett. 66, 1695 (1995)

vii D. R. Baselt et. al.;“Design and performance of a microcantilever-based hydrogen sensor.” Sens. Actuators B, 88:120–131, 2003.

viii F. Keplinger; “Contributions to Miniaturized Sensors”; Postdoctoral thesis; Vienna; June 2005

ix S. Deladi et. al.; „Micromachined fountain pen for atomic foce microscope-based nanopatterning.“; Appl. Phys. Lett., 85(22):5361-5363; 2004

[x] L. Latorre et. al.; „Design, characterization and modelling of a CMOS magnetic field sensor; In DATE’99; Design Automation and Test in Europe, p 239-243; Munich Germany, March 9-12; 1999

[xi] A. Dabsch, “MEMS cantilever based magnetic field gradient sensor”, Journal of micromechanics and microengineering, vol 27 no 5, april 2017

[xii] S. Timoshenko. History of strength of materials. McGraw-Hill, 1983.

[xiii] A. Metthew, „What is the young’s modulus of silicon?“; Journal of Microelectromechanical Systems; vol19; issue 2; April 2019

[xiv] L. D. Landau and E. M. Lifshitz. Theory of Elasticity. Pergamon, Oxford, 1986.

[xv] D.M. Parks; Mechanics and Materials; MIT; Feb 2004; https://ocw.mit.edu/courses/mechanical-engineering/2-002-mechanics-and-materials-ii-spring-2004/lecture-notes/lec2.pdf

[xvi] A. Dabsch; “Multiaxial Resonant MEMS Force Sensor”; Journal of Micromechanics and Microengineering; vol 28 no 10; june 2018

[xvii] Marinescu M. (1996) Induktionswirkung und Induktionsgesetz. In: Elektrische und magnetische Felder. Springer, Berlin, Heidelberg, pp 233-256

[xviii] C. M. Harris and Allan G. Piersol, editor. Harri’s Shock and Vibration Handbook. McGraw-Hill, 2002

[xix] S. Schmid; (2016) „Fundamentals of Nanomechanical Resonators“; Springer, Switzerland, pp56 ff

[xx] S. Schmid; (2016) „Fundamentals of Nanomechanical Resonators“; Springer, Switzerland, pp46

[xxi] V. Kaajakari; „Nonlinear Limits for Single-Crystal Silicon Microresonators“; JOURNAL OF MICROELECTROMECHANICAL SYSTEMS, p717, Fig. 3, VOL. 13, NO. 5, OCTOBER 2004 715

[xxii] M.A. Hopcroft, W.D. Nix and T.W. Kenny, ”What is the Young´s Modulus of Silicon”, MEMS IEEE, vol. 19, no. 2, pp. 229-238, April 2010.

[xxiii] H. Watanabe; „Linear Thermal Expansion Coefficient of Silicon from 293 to 1000 K“; Int. Journal of Thermophysics; Jan 2004; vol. 25 issue 1; pp221-236

[xxiv] Crandall, Dahl, Lardner An Introduction to the Mechanics of Solids. McGraw-Hill, Boston 1959